An analysis of acquisition-related subsampling effects on Marchenko focusing, redatuming, and primary estimation

Peng, Haorui; Vasconcelos, Ivan; Sripanich, Yanadet; Zhang, Lele

DOI
10.1190/geo2020-0914.1

Publication date
2021

Document Version
Accepted author manuscript

Published in
Geophysics

Citation (APA)
Peng, H., Vasconcelos, I., Sripanich, Y., & Zhang, L. (2021). An analysis of acquisition-related subsampling effects on Marchenko focusing, redatuming, and primary estimation. *Geophysics*, *86*(5), WC75-WC88. https://doi.org/10.1190/geo2020-0914.1

GEOPHYSICS®

An analysis of acquisition-related subsampling effects on Marchenko focusing, redatuming, and primary estimation

Journal:	*Geophysics*
Manuscript ID	GEO-2020-0914.R3
Manuscript Type:	Advances in seismic multiple reflection processing
Keywords:	internal multiples, autofocusing
Manuscript Focus Area:	Special Section

An analysis of acquisition-related subsampling effects on Marchenko focusing, redatuming, and primary estimation

Haorui Peng*, **Ivan Vasconcelos***, **Yanadet Sripanich***, **Lele Zhang**†

**Utrecht University, 3584 CB Utrecht, The Netherlands* †*Delft University of Technology,*
2628 CN Delft, The Netherlands

(June 1, 2021)

Running head: **Acquisition Effects on Marchenko Methods**

ABSTRACT

Marchenko methods can retrieve both Green's functions and focusing functions from single-sided reflection data and a smooth velocity model, as essential components of a redatuming process. Recent studies also show that a modified Marchenko scheme can reconstruct primary-only reflection responses directly from reflection data without requiring a priori model information. To provide insight into the artifacts that arise when input data are not ideally sampled, we study the effects of subsampling in both types of Marchenko methods in 2D earth and data — by analyzing the behaviour of Marchenko-based results on synthetic data subsampled in sources or receivers. We show with a layered model that for Marchenko redatuming, subsampling effects jointly depend on the choice of integration variable and the subsampling dimension, originated from the integrand gather in the multidimensional convolution process. When reflection data are subsampled in a single dimension, integrating on the other yields spatial gaps together with artifacts while integrating on the subsampled dimension produces aliasing artifacts but without spatial gaps. Our complex subsalt model shows the subsampling may lead to very strong artifacts, which can be further complicated by having limited apertures. For Marchenko-based primary estimation (MPE), subsampling below a certain fraction of the fully-sampled data can cause MPE iterations to diverge, which can to some extent be mitigated by using more robust iterative solvers, such as LSQR. Our results, covering redatuming and primary estimation in a range of subsampling scenarios, provide insights that can inform acquisition sampling choices as well as processing parameterization and quality control, e.g., to set up appropriate data filters and scaling to accommodate the effects of dipole fields, or to help ensuring that the data interpolation achieves the desired levels of reconstruction quality that minimize subsampling artifacts in Marchenko-derived fields and images.

INTRODUCTION

By means of Marchenko methods, the full-waveform Green's function to a virtual source in the subsurface can be retrieved from single-sided reflection data. Given a smooth velocity model (Wapenaar et al., 2014), this is accomplished by solving a set of coupled Marchenko equations by direct least-squares (LSQR) inversion (van der Neut et al., 2015a) or iterative substitution (van der Neut et al., 2015b). The method, in theory, retrieves internal multiples with correct amplitudes. One of the challenges of this method is that the multidimensional convolution operation of the reflection response with the focusing function requires a regularly sampled, dense data set with co-located sources and receivers. Similar multidimensional convolution operations are also employed — and fairly well-understood — in surface-related multiple-elimination (SRME) (Verschuur et al., 1992; Lopez and Verschuur, 2015). Here, we look into the effects of regular subsampling in the Marchenko method specifically — showing both similarities and differences to the effects seen in SRME applications. Haindl et al. (2018) formulate the Marchenko equations with sparse inversion to alleviate the 2D irregular source subsampling effect. This study observed spatial gaps in both the output redatumed Green's function and the focusing function. Ravasi (2017) also studies the effect of irregular subsampling in sources in the Rayleigh-Marchenko method with LSQR inversion and observed artifacts, but no spatial gaps in the retrieved signals, thereby showing the Rayleigh approach's flexibility in handling the source subsampling. Sripanich and Vasconcelos (2019) provide a comprehensive study on the effects of a limited aperture on Marchenko focusing functions and their radiation behaviour of focusing. In synthetic and field data studies, respectively, Jia et al. (2019) and Staring and Wapenaar (2020) present 3D Marchenko redatuming, where they apply data interpolation to fill the gaps caused by subsampling. More recently, in a companion study to this paper, both regular and irregular subsampling effects on 3D redatuming are discussed by Ravasi and Vasconcelos (2020), in the context of high-performance computing. To account for the imperfect source sampling, Wapenaar and van IJsseldijk (2020) develop a new discrete representation containing point-spread functions that can be multidimensionally deconvolved to deblur the focusing functions and Green's functions. van IJsseldijk and Wapenaar (2020) then alter the iterative Marchenko scheme to integrate this new representation and tested it on synthetic data. All of the above studies alleviate the subsampling effects using different approaches, including sparse inversion, LSQR inversion, and/or data interpolation. Yet, there is still a need to build a basic understanding of these effects' origin and patterns, which could not only inform acquisition sampling choices in the future, but crucially help in the design and quality-control of pre-processing routines tailored toward Marchenko methods.

While the original form of the Marchenko system is designed to perform redatuming, i.e., retrieve subsurface wavefields, the framework can also be employed for surface-to-surface internal multiple prediction — or more specifically — to predict primary-only data. To that end, an alternative, surface-projected form of the Marchenko equations presented by van der Neut and Wapenaar (2016) was recently employed to eliminate multiples directly from reflection data without requiring model information (Zhang and Staring, 2018). In a comparative study, Zhang et al. (2019a) illustrate the benefits and shortcomings of Marchenko-based data-driven scheme for the internal multiple reflection elimination over the theory of inverse scattering series. The former method was further improved to compensate the transmission loss (Zhang et al., 2019b). In this context, i.e., Marchenko-based primary estimation, the effects of acquisition sampling remain largely unaddressed. Very recently, this projected scheme was also employed in the augmented Marchenko method to account for short-period internal multiples in media with a horizontally layered overburden by Elison et al. (2020).

Over recent years, Marchenko-based methods have been developed in two related, yet distinct contexts: depth-domain redatuming and data-domain primary estimation. In this paper, we choose to look into Marchenko approaches in both of these contexts, because they typically pertain to different applications — namely, redatuming is tied to full-wavefield imaging at depth, while primary estimation is usually a pre-processing step prior to model building and imaging. To this end, building on the aforementioned studies that look into acquisition aspects of the Marchenko approaches in specific contexts, we intend to provide a basic understanding of acquisition sampling effects in focusing, redatuming and primary estimation.

Two types of Marchenko methods are addressed in this paper also because they require different inputs and temporal-windowing approaches. Albeit relying on the same general operations of multidimensional convolution and correlation, these two types of Marchenko approaches can behave differently in the presence of subsampling. There are two main reasons for this: (i) Marchenko redatuming does not perform time stepping and uses the full wavefield that has been retrieved by focusing for a given redatuming level, and primary estimation applies time stepping and just selects the samples at that time after applying the Marchenko method at a given time step; (2) the windowing operators themselves in Marchenko redatuming and primary estimation are different, leading to differences in the physical contributions of the convolution processes in either of the applications. We observe that subsampled input data cause artifacts for both methods, and may further lead to divergence for the primary estimation, depending on the degree of subsampling and the algorithm used to solve the system, i.e., Neumann series expansion, or LSQR inversion. Because we wish to analyze subsampling at varying levels of aliasing, we maintain a fixed bandwidth and only vary sampling. In practice, sampling and aliasing are both relative to the actual data bandwidth and as a general rule, adequately sampling the integrals requires satisfying the general spatial Nyquist criteria for the integrands — similarly to well-known applications such as SRME or evaluating Kirchhoff-type integrals.

Our study of the subsampling effects is structured in a simple, yet general framework that could inform acquisition design or help tuning and controlling data processing. With this goal in mind, we limit ourselves to 2D regular subsampling in just one dimension (source or receiver). We believe that the insight of this case shares similarities with the other cases, e.g., irregular subsampling in both dimensions. As 3D and data interpolation are related, yet complex topics, they are left for future research and therefore are not included in this study. We first look at subsampling numerical examples in 2D to mimic subsampling caused by realistic acquisition design. We then analyze the results of the aforementioned two Marchenko methods in the context of subsampling without data interpolation, also by looking at specific yet simple measures to alleviate the effects of subsampling, like invoking spatial reciprocity.

In all current forms of Marchenko methods — whether in the context of redatuming or primary estimation — the theory clearly outlines that both monopole (e.g., pressure-to-pressure) and dipole (e.g., particle velocity-to-pressure) fields are not only required, but must be employed in specific source and receiver configurations (Wapenaar et al., 2014; van der Neut et al., 2015b). When it comes to field data, e.g., in offshore acquisition settings, though monopole fields are easily available from both streamer and ocean-bottom acquisitions, dipole fields are usually only available on the receiver side in the form of acceleration or velocity measurements from multicomponent sensors. Thus, in this paper, we show the effects of subsampling in the presence of dipole sources — which are generally not available in practice — as well as dipole receivers. We do this to provide insights on the importance and effects of dipole integration choices, that may impact choices on how to use multicomponent sensor data for Marchenko applications, or on how to pre-process single component data to be used in Marchenko schemes.

The layout of this paper is as follows. We begin by presenting the Marchenko integral representations, while paying particular attention to the discrete form of the terms within the iterative solution of the coupled Marchenko system, followed by a brief review of the primary estimation method (Zhang and Staring, 2018). With a layered benchmark model, we then illustrate our observations on subsampling effects on Marchenko focusing for multiple scenarios, including the joint effects of subsampling versus the dipole source/receiver integration variable choice, and the effects of focusing depth jointly with subsampling. Next, a complex subsalt model to illustrate subsampling effects together with limited aperture on Marchenko redatuming in a more realistic scenario. Subsequently, we show with numerical examples for both Marchenko systems that integrating on the monopole dimension instead of the (theoretically correct) dipole dimension actually yields negligible errors compared with true results for media with mild lateral heterogeneity. Finally for the primary estimation, we compare the joint effects of different subsampling schemes versus different approaches to solve the Marchenko system with a layered model and provide an operator norm analysis for the iterative substitution method.

THEORY OF MARCHENKO REDATUMING AND PRIMARY ESTIMATION

Discrete integration in the Marchenko framework

According to Wapenaar et al. (2014), the coupled Marchenko representations for the acoustic medium can be defined in frequency domain by integrating on the dipole-source dimension with the receiver being monopole:

$$\hat{G}^{-}(\mathbf{x}_F;\mathbf{x}_r) = \int_{\Lambda_R} d\mathbf{x}_s \hat{R}(\mathbf{x}_r;\mathbf{x}_s)\hat{f}_1^{+}(\mathbf{x}_s;\mathbf{x}_F) - \hat{f}_1^{-}(\mathbf{x}_r;\mathbf{x}_F), \tag{1}$$

$$\hat{G}^{+*}(\mathbf{x}_F;\mathbf{x}_r) = -\int_{\Lambda_R} d\mathbf{x}_s \hat{R}^{*}(\mathbf{x}_r;\mathbf{x}_s)\hat{f}_1^{-}(\mathbf{x}_s;\mathbf{x}_F) + \hat{f}_1^{+}(\mathbf{x}_r;\mathbf{x}_F), \tag{2}$$

$$\hat{R}(\mathbf{x}_r;\mathbf{x}_s) = \frac{2}{j\omega\rho(\mathbf{x}_s)}\frac{\partial \hat{G}(\mathbf{x}_r;\mathbf{x}_s)}{\partial z_s}, \tag{3}$$

where $\mathbf{x}_F$, $\mathbf{x}_r$ and $\mathbf{x}_s$ are spatial coordinates of the focal point, receiver and source positions, respectively. The circumflex accent denotes wavefields in frequency domain. $\hat{f}_1^{+}$ and $\hat{f}_1^{-}$ are the downgoing and upgoing focusing functions, correspondingly. $\hat{G}^{-}$ and $\hat{G}^{+*}$ are the upgoing and the time-reversed downgoing Green's functions. Λ_R denotes an open boundary that corresponds to the surface acquisition level. ∂z_s represents the spatial derivative along the depth at the source position. As such, $\hat{R}(\mathbf{x}_r;\mathbf{x}_s)$ is twice the pressure recorded at $\mathbf{x}_r$ due to a vertical dipole source at $\mathbf{x}_s$. $\hat{G}(\mathbf{x}_r;\mathbf{x}_s)$ is the pressure response from a monopole source, and j is the imaginary unit. ω is the angular frequency, and $\rho(\mathbf{x}_s)$ is mass density at the source position.

Given only reflection surface data as a known input, the system in equations 1 and 2 can only be solved for the unknown focusing functions after employing additional constraints. The more established version of the Marchenko redatuming scheme (e.g. van der Neut et al., 2015b), accomplishes this by introducing a known initial focusing function, and a causality windowing operator leading to a discrete version of the Marchenko system that can be solved for the focusing functions:

$$\underbrace{\left(\begin{bmatrix}\mathbf{I} & \mathbf{0}\\ \mathbf{0} & \mathbf{I}\end{bmatrix}-\begin{bmatrix}\mathbf{0} & \mathbf{WR}\\ \mathbf{WR}^{\star} & \mathbf{0}\end{bmatrix}\right)}_{\mathbf{M}}\begin{bmatrix}\boldsymbol{f}_{1}^{-}\\ \boldsymbol{f}_{m}^{+}\end{bmatrix}=\begin{bmatrix}\mathbf{0} & \mathbf{WR}\\ \mathbf{WR}^{\star} & \mathbf{0}\end{bmatrix}\begin{bmatrix}\mathbf{0}\\ \boldsymbol{f}_{1d}^{+}\end{bmatrix}, \tag{4}$$

where the focusing functions are discrete vectors corresponding to a fixed focal point and all points on the acquisition surface: $\boldsymbol{f}_{m}^{+}$ is the coda of the downgoing focusing function, $\boldsymbol{f}^{-}$ is its upgoing response, and $\boldsymbol{f}_{1d}^{+}$ is the input initial focusing function. Here, following van der Neut et al. (2015b), $\mathbf{R}$ and $\mathbf{R}^{\star}$ are the discrete integral operators that apply multidimensional convolution and correlation in the time domain between the reflection response and the focusing functions, respectively. $\mathbf{W}$ is the operator enforcing causality by windowing in the time domain. Note that the Marchenko system in equation 4 has the same form either in the time or frequency domain — we hereon refer to equations in the frequency domain for the sake of convenience. The system in equation 4 can be solved for $\boldsymbol{f}_{m}^{+}$ and $\boldsymbol{f}^{-}$, by employing a Neumann series expansion of the $\mathbf{M}$ operator (under appropriate conditions, as in Dukalski and de Vos, 2018), the so-called Marchenko iterative scheme is obtained. Once the focusing functions are solved for, the redatumed wavefields, $\hat{G}^{-}$ and $\hat{G}^{+}$, are then obtained by substituting the estimated focusing functions into the original system in equations 1 and 2.

For our purposes, to facilitate the analysis of integration-related effects, we focus on the first operation $\mathbf{R}\hat{\boldsymbol{f}}_{1d}^{+}$ of the iterative substitution method in the form of matrix-vector multiplication (corresponding to the discrete spatial convolutions):

$$\begin{bmatrix} \hat{f}^{-}_{1,K=0}(\mathbf{x}_r^{(0)};\mathbf{x}_F) \\ \vdots \\ \hat{f}^{-}_{1,K=0}(\mathbf{x}_r^{(Nr)};\mathbf{x}_F) \end{bmatrix} = \begin{bmatrix} \sum_{i=1}^{N_s} \hat{R}(\mathbf{x}_r^{(0)};\mathbf{x}_s^{(i)})\hat{f}^{+}_{1d}(\mathbf{x}_s^{(i)};\mathbf{x}_F)d\mathbf{x}_s \\ \vdots \\ \sum_{i=1}^{N_s} \hat{R}(\mathbf{x}_r^{(Nr)};\mathbf{x}_s^{(i)})\hat{f}^{+}_{1d}(\mathbf{x}_s^{(i)};\mathbf{x}_F)d\mathbf{x}_s \end{bmatrix}, \tag{5}$$

where $K = 0$ denotes the initial step of the iterative scheme, $\hat{f}^{+}_{1d}$ is the initial focusing function and N_s is the number of sources. Illustration of equation 5 is given in Figure 1a. Note that here we omit the action of the windowing operator as it does not affect the integrand within the spatial convolutions. This operation is interpreted as follows: the jth element on the left-hand-side corresponds to the trace at receiver position $\mathbf{x}_r^{(j)}$, that is calculated by summing the convolution gather between $\hat{R}(\mathbf{x}_r^{(j)};\mathbf{x}_s)$ and $\hat{f}^{+}_{1d}(\mathbf{x}_s;\mathbf{x}_F)$ for all the source positions and scaled by the (possibly subsampled) source interval.

By employing source-receiver reciprocity, the Marchenko equations can also be defined by integrating on the dipole-receiver dimension with the source being a monopole (van der Neut et al., 2015b):

$$\hat{G}^{-}(\mathbf{x}_F;\mathbf{x}_s) = \int_{\Lambda_f} d\mathbf{x}_r \hat{R}(\mathbf{x}_r;\mathbf{x}_s)\hat{f}^{+}_1(\mathbf{x}_r;\mathbf{x}_F) - \hat{f}^{-}_1(\mathbf{x}_s;\mathbf{x}_F), \tag{6}$$

$$\hat{G}^{+*}(\mathbf{x}_F;\mathbf{x}_s) = -\int_{\Lambda_f} d\mathbf{x}_r \hat{R}^{*}(\mathbf{x}_r;\mathbf{x}_s)\hat{f}^{-}_1(\mathbf{x}_r;\mathbf{x}_F) + \hat{f}^{+}_1(\mathbf{x}_s;\mathbf{x}_F), \tag{7}$$

$$\hat{R}(\mathbf{x}_r;\mathbf{x}_s) = \frac{2}{j\omega\rho(\mathbf{x}_r)}\frac{\partial \hat{G}(\mathbf{x}_r;\mathbf{x}_s)}{\partial z_r}. \tag{8}$$

Here $\hat{R}(\mathbf{x}_r;\mathbf{x}_s)$ is twice the vertical velocity recording at $\mathbf{x}_r$ due to a pressure source at $\mathbf{x}_s$ (compare with equation 3). ∂z_r represents the spatial derivative along the depth, and $\rho(\mathbf{x}_r)$ is the density, now both at the receiver position instead. Analogously to equation 5, the initial-iteration discrete convolution now has the form:

$$\begin{bmatrix} \hat{f}^{-}_{1,K=0}(\mathbf{x}_s^{(0)};\mathbf{x}_F) \\ \vdots \\ \hat{f}^{-}_{1,K=0}(\mathbf{x}_s^{(Ns)};\mathbf{x}_F) \end{bmatrix} = \begin{bmatrix} \sum\limits_{i=1}^{N_r} \hat{R}(\mathbf{x}_r^{(i)};\mathbf{x}_s^{(0)})\hat{f}^{+}_{1d}(\mathbf{x}_r^{(i)};\mathbf{x}_F)d\mathbf{x}_r \\ \vdots \\ \sum\limits_{i=1}^{N_r} \hat{R}(\mathbf{x}_r^{(i)};\mathbf{x}_s^{(Ns)})\hat{f}^{+}_{1d}(\mathbf{x}_r^{(i)};\mathbf{x}_F)d\mathbf{x}_r \end{bmatrix}, \qquad (9)$$

where N_r is the number of receivers. As a consequence, when integrating over the receiver locations, the jth-element output in the obtained upgoing focusing function now corresponds to a trace at source position $\mathbf{x}_s^{(j)}$, that is calculated by integrating the convolution gather $\hat{R}(\mathbf{x}_r;\mathbf{x}_s^{(j)})$ and $\hat{f}^{+}_{1d}(\mathbf{x}_r;\mathbf{x}_F)$ over the receiver positions, scaled by the (possibly subsampled) receiver interval. Figure 1b illustrates equation 9. Here, we rely on equations 5 and 9 to interpret the observed effects of subsampling in source and receiver dimensions.

One key point to note, here as well as throughout this paper, is that we refer to monopole and dipole sources and receivers so as to relate the numerical results to the fields in the equations above. However, in real-life, practical acquisition, dipole fields are not necessarily always available. For example, in an offshore acquisition setting, sources are generally of monopole type only — this means that to obtain dipole sources for calculations one would need to apply, e.g., local obliquity factor corrections. On the receiver side, however, dipole observations correspond to either direct particle velocity or acceleration measurements, which are generally present in ocean-bottom systems and available in some multicomponent streamer systems.

Marchenko-based primary estimation

With the objective of retrieving primary-only data from internal-multiple interference, in addition to redatuming, van der Neut and Wapenaar (2016) propose that the coupled Marchenko equations could be implicitly projected to the acquisition surface by the direct wavefield, such that they can be solved without the need of a macro velocity model. Based on this approach, they eliminate the primaries and multiples for the medium above a chosen depth level by adaptive subtraction. The projected focusing functions are defined as follows in the frequency domain:

$$\hat{v}^{-}(\mathbf{x}_r;\mathbf{x}_P) = \int_{\Lambda_f} d^2\mathbf{x}_F \hat{G}_d^{+}(\mathbf{x}_F;\mathbf{x}_P)\hat{f}_1^{-}(\mathbf{x}_r;\mathbf{x}_F), \tag{10}$$

$$\hat{v}_m^{+}(\mathbf{x}_r;\mathbf{x}_P) = \int_{\Lambda_f} d^2\mathbf{x}_F \hat{G}_d^{+}(\mathbf{x}_F;\mathbf{x}_P)\hat{f}_{1m}^{+}(\mathbf{x}_r;\mathbf{x}_F). \tag{11}$$

Here, $\mathbf{x}_P$ is the projection point at the acquisition surface. $\mathbf{x}_F$ is the focusing point, and Λ_f denotes the focusing level. G_d^{+} is the direct wavefield, which does not need to be known a priori. v^{-} is the projected upgoing focusing function. v_m^{+} is the coda of the projected downgoing focusing function. Likewise, the projected Green's functions are defined as

$$\hat{U}^{-}(\mathbf{x}_P;\mathbf{x}_s) = \int_{\Lambda_f} d^2\mathbf{x}_F \hat{G}_d^{+}(\mathbf{x}_F;\mathbf{x}_P)\hat{G}^{-}(\mathbf{x}_F;\mathbf{x}_s), \tag{12}$$

$$\hat{U}^{+}(\mathbf{x}_P;\mathbf{x}_s) = \int_{\Lambda_f} d^2\mathbf{x}_F \hat{G}_d^{+}(\mathbf{x}_F;\mathbf{x}_P)\hat{G}^{+}(\mathbf{x}_F;\mathbf{x}_s), \tag{13}$$

where $\hat{U}^{-}$ and $\hat{U}^{+}$ are the projected upgoing and downgoing Green's functions. The coupled Marchenko system after projection is

$$\hat{U}^{-}(\mathbf{x}_P;\mathbf{x}_s) = \int_{\Lambda_R} d\mathbf{x}_r \hat{R}(\mathbf{x}_r;\mathbf{x}_s)(\delta(\mathbf{x}_r - \mathbf{x}_P) + \hat{v}_m^{+}(\mathbf{x}_r;\mathbf{x}_P)) - \hat{v}^{-}(\mathbf{x}_s;\mathbf{x}_P), \tag{14}$$

$$\hat{U}^{+*}(\mathbf{x}_P;\mathbf{x}_s) = -\int_{\Lambda_R} d\mathbf{x}_r \hat{R}^{*}(\mathbf{x}_r;\mathbf{x}_s)\hat{v}^{-}(\mathbf{x}_r;\mathbf{x}_P) + (\delta(\mathbf{x}_r - \mathbf{x}_P) + \hat{v}_m^{+}(\mathbf{x}_s;\mathbf{x}_P)), \tag{15}$$

where $\hat{R}(\mathbf{x}_r;\mathbf{x}_s)$ is defined as equation 8. The band-limited 2D delta function $\delta(\mathbf{x}_r - \mathbf{x}_P)$ in space and frequency appears due to that f_{1d}^{+} is defined as the inverse of the direct arrival G_d^{+} — even though in the practical redatuming scheme it is generally approximated by the time-reversed G_d^{+}.

Relying on the same projection in time domain, Zhang and Staring (2018) propose to estimate multiple-free primaries directly from the input reflection data without prior model information or relying on adaptive subtraction. The discrete projected Marchenko equations in their theory are:

$$\boldsymbol{v}^- = \mathbf{W}_\epsilon^{t_2-\epsilon}\mathbf{R}\boldsymbol{\delta} + \mathbf{W}_\epsilon^{t_2-\epsilon}\mathbf{R}\boldsymbol{v}_m^+, \tag{16}$$

$$\boldsymbol{v}_m^+ = \mathbf{W}_\epsilon^{t_2-\epsilon}\mathbf{R}^\star\boldsymbol{v}^-, \tag{17}$$

where $\mathbf{W}_\epsilon^{t_2-\epsilon}$ is the windowing operator that removes all the signals outside the interval $(\epsilon, t_2 - \epsilon)$, where ϵ is, e.g., half length of the source wavelet and t_2 is the two-way traveltime between the acquisition surface and the fictitious focusing depth. $\boldsymbol{\delta}$ contains band-limited 2D delta functions in space and time. $\mathbf{R}$ and $\mathbf{R}^\star$ are the same reflection-data-based convolution and correlation integral operators as in the coupled Marchenko equations. $\mathbf{R}\boldsymbol{\delta}$ selects a given common-shot gather to be used for primary estimation. By inserting equation 16 into 17, and eliminating $\boldsymbol{v}^-$ gives

$$\left(\mathbf{I} - \mathbf{W}_\epsilon^{t_2-\epsilon}\mathbf{R}^\star\mathbf{W}_\epsilon^{t_2-\epsilon}\mathbf{R}\right)\boldsymbol{v}_{\boldsymbol{m}}^+ = \mathbf{W}_\epsilon^{t_2-\epsilon}\mathbf{R}^\star\mathbf{W}_\epsilon^{t_2-\epsilon}\mathbf{R}\boldsymbol{\delta}. \tag{18}$$

This equation can be solved by iterative substitution or by direct inversion to obtain $\boldsymbol{v}_{\boldsymbol{m}}^+$ and $\boldsymbol{v}^-$, which then could be used to calculate the projected upgoing Green's function by

$$\boldsymbol{U}^- = \mathbf{R}(\boldsymbol{\delta} + \boldsymbol{v}_m^+) - \boldsymbol{v}^-. \tag{19}$$

In an ideal case, when the focusing level coincides with an actual reflector in the subsurface, the first value in $\boldsymbol{U}^-$ would be the primary reflection generated by that reflector with a two-way travel time t_2. If not, the value in $\boldsymbol{U}^-$ at t_2 would be zero. By choosing t_2 as a variable and looping over all the time steps, the primaries can be retrieved simply by picking the values of $\boldsymbol{U}^-$ at t_2. The resulting algorithm is outlined in the following pseudo code:

Algorithm 1: Algorithm for Primary Estimation, after Zhang and Staring (2018)

```
Initialize $\mathbf{R}\boldsymbol{\delta}$ with a chosen common-shot gather;
for $t_2 = 0$ to $t_{max}$ do
    compute the windowing operator $\mathbf{W}_{\epsilon}^{t_2-\epsilon}$;
    solve equation 18 and equation 16 for $\boldsymbol{v}_m^{+}$ and $\boldsymbol{v}^{-}$;
    use $\boldsymbol{v}_m^{+}$ and $\boldsymbol{v}^{-}$ to compute $\boldsymbol{U}^{-}$ (equation 19);
    store the value of $\boldsymbol{U}^{-}$ at $t_2$;
```

It is important to note here, that while redatuming requires the numerical solutions only once per redatuming location, Marchenko-based primary estimation requires equation 18 to be solved for every time sample of the iteration above — for primary prediction for a single chosen shot gather. Hereafter, we rely on this algorithm to analyze subsampling effects in Marchenko-based primary estimation.

NUMERICAL ANALYSIS OF ACQUISITION-RELATED SUBSAMPLING EFFECTS

Joint effects of subsampling versus integration variable choice

For the purpose of benchmarking, we employ the same constant-wavespeed (2000 m/s), variable-density layered model (Figure 2a) from van der Neut et al. (2015b), who use it to provide a comprehensive study of the integral contributions to the Marchenko scheme. We choose this model such that the reader can refer to individual events and understand how they are generated — van der Neut et al. (2015b) provide a detailed analysis of how each event is reconstructed by redatuming in relation to the events present on the surface data, via an interferometric interpretation of the Marchenko integrals acting in the practical iterative scheme. Back to our case, Figure 2b and 2c show the regular sampling masks for source and receiver dimensions, which are used in all examples of Marchenko focusing and redatuming in this study. The full reflection data have 201 co-located sources and receivers with a spacing interval of 10 m. The acquisition spread lies within the range of $x = (-1000\,\mathrm{m}, 1000\,\mathrm{m})$ at the acquisition surface with time sampling rate $dt = 2.5\,\mathrm{ms}$. Two focal points are chosen for this model: one at $(X_F = 0\ \mathrm{m}, Z_F = 2670\ \mathrm{m})$ and the other $(X_F = 0\ \mathrm{m}, Z_F = 1125\ \mathrm{m})$, as shown in Figure 2a. Our study in this section will focus on the deeper focal point as discussed by van der Neut et al. (2015b), with the shallower one used later as a comparison. In our examples, all reflection responses are modeled by a spectral-element (SEM) wave solver from the Salvus package (Afanasiev et al., 2019) with monople sources and dipole receivers.

Because of the symmetry of the chosen model, the reflection responses are the same for co-located shot and receiver gathers, which allows us to freely integrate over either dimension. Figure 3 shows the focusing functions in time domain obtained by integrating on different chosen variables, with source- or receiver-domain subsampled data. Here, we show results after a fixed number of iterations (13 in this case) of the Marchenko scheme — the number of iterations is simply chosen arbitrarily to be more-than-sufficient for the scheme to achieve convergence, which in ideal sampling conditions occurs in a mere few (e.g., 3-5) iterations. Figure 3a is the benchmark focusing function obtained without subsampling. Figure 3b displays the same focusing function obtained by subsampling in either source or receiver and integrating on the same corresponding variable. Because of the subsampling, aliasing artifacts appear at far offsets but both focusing solutions in Figure 3b are fully sampled in space, i.e., surface-coordinate dimensions. In comparison, Figure 3c displays clear spatial gaps obtained by subsampling in source or receiver but integrating on the other variable, together with the far-offset artifacts seen in Figure 3b. A comparison of traces at far offset $x_r = 910\,\mathrm{m}$ in the three focusing functions of Figure 3a-3c displayed in Figure 3d shows that artifacts appear in both integration scenarios. From the trace plot we can also see that the artifacts in Figure 3b seem more unstable than those in Figure 3c due to poor sampling near the stationary-point contributions — these stationary-point regions are discussed by van der Neut et al. (2015b). Figure 3e-3g are the zoomed-in plots of Figure 3a-3c around the circles, respectively.

When integration is conducted over the subsampled dimensions (Figure 3b), the summation process in every element of the output upgoing focusing function $\hat{f}_1^-$ in equations 5 and 9 become increasingly inaccurate as a result of the increased subsampling interval, but they remain well-sampled in space because the row-space of equations 5 and 9 is well sampled. This property carries over in the subsequent convolution operations needed in the iterative scheme, or in any other iterative linear solver (e.g., LSQR), leading to error propagation at later iterations. As a consequence of the negligible scaling in the source-receiver reciprocity in terms of horizontally independent obliquity factor present in the monopole-dipole configuration (in this case, because the medium is laterally homogeneous), subsampling and integrating on the source or receiver dimension are equivalent. When the subsampling and integration are performed over different dimensions, the summation process in every non-zero element of the output upgoing focusing function $\hat{f}_1^-$ in equations 5 and 9 will be accurate, because the column space of equations 5 and 9 is well sampled. However, subsampling will result in spatial gaps in the output focusing function because equations 5 and 9 are now subsampled in the row space. At later iterations, the row-space gaps will remain and inaccuracies arise in the non-zero elements of the output focusing functions because the input focusing functions gaps carry over into the summation process, as shown in Figure 3d. A diagram of all the four cases in integration versus subsampling is given in Figure 4.

The corresponding focusing functions in Figure 3a-3c are transformed to the frequency-wavenumber $(f-k)$ domain, as shown by Figure 5a, 5b, and 5d, separately. Normalized by the maximum value of Figure 5a, 5c, and 5e show the differences between the benchmark response (Figure 5a) and those in Figure 5b and 5d, respectively. By comparing all the panels in Figure 5, we see that the aliasing effects caused by subsampling and integrating on the same dimension are relatively weaker — compared to subsampling and integrating on different dimensions where artifacts are generally stronger.

Figure 6 illustrates how the spatially-dependent artifacts at far-offset come into being in Figure 3b, as a result of column-space subsampling in equation 5. Shown in Figure 6a, 6c, and 6e are convolution gathers (i.e., the integrands) of $\mathbf{R}\boldsymbol{f}_{1d}^{+}$ at different receiver positions, where the gaps represent the missing sources. Their summation (properly scaled by the subsampling interval), corresponding to different elements in the vector of the output $\hat{f}_1^{-}(\mathbf{x}_r;\mathbf{x}_F)$, are shown by the blue traces in Figure 6b, 6d, and 6f, respectively. For reference, we overlay the corresponding traces of the focusing function without source subsampling. As can be seen from Figure 6, the focusing function traces obtained by the first convolutional operation with subsampling are very close to the reference ones at near offset, because traveltime varies slowly with respect to $\mathbf{x}_s$. Toward larger offsets, the rate of traveltime variations in the integrand increases, leading to steeper slopes in the integrand and thus aliasing-induced artifacts.

Figure 7a-7d show the errors caused by subsampling and integrating on the same dimension from the first to the fourth iterations. As can be seen, most error comes from the second iteration and then the error decreases in magnitude with increasing iteration numbers — this is expected assuming that the iterative scheme is applied within its convergence criteria of the spectral radius (maximum magnitude eigenvalue) of the operator, and as such our observations should hold for any media that satisfy them (Dukalski and de Vos, 2018). This is the main reason why we focus our analysis here on the artifacts arising at the leading iteration of the Marchenko redatuming scheme.

Effects of focusing depth in conjunction with subsampling

Because most datasets have fixed source and receiver apertures, the behavior of focusing functions and resulting redatumed fields changes with focal-point depth. Hence, we complement our observations above by studying the effects of focusing depth together with subsampling. Figure 8a and 8b show the focusing functions calculated by integrating on source without and with subsampling at a shallower focusing depth ($X_F = 0\,\mathrm{m}, Z_F = 1125\,\mathrm{m}$). Comparing Figure 8b and 3b, we see that the artifacts at far offset brought by the same subsampling appear to be stronger for the shallow focusing depth than those for the deep focusing depth. This effect can be explained by comparing the traveltime slopes of the two input focusing functions as shown in Figure 8c and 8d: because the shallower-depth focusing function in Figure 8c has steeper slopes at far offsets, the integrand events at far offsets will be more aliased than those from a deeper focal point (Figure 6), given a fixed subsampling rate.

Source-receiver reciprocity for Marchenko methods in laterally inhomogeneous media

The Marchenko methods have a requirement of monopoles and dipoles, either on source or on receiver side, as we show in equation 3. Because of the symmetrical geometry in previous examples, the source-receiver transpose yields same reflection record and therefore integrating on the dipole or the monopole dimension yields the same result in the Marchenko method for laterally homogeneous media, as shown by Figure 3. However, this may no longer be true for laterally inhomogeneous media, as, e.g., the angles of rays coming in and out at a fixed source-receiver pair may not be equal anymore. In practice, real dipoles are typically only available on the receiver side, for example, through particle velocity or acceleration measurements. On the source side, they are generally unavailable on offshore experiments because the source is monople in its nature. The common practice in industry where one needs a dipole on the source side, is to apply model-based corrections that would require knowledge of the local wavenumber and impedance at the source locations. Here, we show with numerical examples that for smoothly laterally varying 2D media, the error caused by integrating over the monopole dimension is generally negligible — so long as the near-surface properties in the vicinity of sources and receivers do not have pronounced variations. In the case where the near-surface properties vary rapidly laterally, in addition to obliquity factor, differences in local impedance at source and receiver locations must be taken into account.

The 2D model used in our test is shown in Figure 9. The full reflection data have 201 co-located sources (monopole) and receivers (dipole) with spacing intervals of 10 m lying within the range of $x = (3000\,\mathrm{m}, 5000\,\mathrm{m})$ at the acquisition surface with the time sampling rate of $dt = 2.4\,\mathrm{ms}$. The focal point is located at $(X_F = 4000\,\mathrm{m}, Z_F = 1000\,\mathrm{m})$. The coupled Marchenko system is solved with 13 iterations. Figure 10a-10c shows the Green's function obtained from SEM modeling, Marchenko redatuming by integrating on the dipole dimension and the monopole dimension, respectively. These Green's functions correspond to waves generated from a monopole source sitting at focal point and recorded at receivers at the acquisition surface, or vice versa, due to the source-receiver reciprocity. Shown in Figure 11a-11c are the focusing functions calculated with dipole and monopole integration as well as their difference, respectively. For primary estimation, Figure 12a shows the reference reflection data with source position $X_s = 4000\,\mathrm{m}$. Figure 12b-12d shows the result from dipole and monopole integration as well as their difference. Note that our observations are entirely consistent with well-established experience in SRME: amplitude effects — those related to the incidence-angle-dependent obliquity factors — are second order with respect to kinematic errors that result from sampling deficiencies.

Effects of acquisition aperture and subsampling in redatuming: complex model

To illustrate how acquisition sampling can impact results in a more realistic scenario, we study the effect of limited aperture, together with source integration and subsampling in the redatumed Green's function with a salt model, which has a constant density and varying wavespeed (Fig. 13). This model has also been used by Vargas and Vasconcelos (2020) in the context of scattering-based focusing. We choose this model such that the effects of density-related impedance changes do not play a role, which allows us to focus on the kinematics and reconstruction of the events — in any case. Because sampling-related inaccuracies are controlled by event slope (kinematics) and bandwidth, we expect that tests on a variable-density version of this model would yield the same conclusions as those we present below. The full reflection data have 201 co-located sources and receivers with spacing intervals of 40 m in the subsalt model. The acquisition spread lies within the range of $x = (4000\,\mathrm{m}, 12000\,\mathrm{m})$ at the acquisition surface with the time sampling rate of $dt = 4\,\mathrm{ms}$. The focal point is located $(X_F = 8130\,\mathrm{m}, Z_F = 4400\,\mathrm{m})$, as shown in Figure 13. The same subsampling scheme is used as shown in Figure 2b. Figure 14a shows the Green's functions obtained with full aperture. As observed in Figure 14b, subsampling by a ratio of 8 brings strong artifacts for the complex salt model. A comparison between Figure 14a and 14c illustrates that the acquisition with smaller aperture also increases aperture-induced artifacts in the Green's function. Figure 14d shows that a smaller aperture and subsampling compound into more complicated artifacts. Here all the Green's functions are calculated by solving the coupled Marchenko equations by inversion with the LSQR solver (Paige and Saunders, 1982; Ravasi and Vasconcelos, 2020).

Effects of subsampling in Marchenko primary estimation

Completing our analysis of subsampling effects on redatuming, here we study the receiver subsampling effects on Marchenko primary estimation in a four-layer model with co-located 201 sources and receivers, as shown by Figure 15. Figure 16a shows the reference reflection data with the source location $X_s = 0$ m, where four strong primaries and the ensuing relatively weak multiples can be observed. Figure 16b is the primary prediction result — using the algorithm presented above (see Algorithm 1) — without subsampling, where only four primaries are visible and the multiples are suppressed significantly. Figure 16c-16e are results of primary estimation with three different subsampling schemes (evenly zeroing out 66%, 75%, and 80%), calculated with 20 iterative substitutions, respectively. Here, as above, the choice of 20 iterations is arbitrary, chosen to be sufficiently higher then our observed number of iterations to achieve convergence on fully sampled data. Figure 16f shows the result using the same subsampling scheme as in Figure 16e, but calculated with LSQR instead of explicit Neumann iterations. As expected, the strength of artifacts increases with increasingly subsampled data. The errors in the first three iterations for the 75% subsampling scheme are given in Figure 17a-17c, which show that the major error comes from the first iteration and it can decrease in the subsequent iterations.

Figure 16e shows that the iterative substitution method fails to converge for this example when subsampling degree increases to 80%. Based on the theory of Neumann series expansion, in Figure 18 we examine the operator norm of $\mathbf{A} = \mathbf{W}_{\epsilon}^{t_2-\epsilon}\mathbf{R}^{\star}\mathbf{W}_{\epsilon}^{t_2-\epsilon}\mathbf{R}$ in equations 18 for different subsampling schemes as a function of time. In general, the operator norm first increases and then plateaus with time t_2. This occurs as more finite-energy arrivals are included by the windowing operator $\mathbf{W}_{\epsilon}^{t_2-\epsilon}$ as time increases, but the contribution of an increasing number of arrivals is offset by the decreasing energy of high-order multiples that arrive late (Zhang and Staring, 2018). As shown in Figure 18, the operator norm with full data for primary estimation with 20 iterations lies below that of the Marchenko redatuming for the chosen focal depth (0.8094), which satisfy the convergence condition $||\mathbf{A}|| < 1$. It is important to note that $||\mathbf{A}|| < 1$ guarantees convergence, whereas for $||\mathbf{A}|| > 1$, it may diverge (not guaranteed, but true for our example — for details on Neumann series convergence we refer to Dukalski and de Vos, 2018). Subsampling evenly by 66% and 75% brings the operator norm to around 1.2 and 2.1 respectively, where the iterations diverge slowly but lie within an acceptable range (see Figure 16c and 16d). Subsampling evenly by 80% further pushes the operator norm to around 3.1, resulting in a much faster divergence as shown in Figure 16e. Here we point out again that this operator norm analysis does not carry the same implications when the problem is solved without relying on explicitly evaluating the Neumann-series-based solution.

DISCUSSION

Our study with the four-layer model shows that for Marchenko redatuming the subsampling effects jointly depend on: (1) the choice of integration variable, and (2) the subsampling dimension in the multidimensional convolutions within the Marchenko scheme. Because of source-receiver reciprocity, the freedom to choose an appropriate integration variable can be advantageous in cases when only one of the dimensions (source or receiver) is subsampled. For the same reason, when the sampling of reflection data is symmetric with respect to the source and receiver dimensions, integrating on either dimension yields the same result, regardless of subsampling. When the data are regularly subsampled on one dimension, integrating on the other dimension yields inaccurate focusing results, with focusing function gaps at surface locations corresponding to the missing data. However, in this same sampling scenario, integrating on the subsampled dimension yields focusing functions with artifacts but no spatial gaps, with their strength affected by the chosen focusing depth. The analysis of the integrand gather shows that the mechanism behind lies at the integration within the multidimensional convolution between the reflection response and the focusing function formulated in the form of a matrix-vector multiplication in frequency domain. Naturally, we expect subsampling in both sources and receivers will compound and cause stronger artifacts together with gaps, compared with subsampling in a single dimension. In addition, limiting acquisition aperture will also bring artifacts (Sripanich and Vasconcelos, 2019), which can be compounded by the subsampling effects, as we show with our salt model example.

Further, we show with a model of mild lateral heterogeneity that conducting integration over the monopole dimension instead of the dipole brings negligible errors to both Marcheko systems here investigated, which may facilitate our choice of integration variable in combination with the subsampling scheme. This also reveals that the Marchenko methods are not highly sensitive to relatively small errors contained within the reflection data. Therefore, it implies that in practice interpolating the gaps of the input reflection data should be preferred over post processing the output focusing functions or Green's functions, as shown by Jia et al. (2019) and Staring and Wapenaar (2020) for 3D redatuming.

One important take-away from our results with different combinations of dipole and monopole field quantities is that, although theory strictly requires the use of dipole sources — which are not practically available — it is entirely feasible to rely on dipole data instead, e.g., acquired with multicomponent sensors. Though replacing dipole sources by receivers may violate spatial reciprocity in heterogeneous media, we believe in most offshore conditions the associated errors are likely negligible. In the absence of any dipole data, e.g., the case of conventional streamer data, we recommend that a monopole-to-dipole filter be applied in best-sampled domain, likely to be the receiver domain in streamer-based data. In the case of ocean-bottom nodes, which are multicomponent but often highly sparse, it may be better to apply dipole corrections on the more densely sampled source domain and perform convolutions over sources.

In the context of focusing and redatuming, it is important to point out that the behavior of subsampling-related errors in Marchenko operations is analogous to those occurring in Surface-Related Multiple Elimination (SRME). In SRME literature and practice (Dragoset et al., 2006, 2010; Verschuur, 2013), acquisition-related subsampling has been studied by many authors in many contexts — 2D, 3D, synthetic and field data. Throughout the literature in multiple elimination, subsampling effects have been extensively investigated, together with several approaches suggested to condition data for multiple suppression — including interpolation/regularization techniques. For example, in closed-loop SRME (Lopez and Verschuur. 2015), one may use a focal transformation and a sparse norm regularization to remove the undersampling noise. Although our study begins to highlight the connections between these methods, we expect more about Marchenko can be learned from what has been studied in the context of SRME — e.g., by taking inspiration from data conditioning approaches used in that context. However, appropriately translating SRME lessons into Marchenko practice will require further testing and research, particularly in the context of field data examples.

Though here we base our discussions on 2D examples, the arguments we build regarding the integration over monopole fields are general, and as such in principle apply to 3D media, i.e., having both source and receiver integrals each act on a plane of source/receiver coordinates. We point out that the work of Ravasi and Vasconcelos (2020) contains examples of subsampling 3D Marchenko operators — indeed in agreement with this study. Their example does further highlight that while aliasing effects in 3D follows the same patterns as we present here, they can be lower in magnitude when either source or receiver integration is subsampled in only one of the two spatial coordinates. This observation is likely to depend on the degree of subsampling as well as on the degree of complexity — due to the subsurface heterogeneity — present in the 3D wavefields that make up the reflection operator.

A study of subsampling effects on the primary estimation based on the projected Marchenko system shows a similar pattern of artifacts that appear in the original coupled Marchenko system, which can be explained by the common multidimensional convolution and correlation between reflection data and focusing functions. As expected, the artifacts increase with degree of subsampling and may cause divergence issue with iterative substitution when subsamping to a certain extent, which is illustrated by the analysis of the time-dependent operator norm lying in the core of the iteration. This problem can be mitigated by using more robust iterative linear solvers, such as LSQR — but this would likely come at greater computational cost as such solvers tend to convergence more slowly than the Neumann series, thus requiring a larger number of iterations (i.e., of operator evaluations, Dukalski and de Vos, 2018). In our case, LSQR yields consistent results, as opposed to Neumann-series-based iterative substitution, when presented with data with high degrees of subsampling. When the data are well-sampled, the Neumann-series iterative scheme and the LSQR solver perform equally well. As in using the coupled Marchenko system for redatuming, the errors caused by subsampling decrease rapidly with the number of iterations — provided the Neumann series remains stable.

CONCLUSION

By relying on representative numerical cases to mimic acquisition scenarios over varying subsurface complexity, we provide a study of the acquisition-related subsampling effects on the 2D Marchenko focusing, redatuming (original coupled Marchenko system) and primary estimation (projected Marchenko system) to shed light on the underlying physical and numerical mechanisms. For Marchenko focusing and redatuming, we show that the artifacts brought by subsampling are rooted in the integration within the multidimensional convolution between the reflection response and the focusing function, which also applies to primary estimation because of how similar the underlying operations are. These subsampling effects depend jointly on the integration variable choice and the subsampled dimension (dipole source or receiver). Artifacts appear without spatial gaps when these two are identical and spatial gaps are present with artifacts for different dimensions. Our study also shows that integrating on the monopole dimension also gives very close approximation to the results of both Marchenko systems for smoothly laterally varying media. In this regard, future studies are expected regarding the sampling requirement for convergence, the interpolation accuracy, etc. The artifacts in redatumed Greens' functions depend on the reflection data sampling as well as focusing depths. In imaging, these artifacts will very likely cause small errors but for full-waveform inversion (FWI), time-lapse and reservoir characterization, these could lead to larger errors.

Our study focuses only on regularly subsampling in one dimension of the input reflection data, i.e., source or receiver dimension. Meanwhile, the conclusions drawn from our study are limited to the 2D case. For 3D, the irregular subsampling effects are likely more complicated, due to 2D integration over both the source and receiver dimension, particularly in the case of highly complex media. Our results can inform acquisition design, but more importantly they tell us how to handle single and multicomponent data for Marchenko applications, while providing insight that can help in ensuring the quality of data conditioning approaches for Marchenko applications.

ACKNOWLEDGMENTS

We thank all the sponsors of UCSI (the Utrecht Consortium for Subsurface Imaging) for funding this project. We also thank the open source matlab code Spot for providing a linear-operator toolbox that allows us to compute the operator norm. We thank the software Salvus for spectral-element-based modeling.

REFERENCES

Afanasiev, M., C. Boehm, M. van Driel, L. Krischer, M. Rietmann, D. A. May, M. G. Knepley, and A. Fichtner, 2019, Modular and flexible spectral-element waveform modelling in two and three dimensions: Geophysical Journal International, **216**, no. 3, 1675–1692.

Dragoset, B., I. Moore, and C. Kostov, 2006, The impact of field-survey characteristics on surface-related multiple attenuation: Geophysical Prospecting, **54**, no. 6, 781–791.

Dragoset, B., E. Verschuur, I. Moore, and R. Bisley, 2010, A perspective on 3D surface-related multiple elimination: Geophysics, **75**, no. 5, 75A245–75A261.

Dukalski, M., and K. de Vos, 2018, Marchenko inversion in a strong scattering regime including surface-related multiples: Geophysical Journal International, **212**, no. 2, 760–776.

Elison, P., M. S. Dukalski, K. de Vos, D. J. van Manen, and J. O. A. Robertsson, 2020, Data-driven control over short-period internal multiples in media with a horizontally layered overburden: Geophysical Journal International, **221**, no. 2, 769–787.

Haindl, C. M., M. R. F. Broggini, and D.-J. van Manen, 2018, Using sparsity to improve the accuracy of Marchenko imaging given imperfect acquisition geometries: 80th Annual International Conference and Exhibition, EAGE, Extended Abstracts.

Jia, X., Y. Zhao, and R. Snieder, 2019, Data interpolation for 3D Marchenko Green's function retrieval: 89th Annual International Meeting, SEG, Expanded Abstracts, 4725–4729.

Lopez, G. A., and D. J. Verschuur, 2015, Closed-loop surface-related multiple elimination and its application to simultaneous data reconstruction: Geophysics, **80**, no. 6, V189–V199.

Paige, C. C., and M. A. Saunders, 1982, LSQR: An algorithm for sparse linear equations and sparse least squares: ACM Transactions on Mathematical Software, **8**, no. 1, 43–71.

Ravasi, M., 2017, Rayleigh-Marchenko redatuming for target-oriented, true-amplitude imaging: Geophysics, **82**, no. 6, S439–S452.

Ravasi, M., and I. Vasconcelos, 2020, On the implementation of large-scale integral operators with modern hpc solutions – Application to 3D Marchenko imaging by least-squares inversion: arXiv:2011.11120 [physics.geo-ph].

Sripanich, Y., and I. Vasconcelos, 2019, Effects of aperture on Marchenko focussing functions and their radiation behaviour at depth: Geophysical Prospecting, **67**, no. 2, 443–454.

Staring, M., and K. Wapenaar, 2020, Three-dimensional Marchenko internal multiple attenuation on narrow azimuth streamer data of the Santos Basin, Brazil: Geophysical Prospecting, **68**, no. 6, 1864–1877.

van der Neut, J., J. Thorbecke, K. Wapenaar, and E. Slob, 2015a, Inversion of the multidimensional Marchenko equation: 77th Annual International Conference and Exhibition, EAGE, Extended Abstracts.

van der Neut, J., I. Vasconcelos, and K. Wapenaar, 2015b, On Green's function retrieval by iterative substitution of the coupled Marchenko equations: Geophysical Journal International, **203**, no. 2, 792–813.

van der Neut, J., and K. Wapenaar, 2016, Adaptive overburden elimination with the multidimensional Marchenko equation: Geophysics, **81**, no. 5, T265–T284.

van IJsseldijk, J., and K. Wapenaar, 2020, Adaptation of the iterative Marchenko scheme for imperfectly sampled data: Geophysical Journal International, **224**, no. 1, 326–336.

Vargas, D., and I. Vasconcelos, 2020, Rayleigh-Marchenko redatuming using scattered fields in highly complex media: 82nd Annual International Conference and Exhibition, EAGE, Extended Abstracts.

Verschuur, D., 2013, Seismic multiple removal techniques: past, present and future (revised edition): EAGE.

Verschuur, D., A. Berkhout, and C. Wapenaar, 1992, Adaptive surface-related multiple elimination: Geophysics, **57**, no. 9, 1166–1177.

Wapenaar, K., J. Thorbecke, J. Van der Neut, F. Broggini, E. Slob, and S. R., 2014, Marchenko imaging: Geophysics, **79**, no. 3, WA39–WA57.

Wapenaar, K., and J. van IJsseldijk, 2020, Discrete representations for Marchenko imaging of imperfectly sampled data: Geophysics, **85**, no. 2, A1–A5.

Zhang, L., and M. Staring, 2018, Marchenko scheme based internal multiple reflection elimination in acoustic wavefield: Journal of Applied Geophysics, **159**, 429–433.

Zhang, L., J. Thorbecke, K. Wapenaar, and E. Slob, 2019a, Data-driven internal multiple elimination and its consequences for imaging: A comparison of strategies: Geophysics, **84**, no. 5, S365–S372.

———, 2019b, Transmission compensated primary reflection retrieval in the data domain and consequences for imaging: Geophysics, **84**, no. 4, Q27–Q36.

Figure 1. (a) Illustration for equations 5, where the integration is conducted over the dipole source dimension with the receiver being monopole. (b) The same for equation 9, where the integration is conducted over the dipole receiver dimension, but with the source being monopole. For each frequency slice, $\hat{R}$ and $\hat{R}^T$ are 2D matrices and focusing functions $\hat{f}^+_{1d}$ and $\hat{f}^-_{1,K=0}$ are 1D vectors for a fixed focal point X_F.

Figure 2. (a) The density profile of the layered model, same as in van der Neut et al. (2015b). The magenta circles represent two focal point locations (($X_F = 0\,\mathrm{m}, Z_F = 1125\,\mathrm{m}$) and ($X_F = 0\,\mathrm{m}, Z_F = 2670\,\mathrm{m}$)). (b)-(c) The sampling masks for regular subsampling in the source and receiver dimensions, respectively, where the white represent the missing data. Here, subsampling is achieved by zeroing out 7 of every 8 sources or receivers. The red stars and white triangles indicate the source and receiver locations.

Figure 3. For the layered model in Figure 2a with the focal position ($X_F = 0\,\mathrm{m}, Z_F = 2670\,\mathrm{m}$): (a) the reference focusing function without subsampling. Focusing functions are then presented for different sampling and integration scenarios: (b) subsampling and integration over sources, the same as subsampling and integration over receivers, (c) subsampling over sources and integrating over receivers, the same as subsampling over receivers and integrating over sources. The magenta circles point out the major differences. (d) the zoomed-in traces for comparison of focusing functions in (a), (b) and (c) at far offset ($X_r = -910\,\mathrm{m}$), location shown by the yellow solid line) in red, blue and black, respectively. (e)-(g) are the zoomed-in plots of (a)-(c) around the circles, respectively.

Figure 4. Summary of the four cases of integration versus subsampling. (a) and (b) Integrating and subsampling in the same dimension (dipole source or receiver) are equivalent and will result in artifacts without spatial gaps. (c) and (d) Integrating and subsampling in

different dimensions are equivalent and will cause spatial gaps together with artifacts. The squared matrices are interpreted as the $\hat{R}$ or $\hat{R}^T$ matrices of Figure 1. The yellow arrow points at the integrated dimension. The magenta and gray squares represent sampled and missing data, respectively.

Figure 5. For the layered model in Figure 2a with the focal position ($X_F = 0\,\mathrm{m}, Z_F = 2670\,\mathrm{m}$), focusing functions in $f-k$ domain: (a) the reference focusing function without subsampling corresponding to Figure 3a. (b) the focusing function corresponding to Figure 3b. (c) the difference between (a) and (b) normalized by the maximum value of (a). (d) the focusing function corresponding to Figure 3c. (e) the difference between (a) and (d) normalized by the maximum value of (a). The color bars in (c) and (e) denote the corresponding relative errors.

Figure 6. For the layered model in Figure 2a with the focal position ($X_F = 0\,\mathrm{m}, Z_F = 2670\,\mathrm{m}$) corresponding to Figure 3b, i.e. subsampling and integrating over the same dimension: (a) the convolution gather from $\mathbf{R}\boldsymbol{f}^{+}_{1d}$ for the output near-offset receiver position $X_r = -40\,\mathrm{m}$. (b) Integration of (a), with scaling by the subsampled source interval. The blue and red lines represent the results calculated with and without subsampling, respectively. (c) and (d) as well as (e) and (f) are counterpart to (a) and (b), but for $X_r = -400\,\mathrm{m}$ (mid-offset) and $X_r = -960\,\mathrm{m}$ (far-offset), respectively.

Figure 7. For the layered model in Figure 1a with focal point at ($X_F = 0\,\mathrm{m}, Z_F = 2670\,\mathrm{m}$): (a)-(d) The error of focusing function caused by subsampling and integrating on the same dimension (corresponding to Figure 3b) in the first, second, third, and fourth iteration, respectively. All the amplitudes are clipped at 1% of the strongest arrival in Figure 3a.

Figure 8. For the layered model in Figure 2a with a shallower focal point at ($X_F = 0\,\text{m}, Z_F = 1125\,\text{m}$): (a) the reference focusing function without subsampling. (b) Idem, calculated by subsampling and integrating over sources, using the sampling mask shown in Figure 2b. (c)-(d) show the initial focusing functions used for the focusing depths at $Z_F = 1125\,\text{m}$ and $Z_F = 2670\,\text{m}$, respectively, at fixed aperture.

Figure 9. (a) Velocity and density profiles of the 2D model used in the source-receiver transpose study for the Marchenko focusing and primary estimation. The magenta dot denotes the location of focal point ($x = 4000\,\text{m}$, $z = 1000\,\text{m}$). The red stars and white triangles indicate the source and receiver locations.

Figure 10. For the 2D model shown in Figure 9: (a)-(c) the Green's function from forward modeling, from Marchenko redatuming by integrating on the dipole dimension, and from Marchenko redatuming by integrating on the monopole dimension, respectively.

Figure 11. (a)-(b): Focusing functions calculated by integrating on the dipole and monopole dimension, respectively. (c) the difference between (a) and (b), of which the amplitude is multiplied by a gain factor of 10.

Figure 12. Results of primary estimation for the 2D model shown in Figure 9. (a) the reference reflection data with source at $x = 4000\text{m}$. (b) primary estimation from integrating on the dipole dimension. (c) Idem, from integrating on the monopole dimension. (d) the difference between (b) and (c), of which the amplitude is multiplied by a gain factor of 10.

Figure 13. The velocity profile of the salt model with constant density. The magenta circle denotes the focal point ($X_F = 8130\,\text{m}, Z_F = 4400\,\text{m}$) located beneath the salt body. The red stars and white triangles indicate the source and receiver locations.

Figure 14. For the subsalt model with the focal point at ($X_F = 8130\,\text{m}, Z_F = 4400\,\text{m}$):

(a) the reference Green's function without subsampling. (b) The redatumed Green's function calculated by subsampling and integrating over source and integrating on source. The same subsampling scheme is used as shown in Figure 2b. (c) and (d) are difference plots between true and estimated responses use 2/3 of the original data aperture: (c) is from fully sampled data, while (d) is from subsampled data. In (c-d), the missing traces indicate the part of the data that was removed for these tests.

Figure 15. (a)-(b) Velocity and density profiles of the four layer model used for primary estimation, respectively. The red stars and white triangles indicate the source and receiver locations.

Figure 16. Comparison of the results of primary estimation with different subsampling scheme: (a) The reference reflection data for a shot located at $x = 0\,\mathrm{m}$. (b)-(e) Results of primary estimation with full data and subsampled data of three different subsampling schemes (evenly zeroing out 66%, 75%, and 80%), calculated with iterative substitution, respectively. (f) Results of primary estimation with subsampled data used in (e) calculated with LSQR inversion.

Figure 17. (a)-(c) Error in the first 3 iterations of primary estimation caused by subsampling (evenly zeroing out 75% of the 201 sources). All the amplitudes are clipped at 2% of the strongest arrival in Figure 16a.

Figure 18. (a) Comparison of operator norm of iterative substitution in primary estimation with different subsampling schemes (100% data, regularly zeroing out 66%, 75%, 80%, respectively), as well as in the Marchenko redatuming with full data for the same model. Here, we note that the Marchenko redatuming operator norm corresponds to fixed focal point at depth — thus not being one-to-one comparable with primary estimation on the

acqusition surface — but we choose to show it here merely to indicate that operator norm for redatuming is not time-dependent.

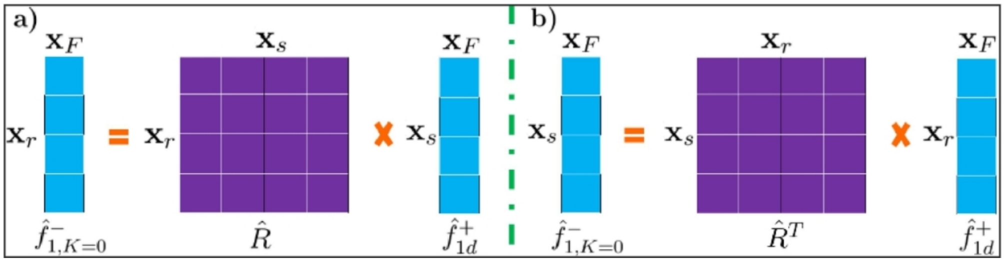

Figure 1. (a) Illustration for equations~ ef{eq:SouInt}, where the integration is conducted over the dipole source dimension with the receiver being monopole. (b) The same for equation~ ef{eq:RecInt}, where the integration is conducted over the dipole receiver dimension, but with the source being monopole. For each frequency slice, $\hat{R}$ and $\hat{R}^T$ are 2D matrices and focusing functions $\hat{f}^+_{1d}$ and $\hat{f}^-_{1,K=0}$ are 1D vectors for a fixed focal point X_F.

117x29mm (300 x 300 DPI)

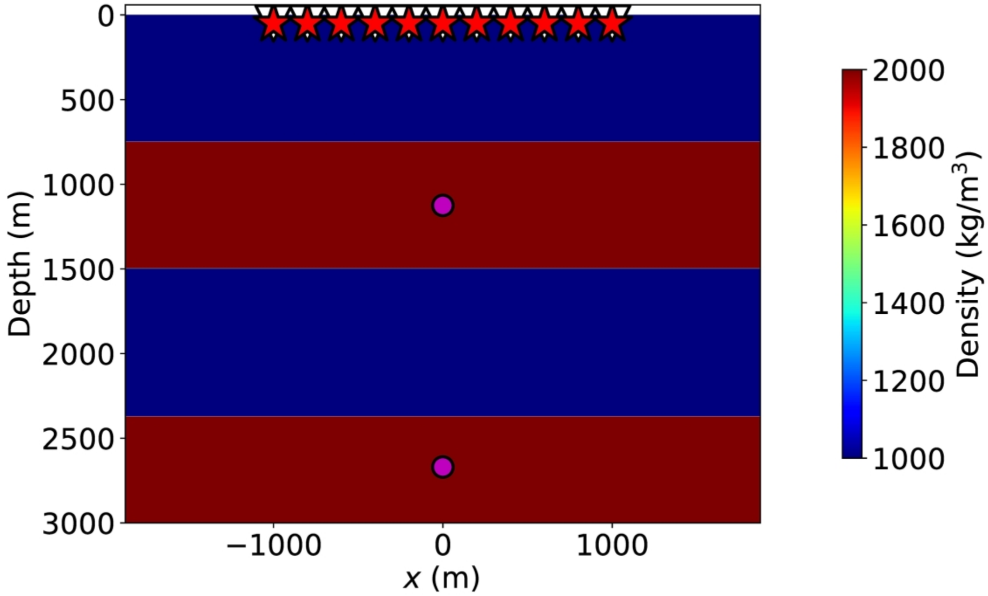

Figure 2. (a) The density profile of the layered model, same as in \citet{Joosta}. The magenta circles represent two focal point locations ($(X_F=0\: ext{m}, Z_F=1125\: ext{m})$ and $(X_F=0\: ext{m}, Z_F=2670\: ext{m})$).

242x148mm (300 x 300 DPI)

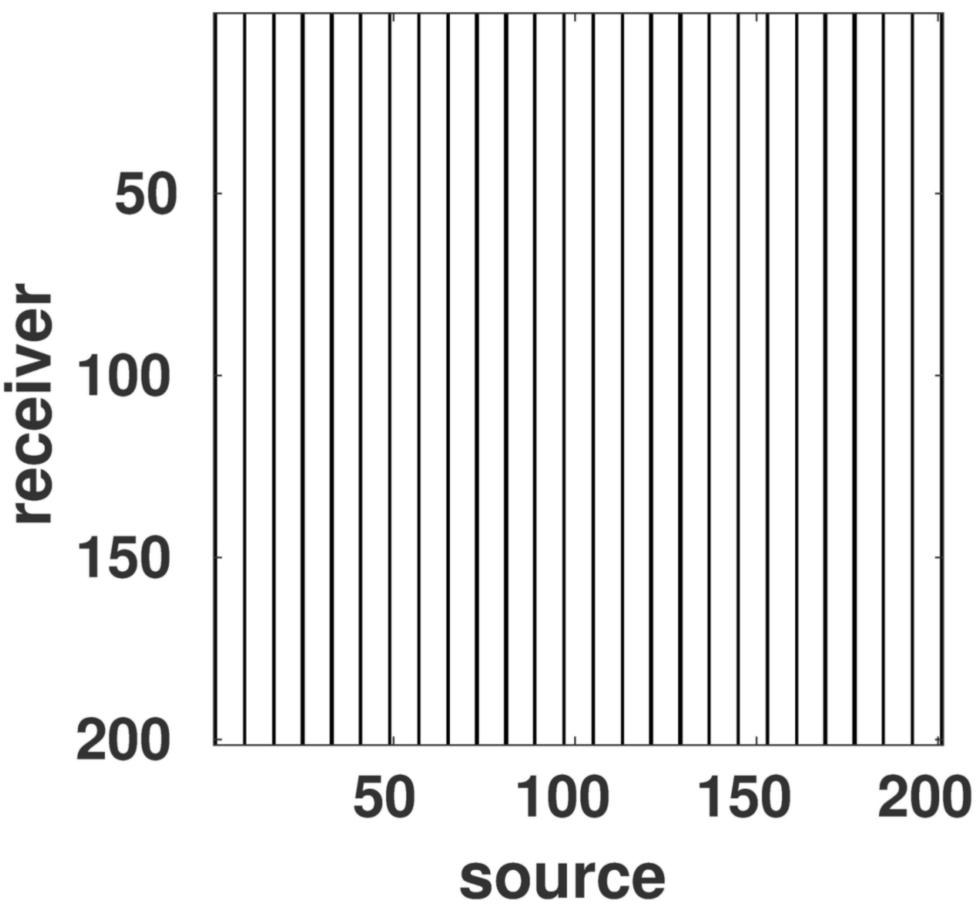

Figure 2.(b)The sampling masks for regular subsampling in the source dimension, where the white represent the missing data. Here, subsampling is achieved by zeroing out 7 of every 8 sources or receivers. The red stars and white triangles indicate the source and receiver locations.

122x108mm (300 x 300 DPI)

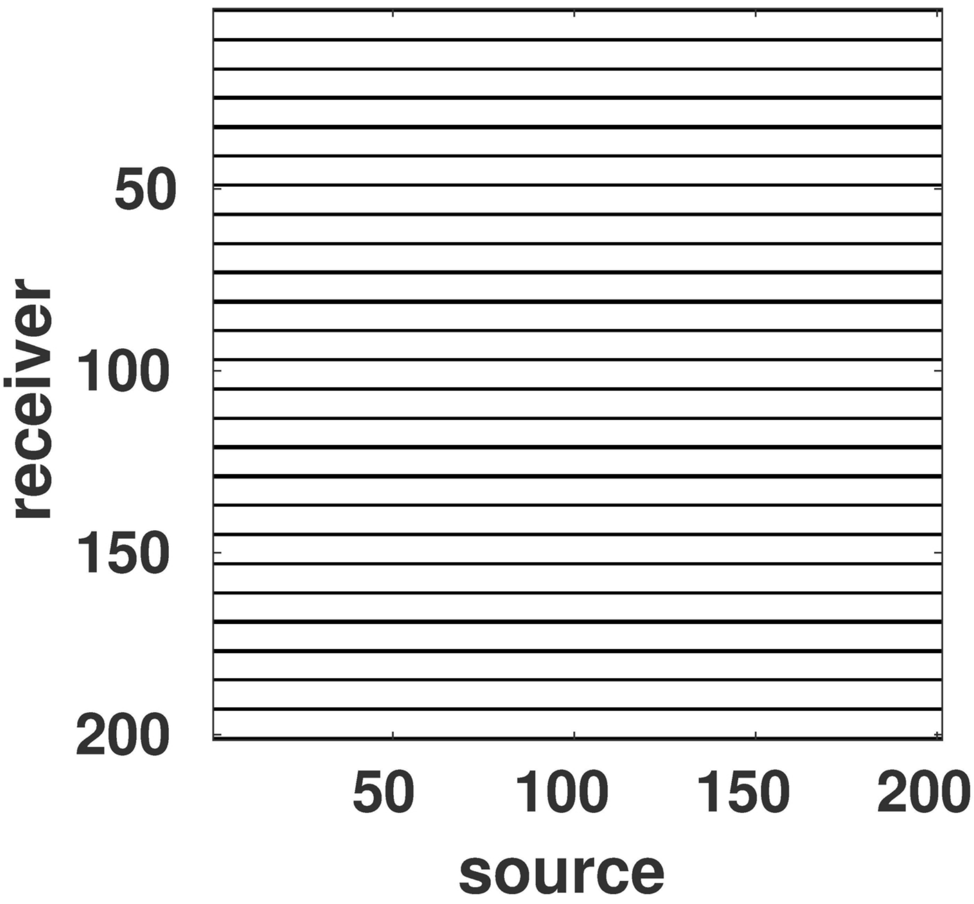

Figure 2. (c) The sampling masks for regular subsampling in the receiver dimensions.

122x108mm (300 x 300 DPI)

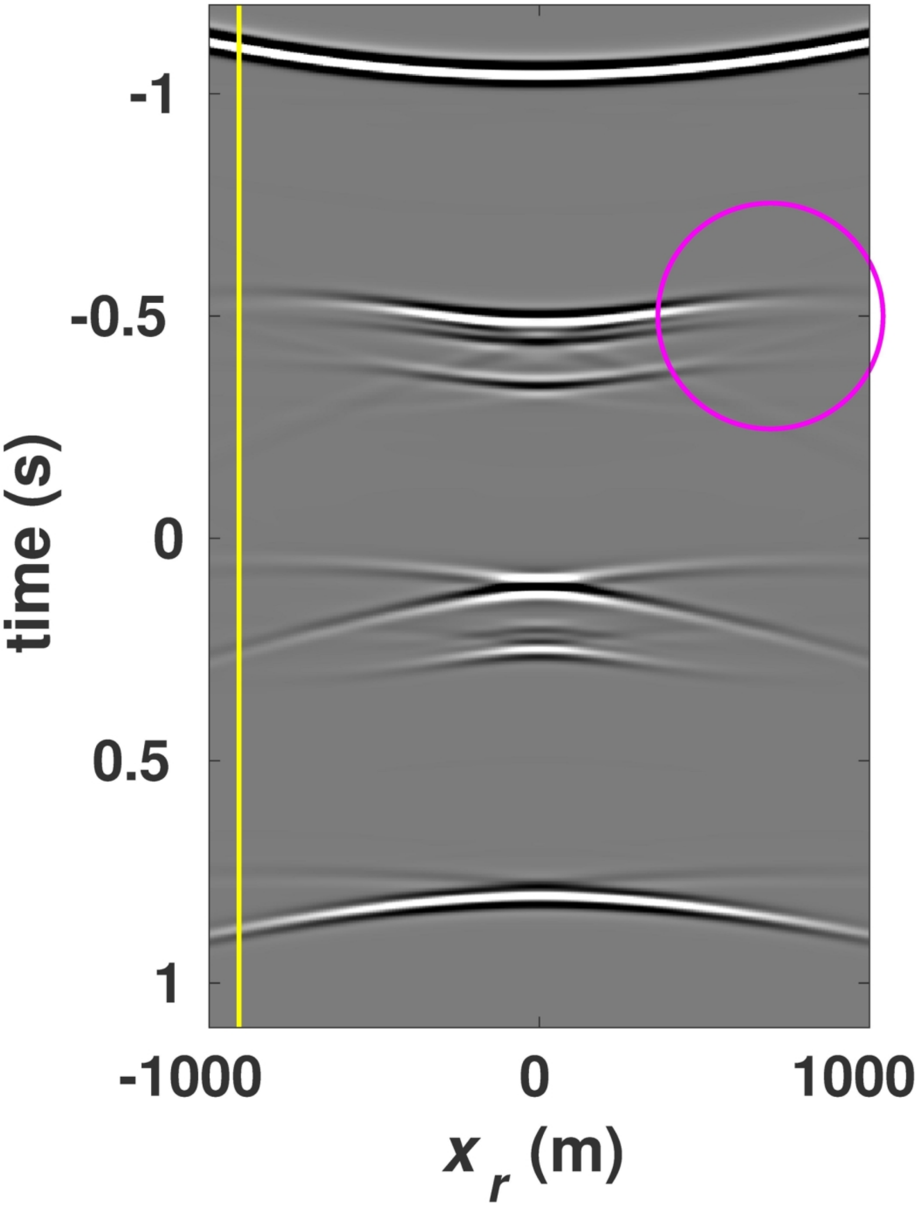

Figure 3. (a) For the layered model in Figure 2a with the focal position $(X_F=0\: ext{m}, Z_F=2670\: ext{m})$, the reference focusing function without subsampling.

147x187mm (300 x 300 DPI)

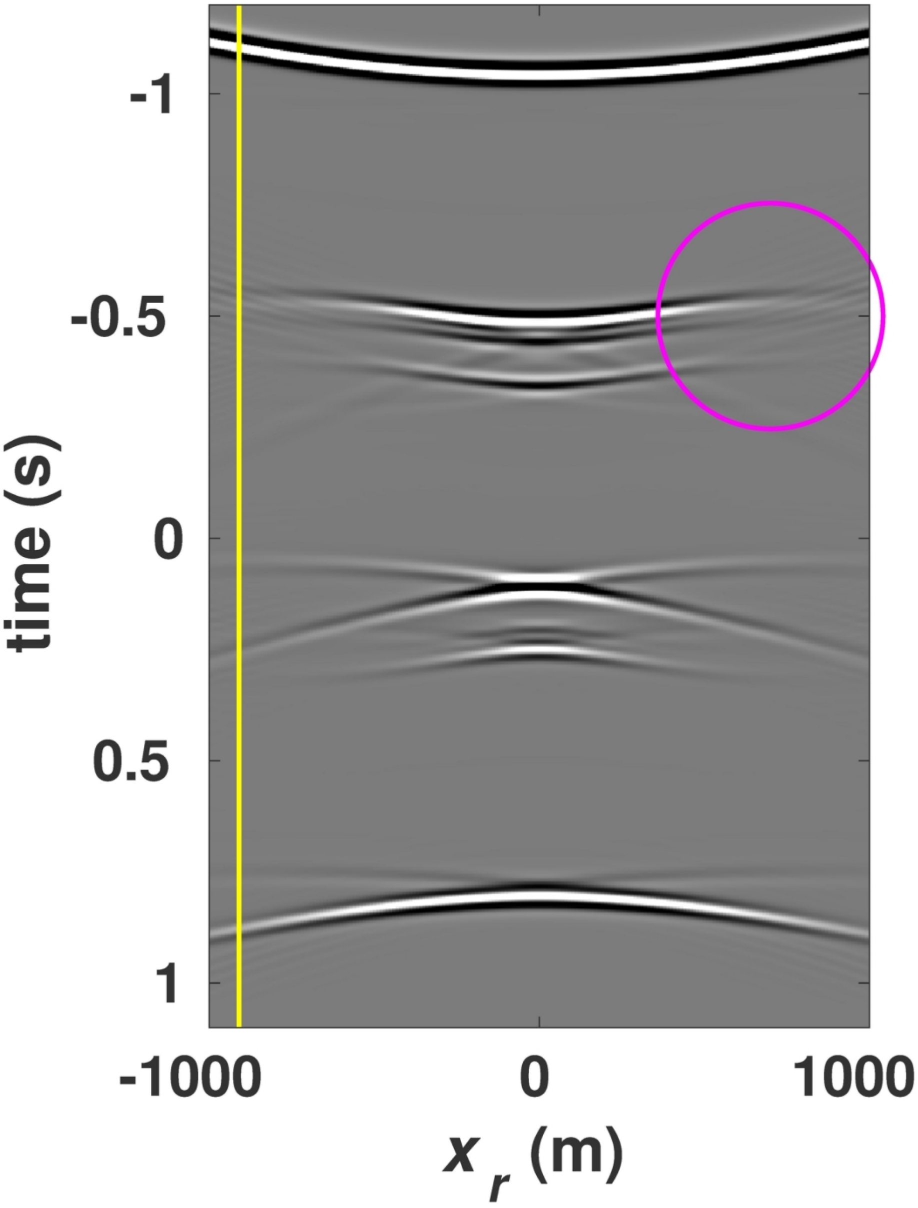

Figure 3 (b) For the layered model in Figure 2a with the focal position $(X_F=0\: ext{m}, Z_F=2670\: ext{m})$: focusing function for subsampling and integration over sources, the same as subsampling and integration over receivers.

147x187mm (300 x 300 DPI)

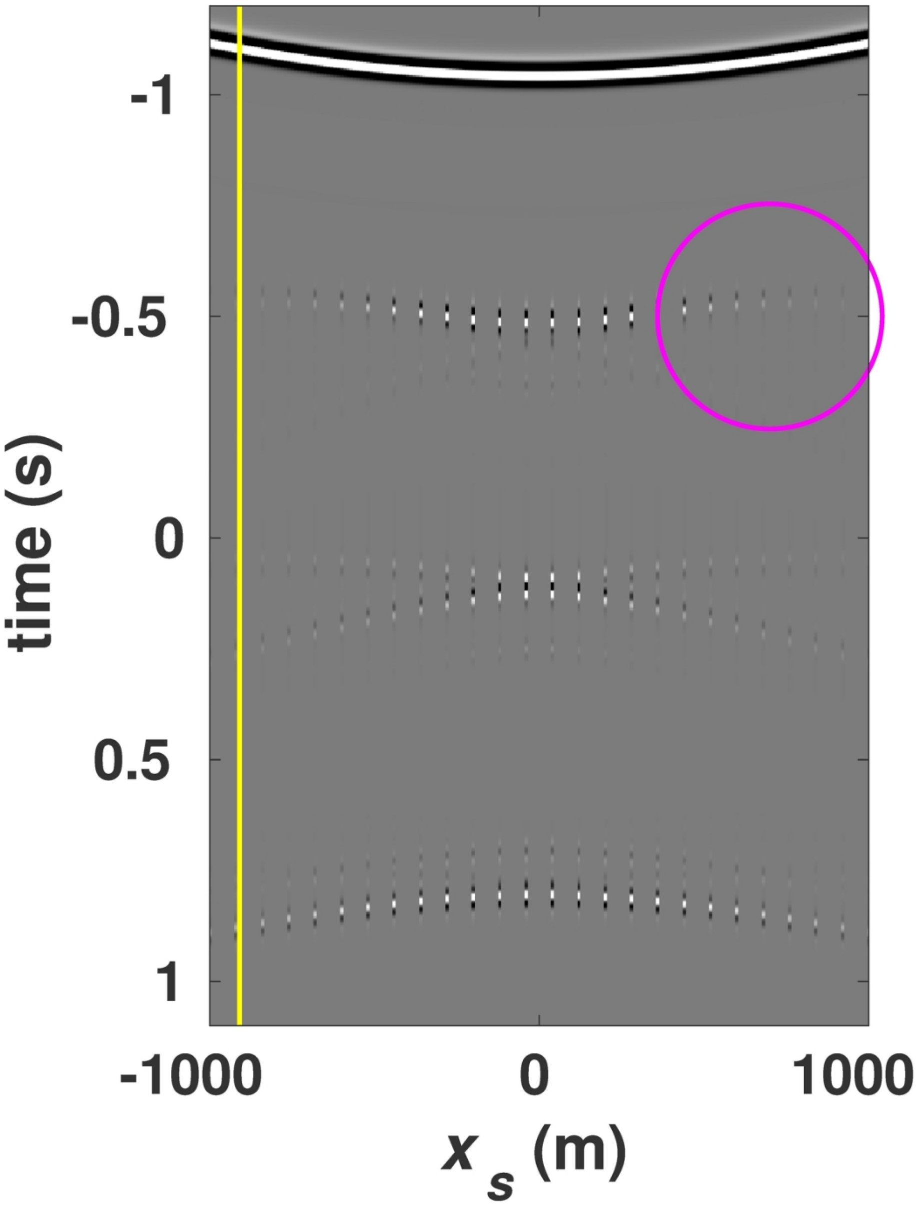

Figure 3(c) For the layered model in Figure 2a with the focal position $(X_F=0\: ext{m}, Z_F=2670\: ext{m})$, focusing functions for subsampling over sources and integrating over receivers, the same as subsampling over receivers and integrating over sources. The magenta circles point out the major differences.

147x188mm (300 x 300 DPI)

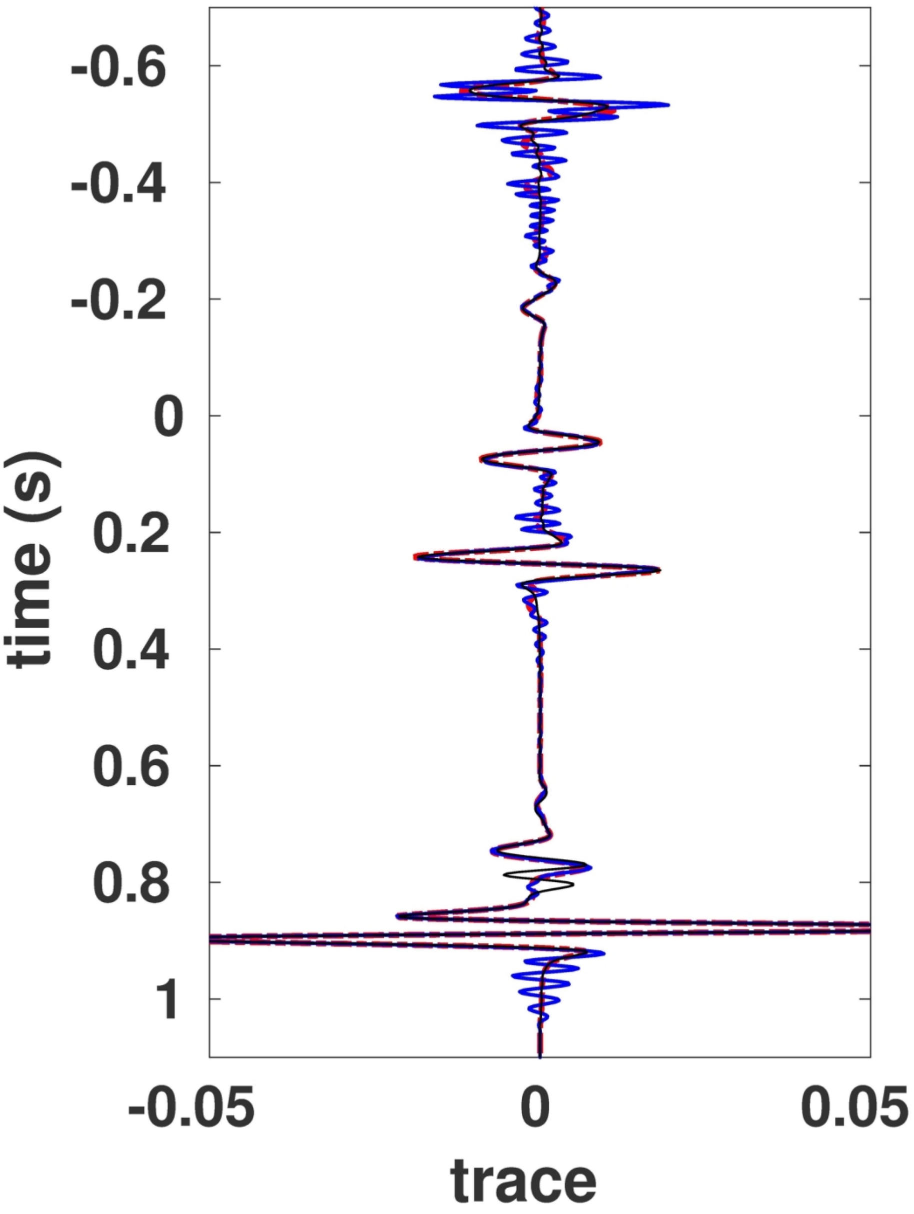

Figure 3(d). For the layered model in Figure 2a with the focal position $(X_F=0\: ext{m}, Z_F=2670\: ext{m})$, zoomed-in traces for comparison of focusing functions in (a), (b) and (c) at far offset $(X_r=-910\: ext{m})$, location shown by the yellow solid line) in red, blue and black, respectively.

146x187mm (300 x 300 DPI)

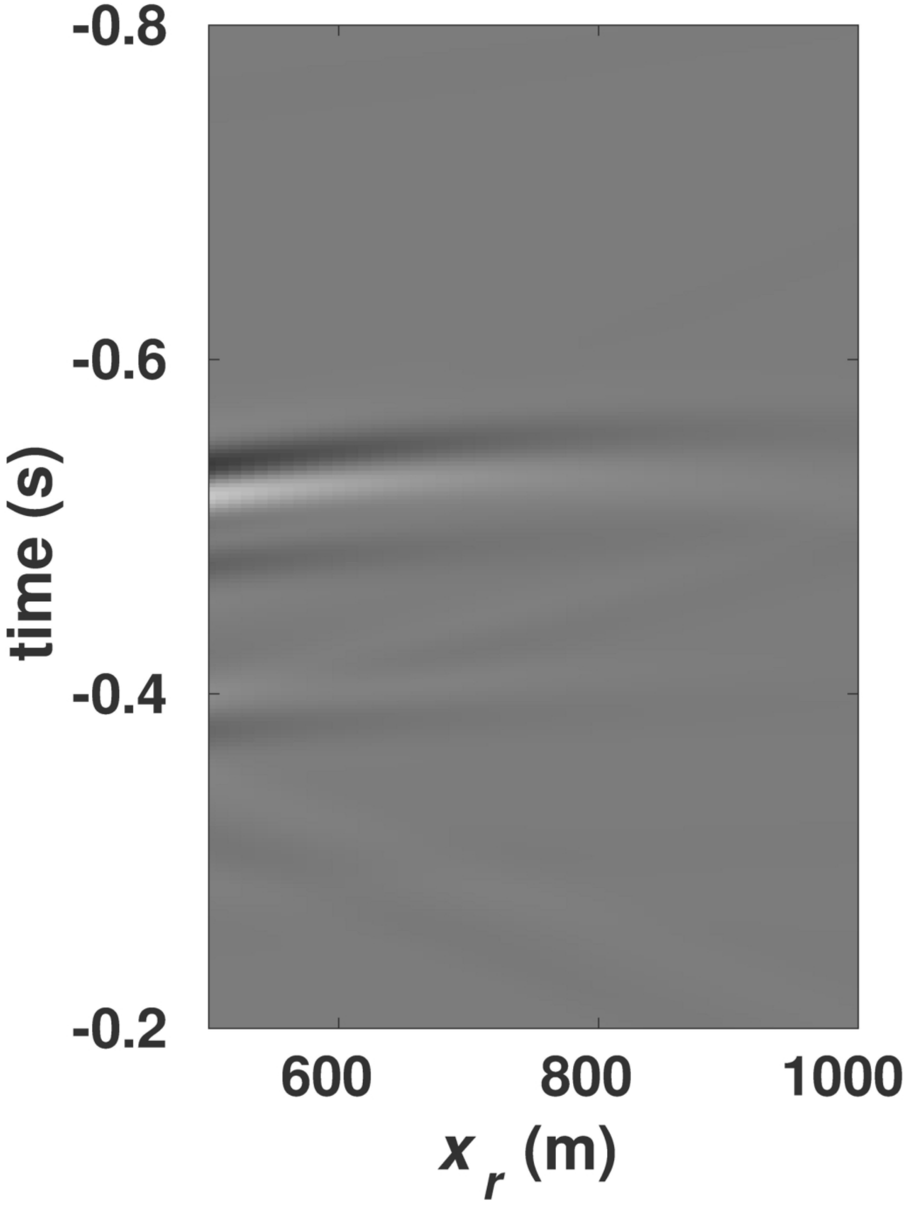

Figure 3(e). For the layered model in Figure 2a with the focal position $(X_F=0\: ext{m}, Z_F=2670\: ext{m})$, zoomed-in plots of Figure 3(a) around the circles.

147x190mm (300 x 300 DPI)

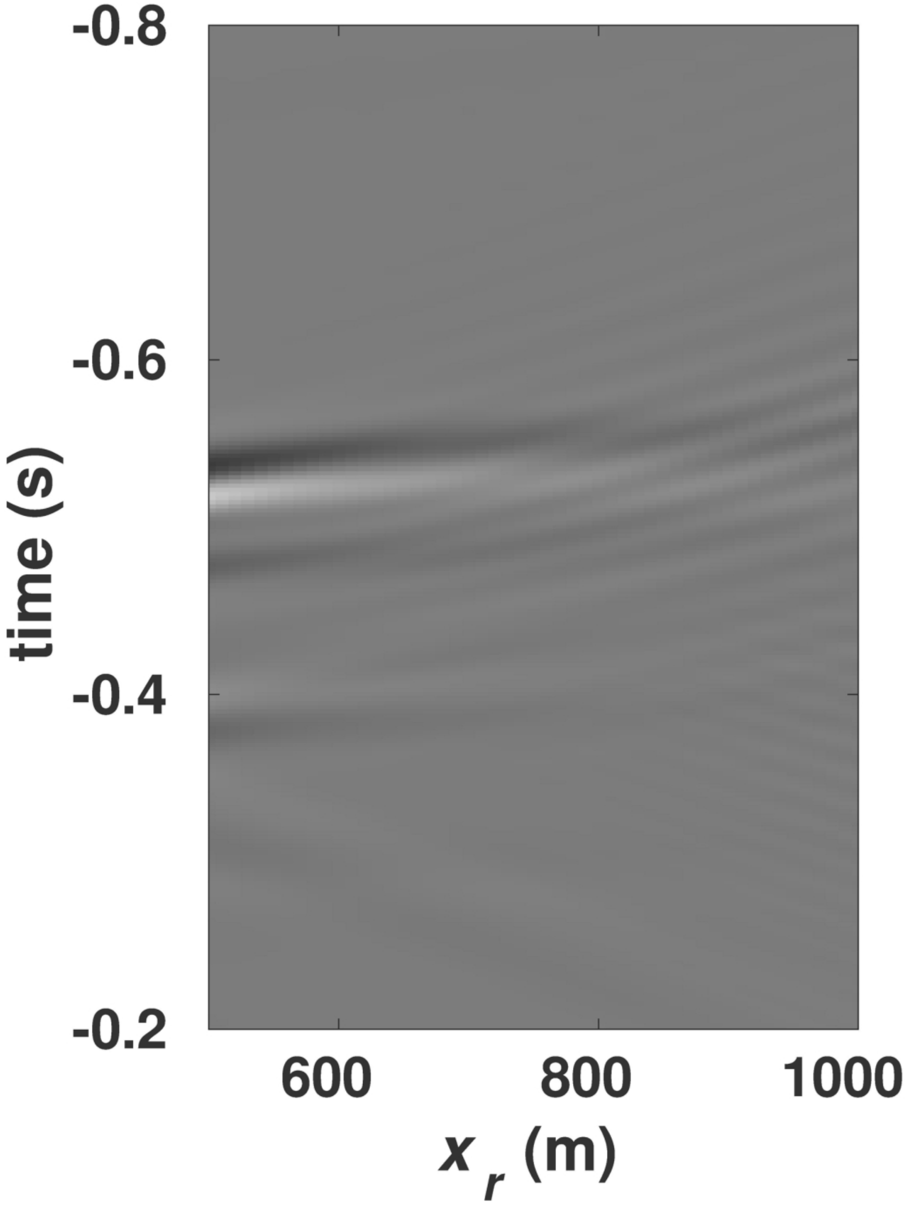

Figure 3(f). For the layered model in Figure 2a with the focal position $(X_F=0\: ext{m}, Z_F=2670\: ext{m})$, zoomed-in plots of Figure 3(b) around the circles.

147x190mm (300 x 300 DPI)

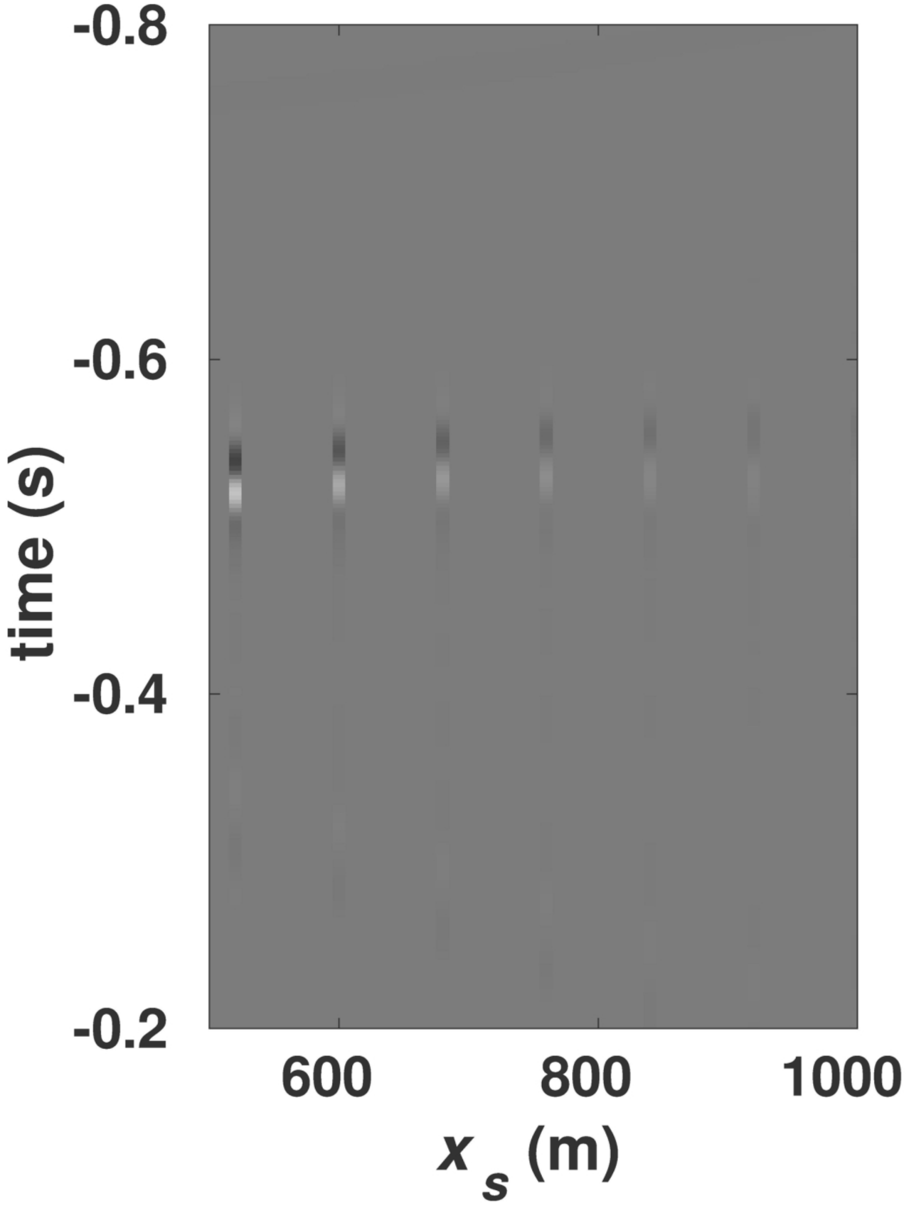

Figure 3(g). For the layered model in Figure 2a with the focal position $(X_F=0\: ext{m}, Z_F=2670\: ext{m})$, zoomed-in plots of Figure 3(c) around the circles.

147x191mm (300 x 300 DPI)

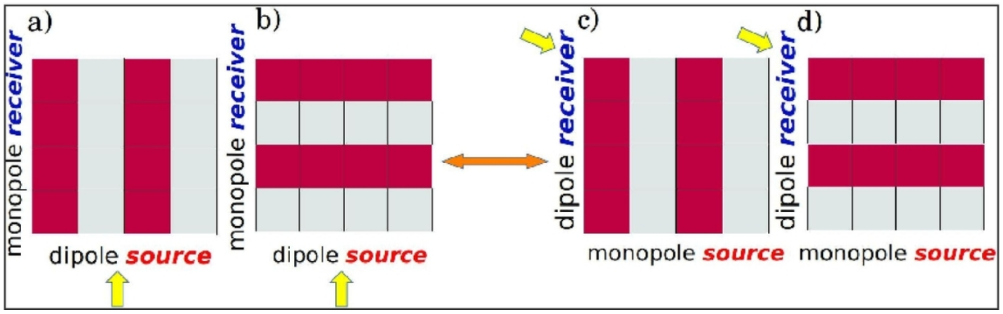

Figure 4. Summary of the four cases of integration versus subsampling. (a) and (b) Integrating and subsampling in the same dimension (dipole source or receiver) are equivalent and will result in artifacts without spatial gaps. (c) and (d) Integrating and subsampling in different dimensions are equivalent and will cause spatial gaps together with artifacts. The squared matrices are interpreted as the $\hat{R}$ or $\hat{R}^T$ matrices of Figure 1. The yellow arrow points at the integrated dimension. The magenta and gray squares represent sampled and missing data, respectively.

115x35mm (300 x 300 DPI)

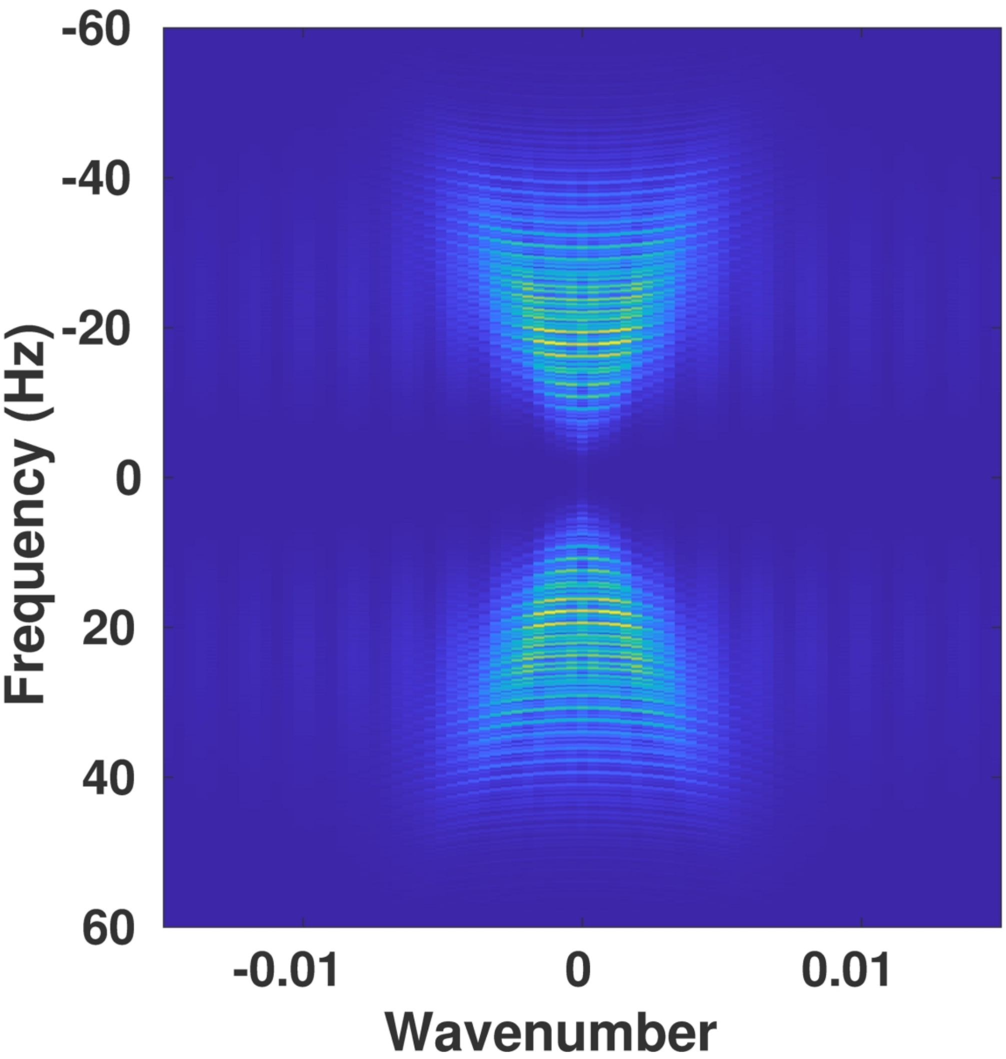

Figure 5(a). The focusing functions in $f-k$ domain without subsampling, corresponding to Figure 3a.

182x190mm (300 x 300 DPI)

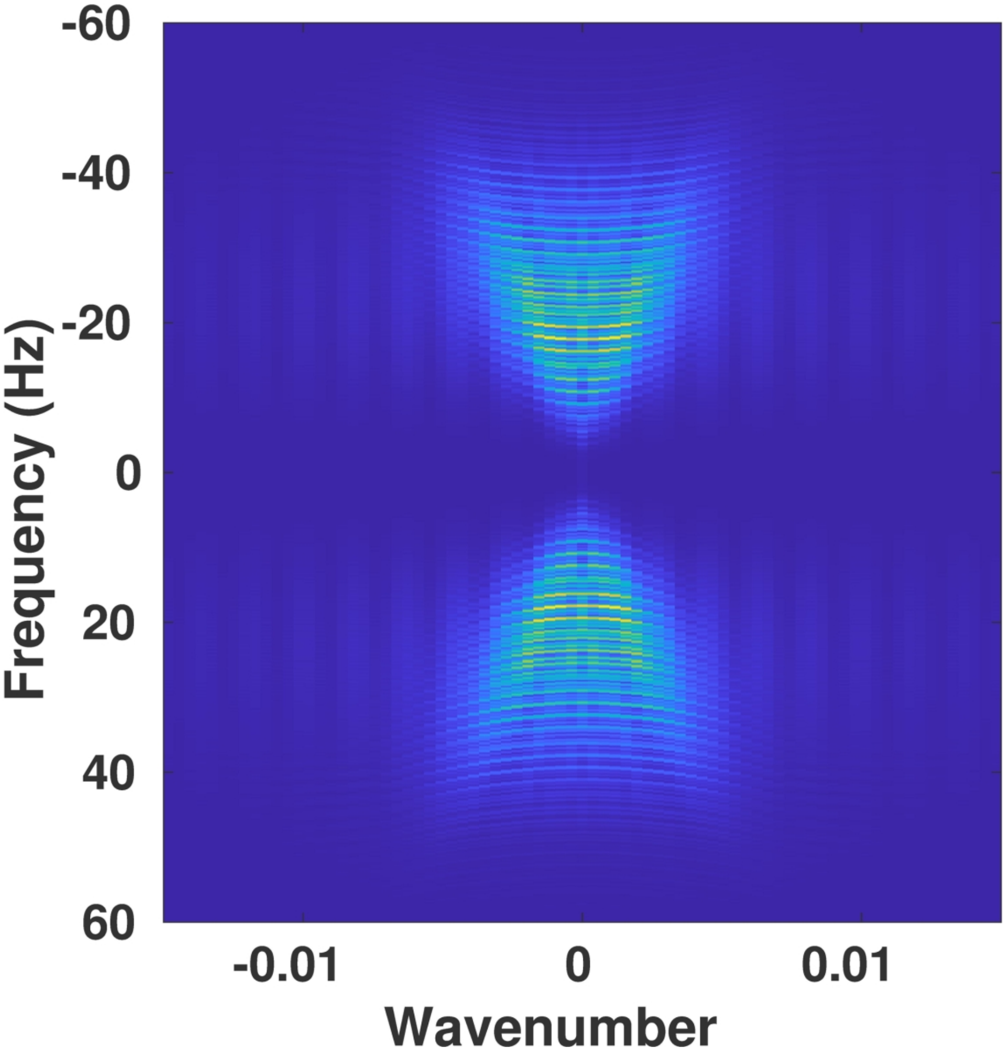

Figure 5(b). The focusing functions in $f-k$ domain, corresponding to Figure 3b.

182x190mm (300 x 300 DPI)

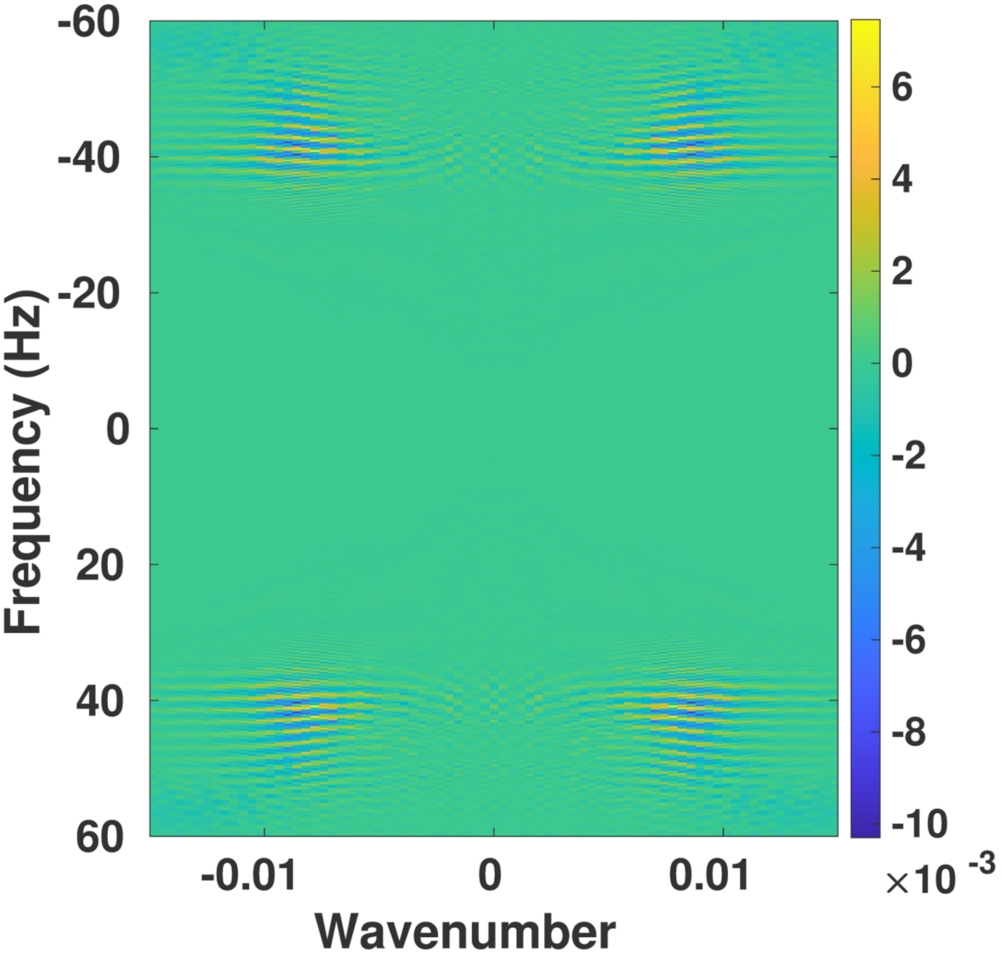

Figure 5(c). The difference between Figure 5(a) and Figure 5(b) normalized by the maximum value of Figure 5(a).

201x190mm (300 x 300 DPI)

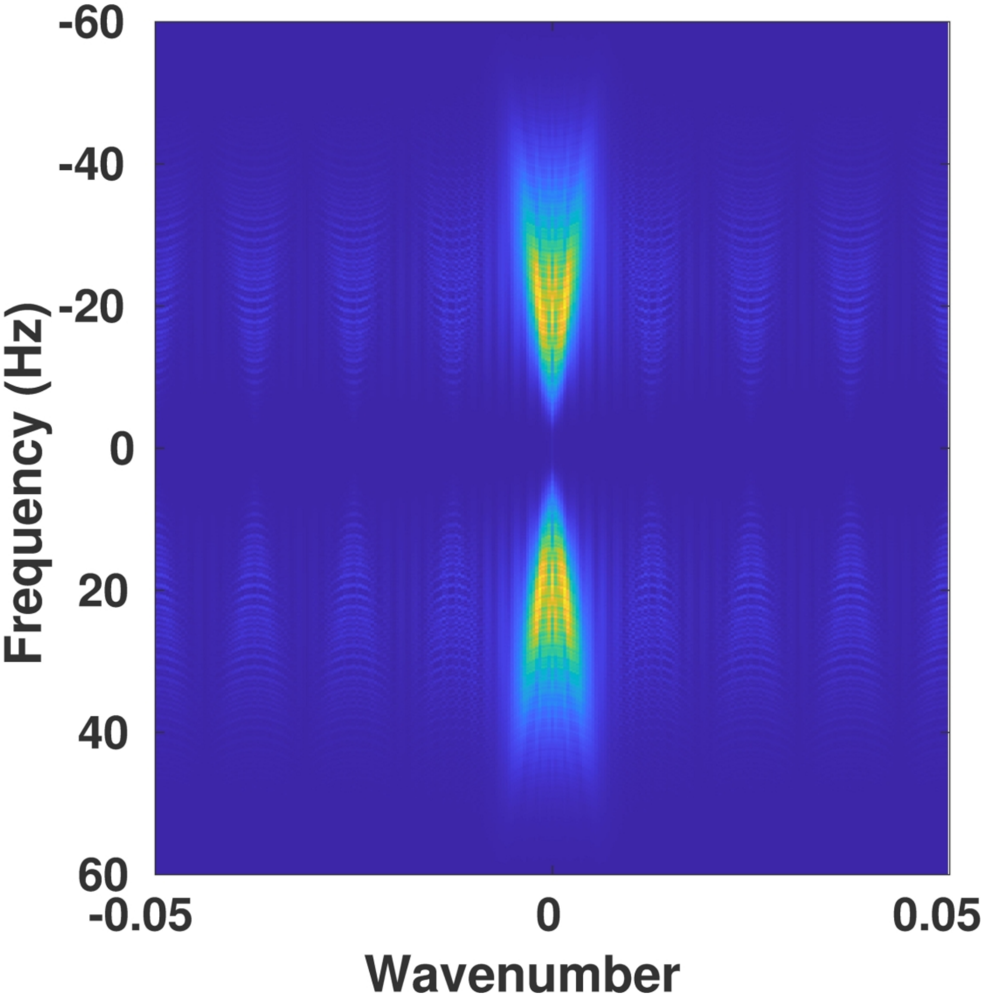

Figure 5(d). The focusing function in $f-k$ domain, corresponding to Figure 3c.

192x190mm (300 x 300 DPI)

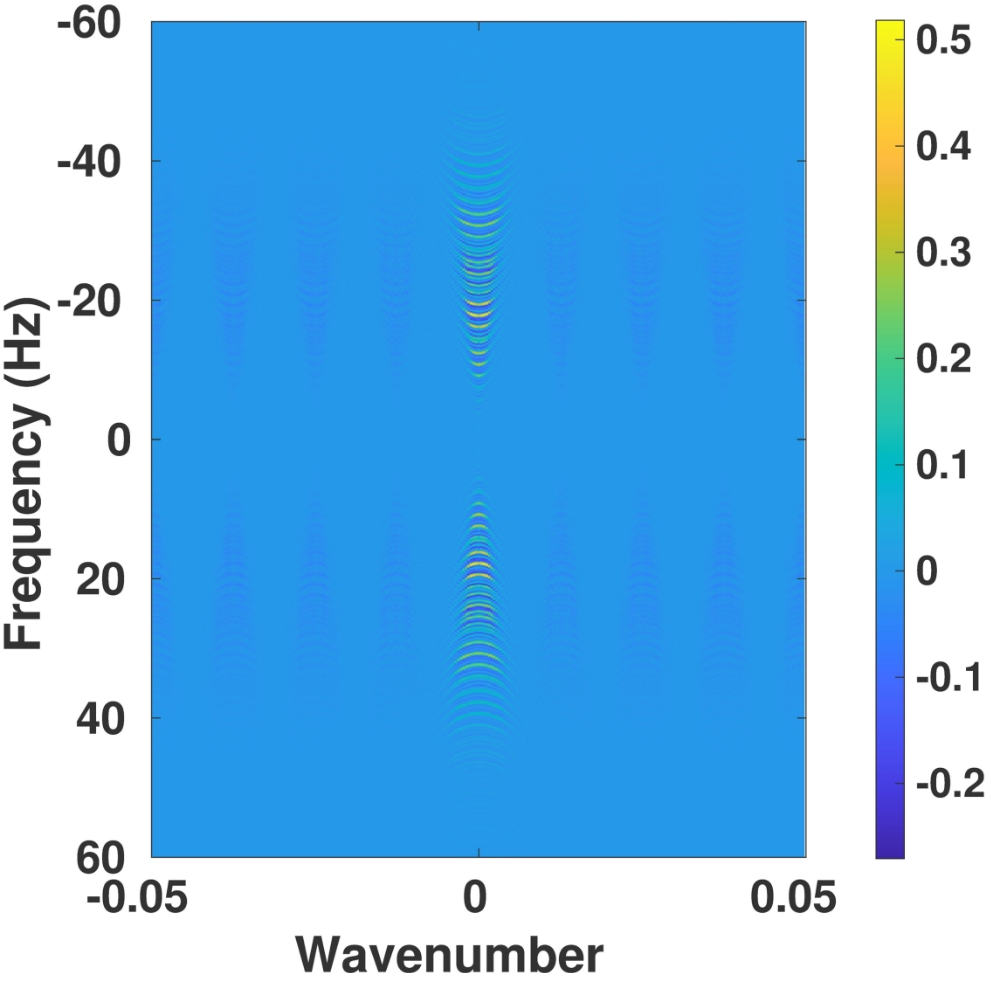

Figure 5(e). The difference between Figure 5(a) and Figure 5(d) normalized by the maximum value of Figure 5(a).

196x190mm (300 x 300 DPI)

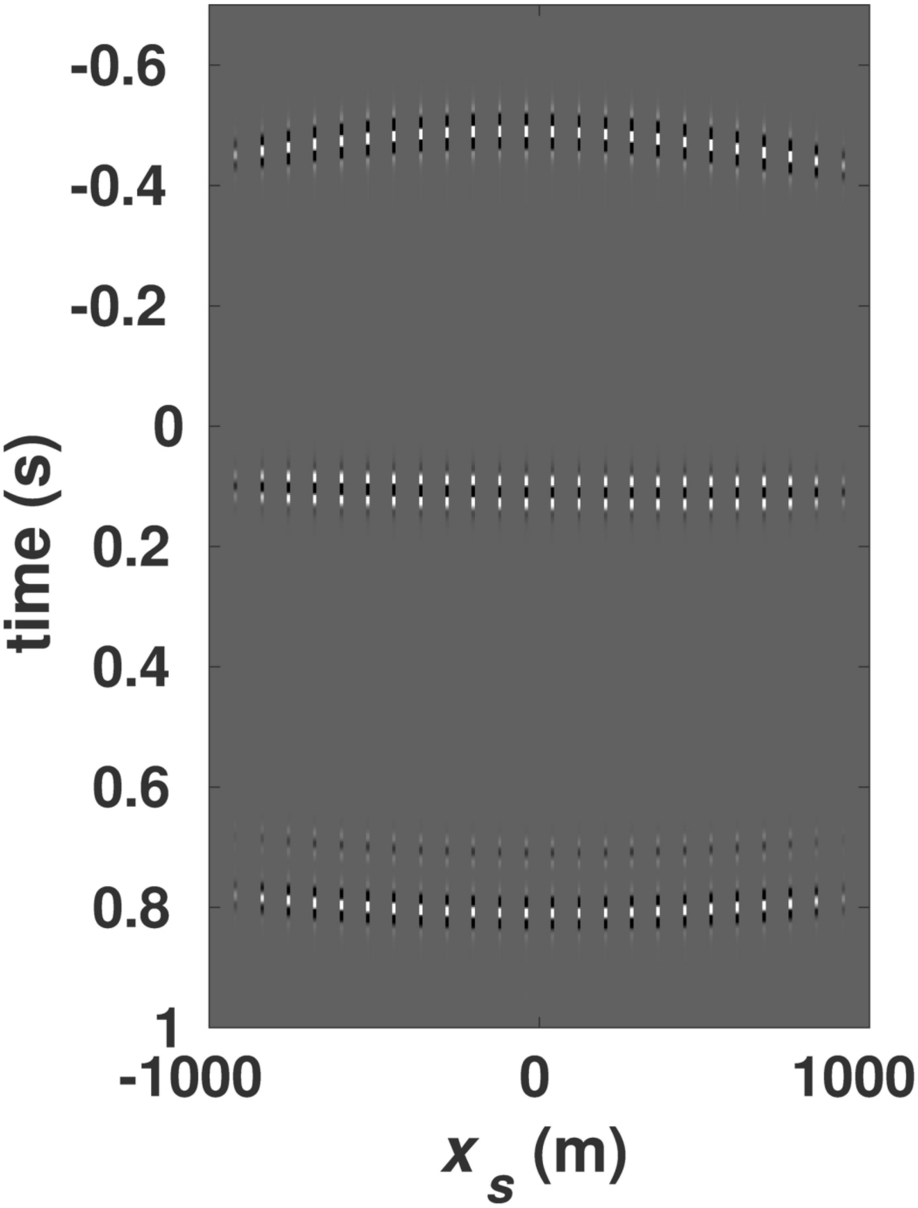

Figure 6(a). For the layered model in Figure 2a with the focal position \$(X_F=0\:\text{m}, Z_F=2670\:\text{m})\$ corresponding to Figure 3b, i.e. subsampling and integrating over the same dimension: the convolution gather from \$ \textbf{R} \bm{f}^{+}_{1d}\$ for the output near-offset receiver position \$X_r = -40\:\text{m}\$.

147x187mm (300 x 300 DPI)

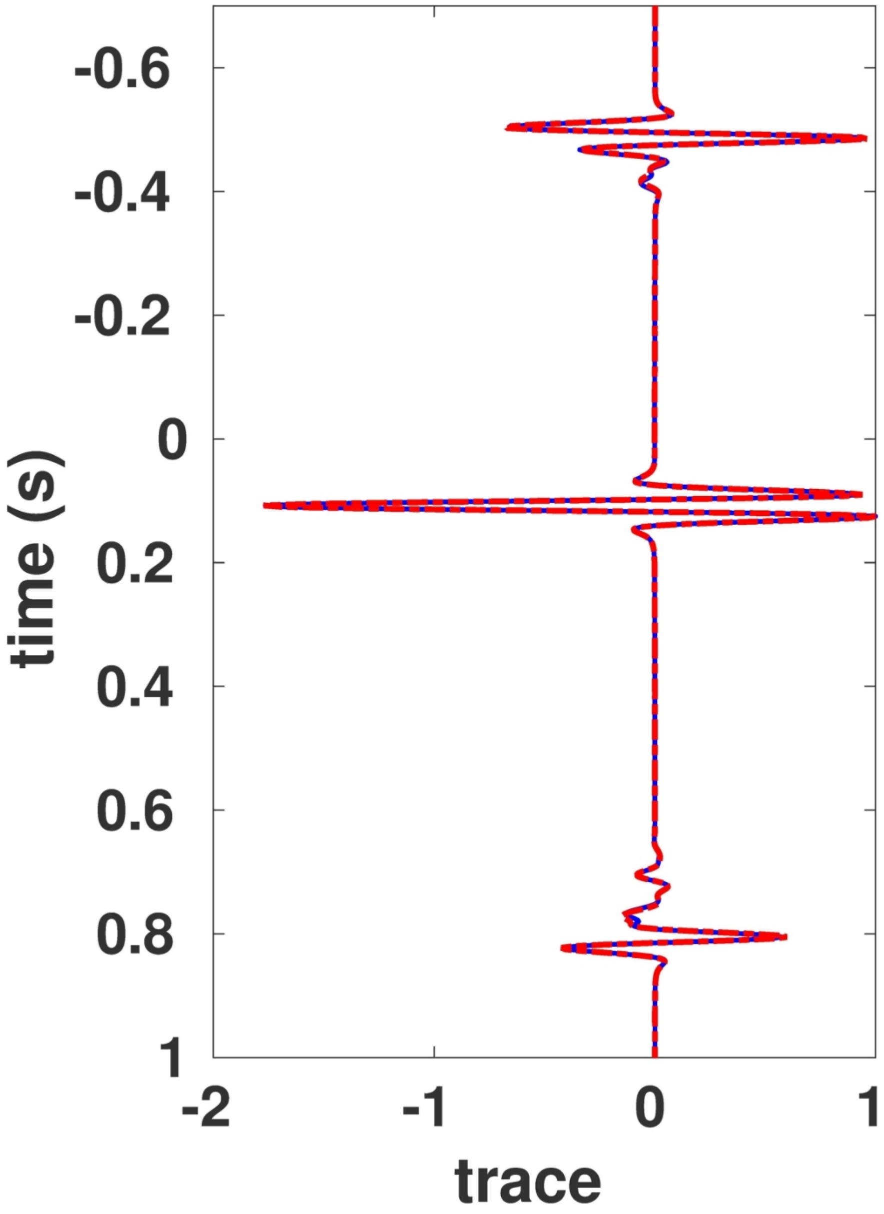

Figure 6(b) Integration of Figure 6(a), with scaling by the subsampled source interval. The blue and red lines represent the results calculated with and without subsampling, respectively.

138x187mm (300 x 300 DPI)

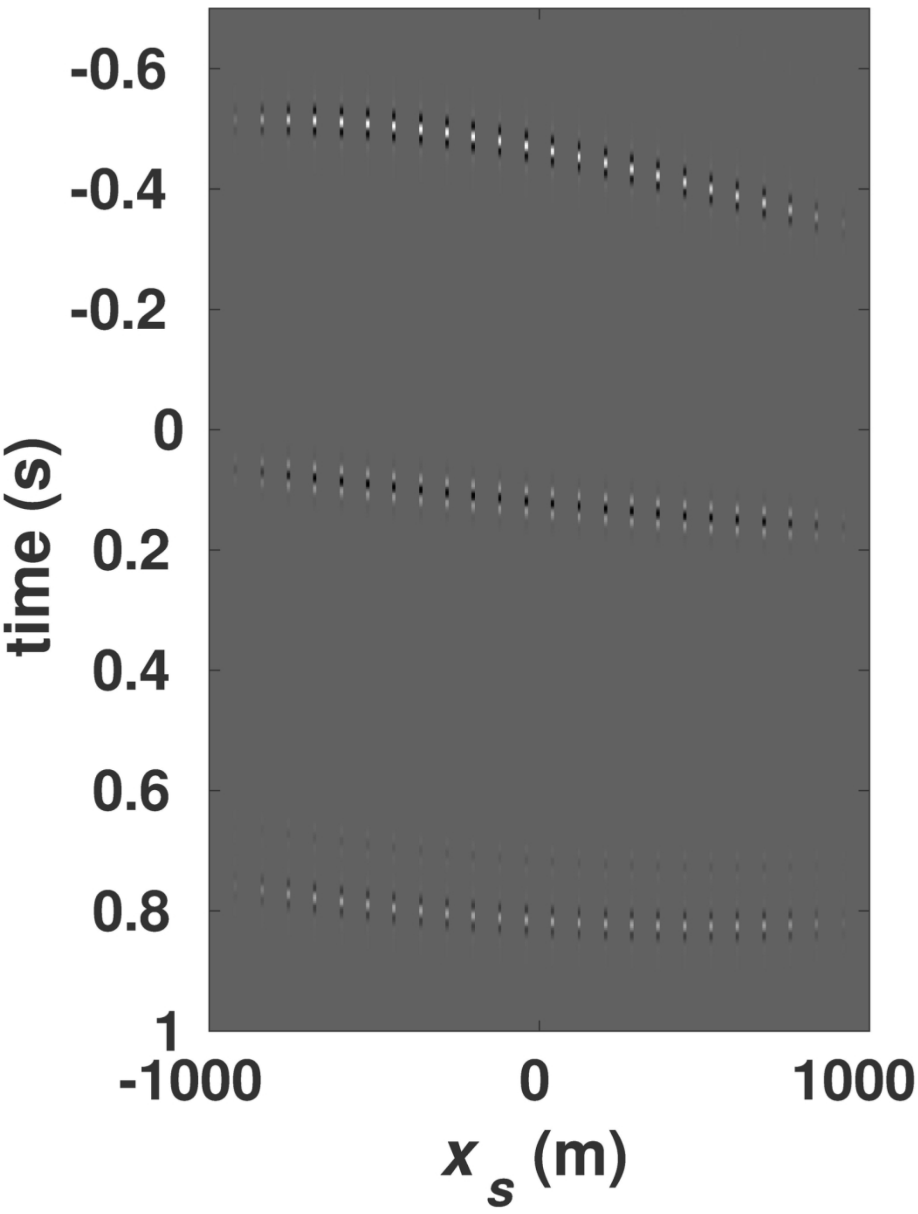

Figure 6(c) is counterpart to Figure 6(a), but for $X_r = -400\:\text{m}$ (mid-offset).

147x187mm (300 x 300 DPI)

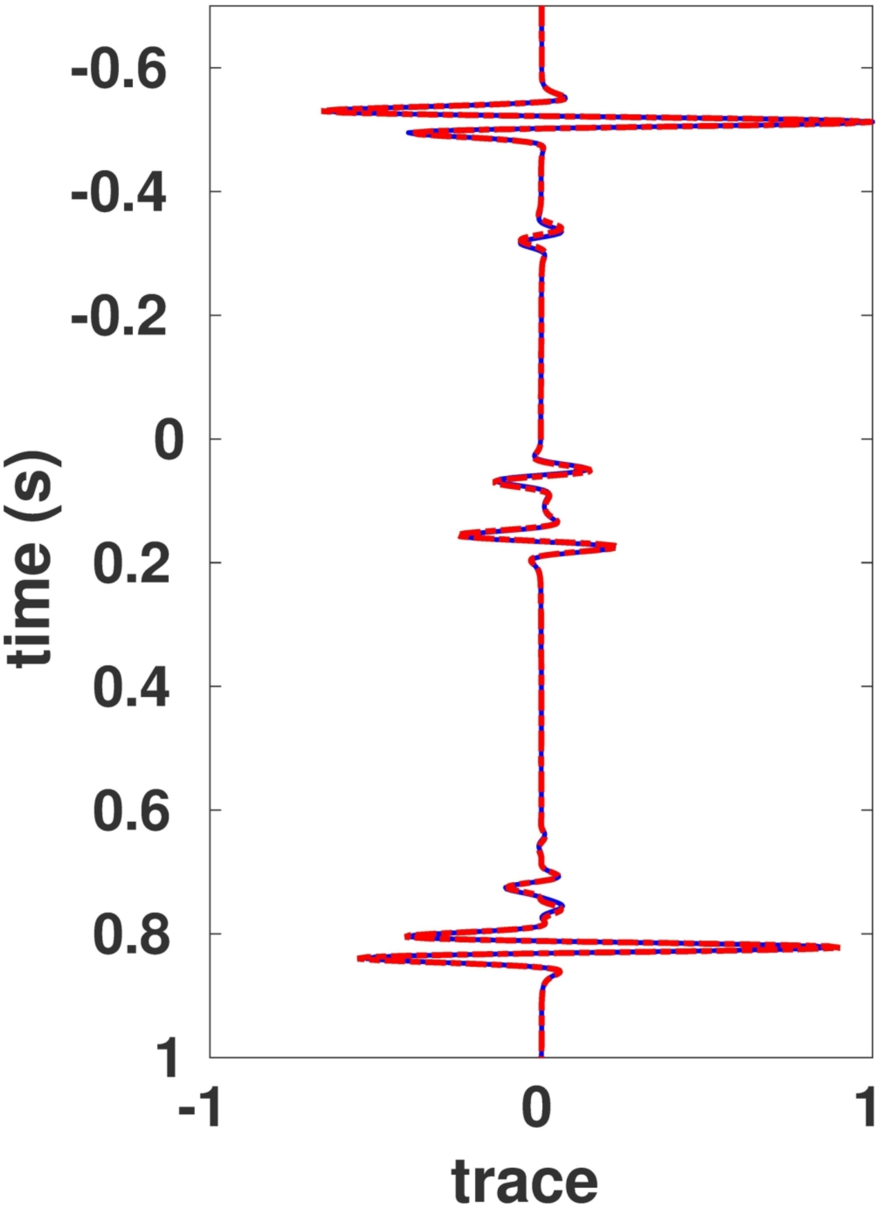

Figure 6(d) is counterpart to Figure 6(b), but for $X_r = -400\: ext{m}$ (mid-offset).

138x187mm (300 x 300 DPI)

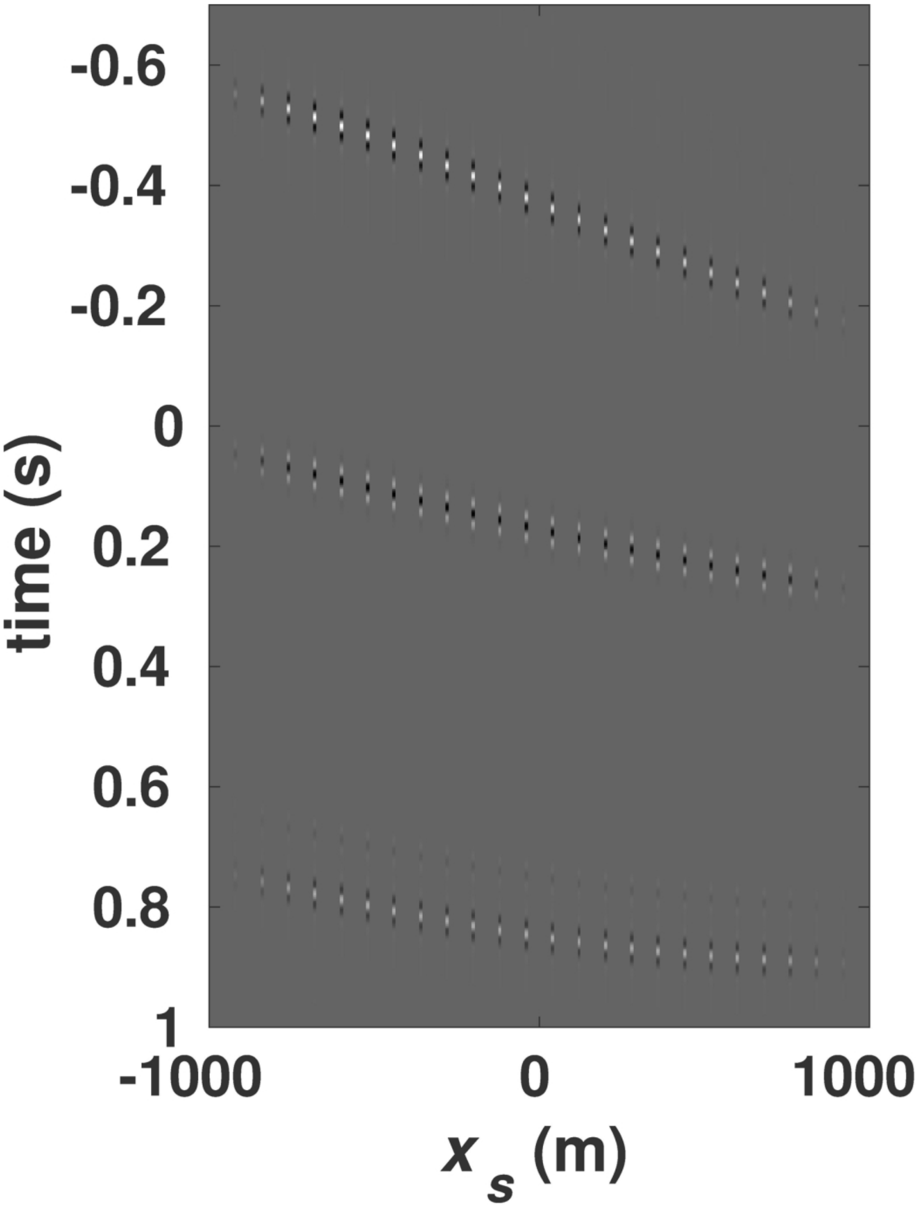

Figure 6(e) is counterpart to Figure 6(a), but for $X_r = -960\:\text{m}$ (far-offset).

147x187mm (300 x 300 DPI)

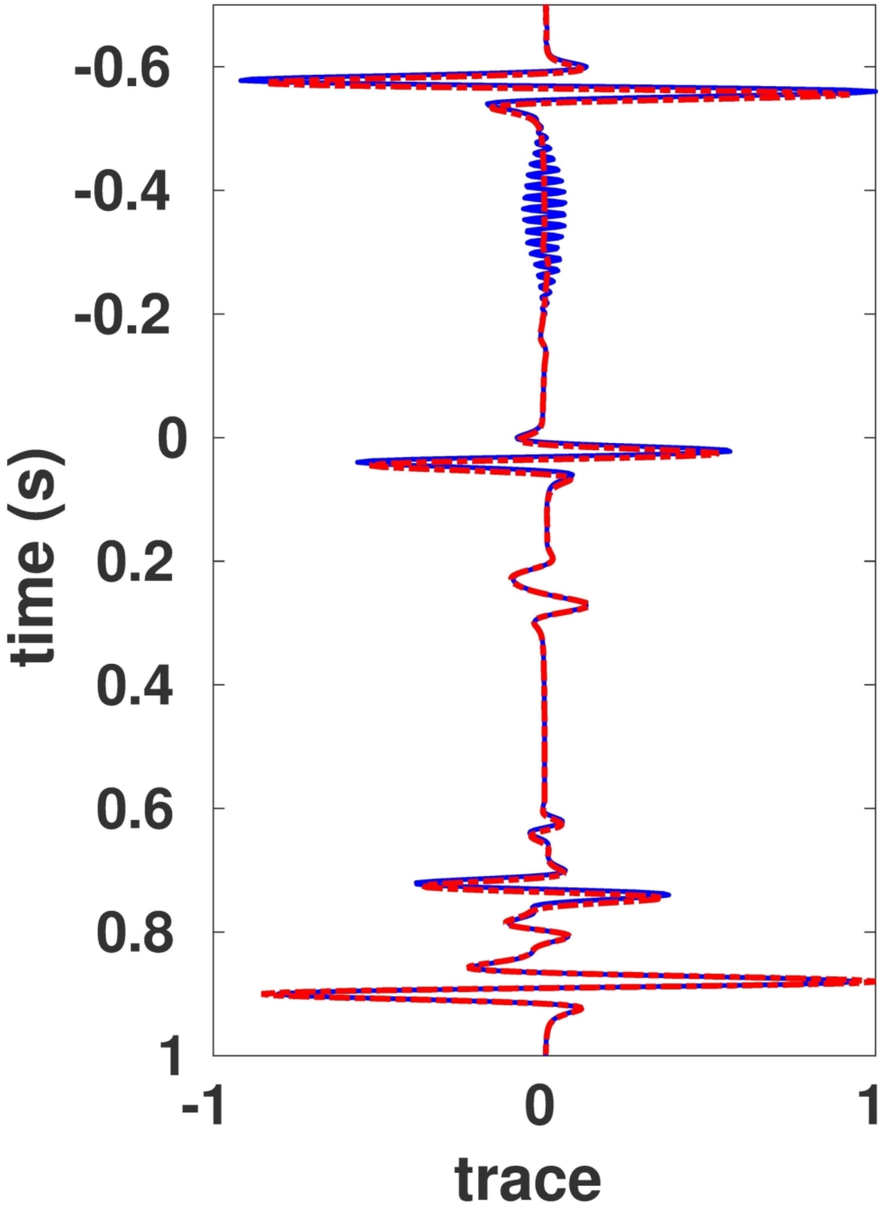

Figure 6(f) is counterpart to Figure 6(b), but for $X_r = -960\:\text{m}$ (far-offset).

138x187mm (300 x 300 DPI)

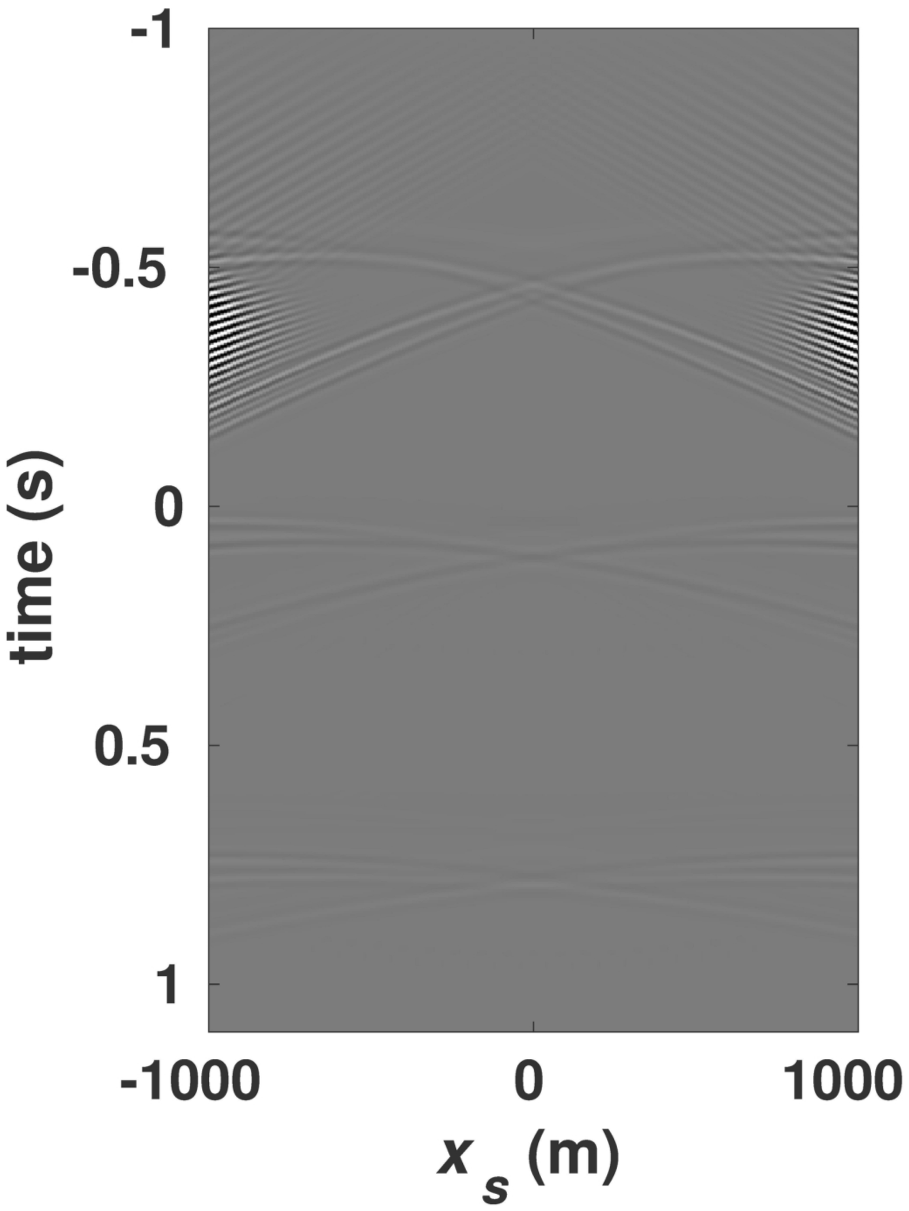

Figure 7(a). For the layered model in Figure 1a with focal point at $(X_F=0\: ext{m}, Z_F=2670\: ext{m})$, the error of focusing function caused by subsampling and integrating on the same dimension (corresponding to Figure 3b) in the first iteration.

147x190mm (300 x 300 DPI)

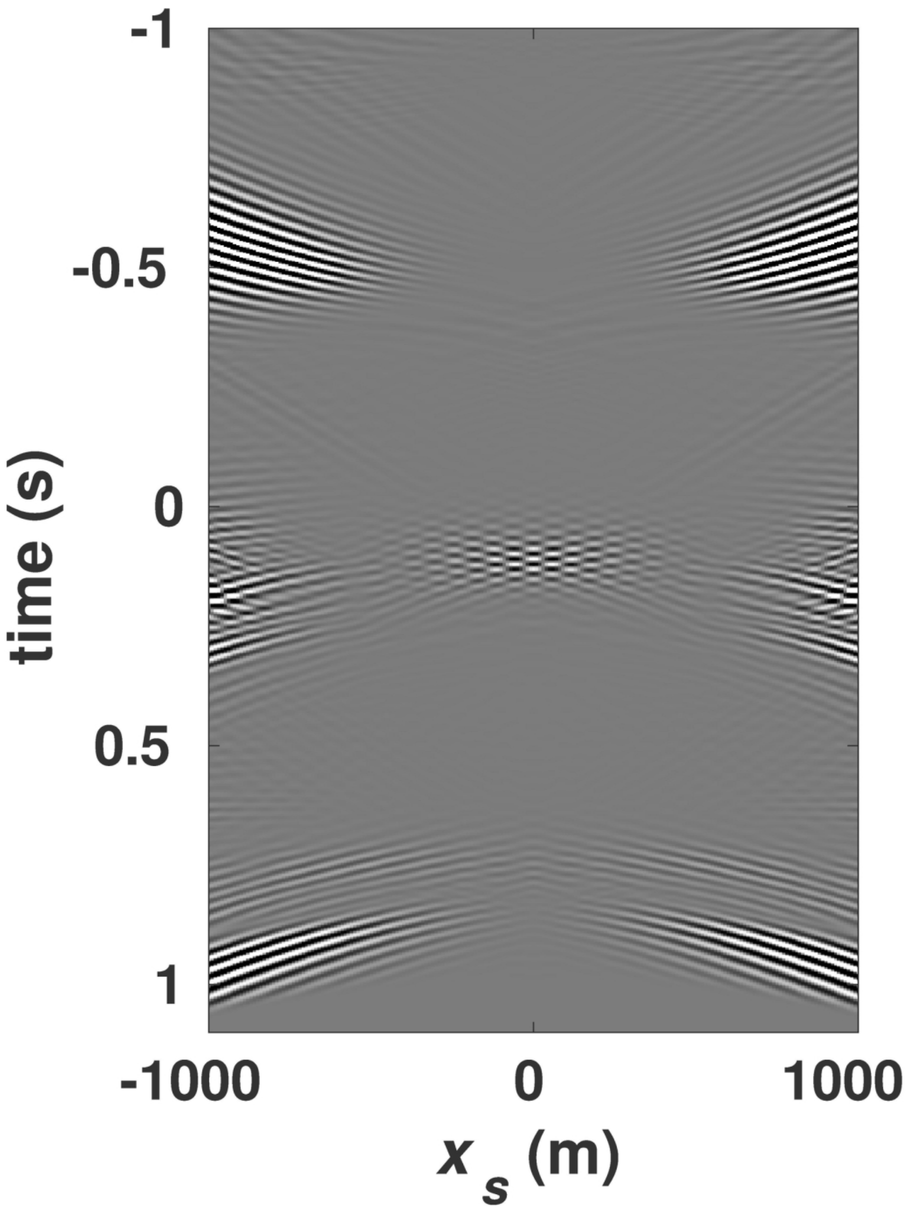

Figure 7(b). For the layered model in Figure 1a with focal point at $(X_F=0\: ext{m}, Z_F=2670\: ext{m})$, the error of focusing function caused by subsampling and integrating on the same dimension (corresponding to Figure 3b) in the second iteration.

147x190mm (300 x 300 DPI)

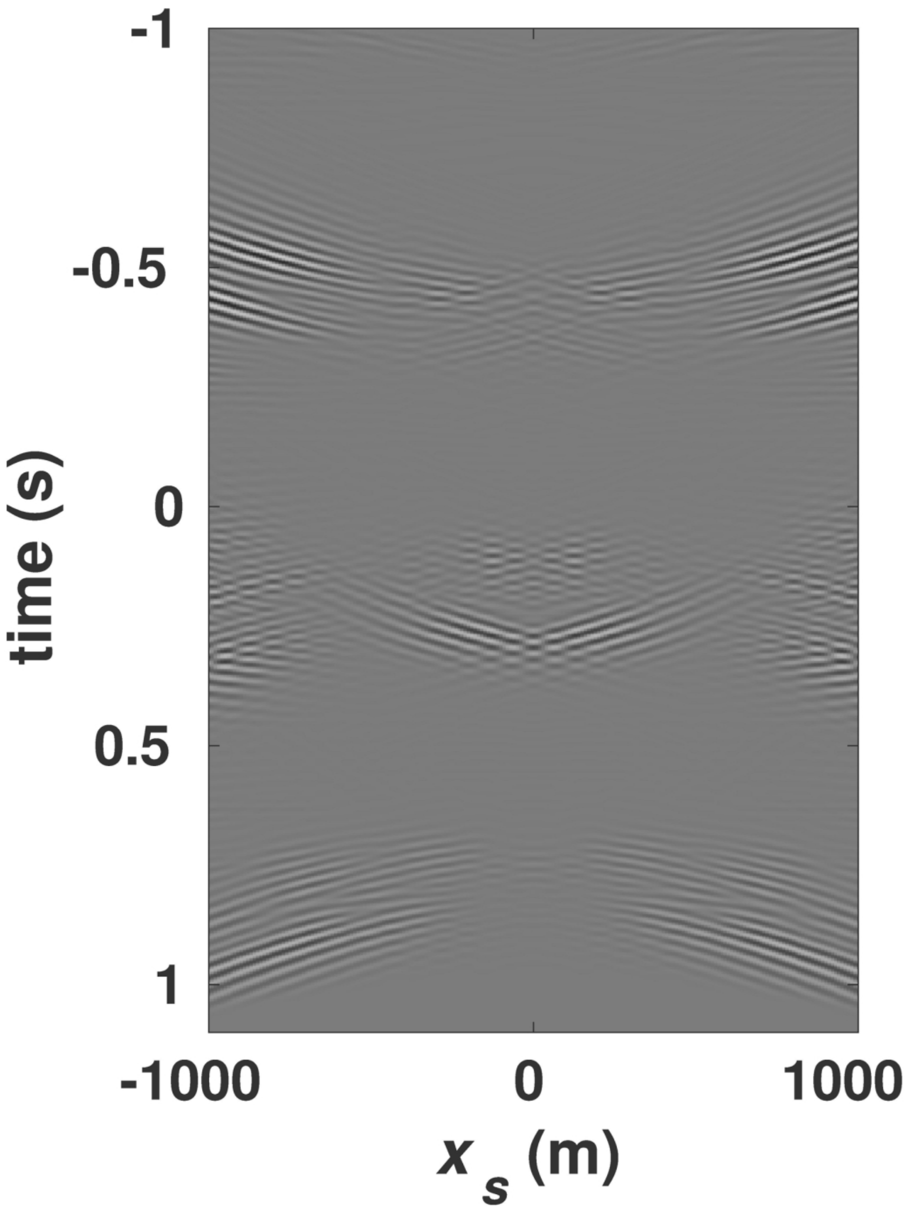

Figure 7(c). For the layered model in Figure 1a with focal point at $(X_F=0\:\text{m}, Z_F=2670\:\text{m})$, the error of focusing function caused by subsampling and integrating on the same dimension (corresponding to Figure 3b) in the third iteration.

147x190mm (300 x 300 DPI)

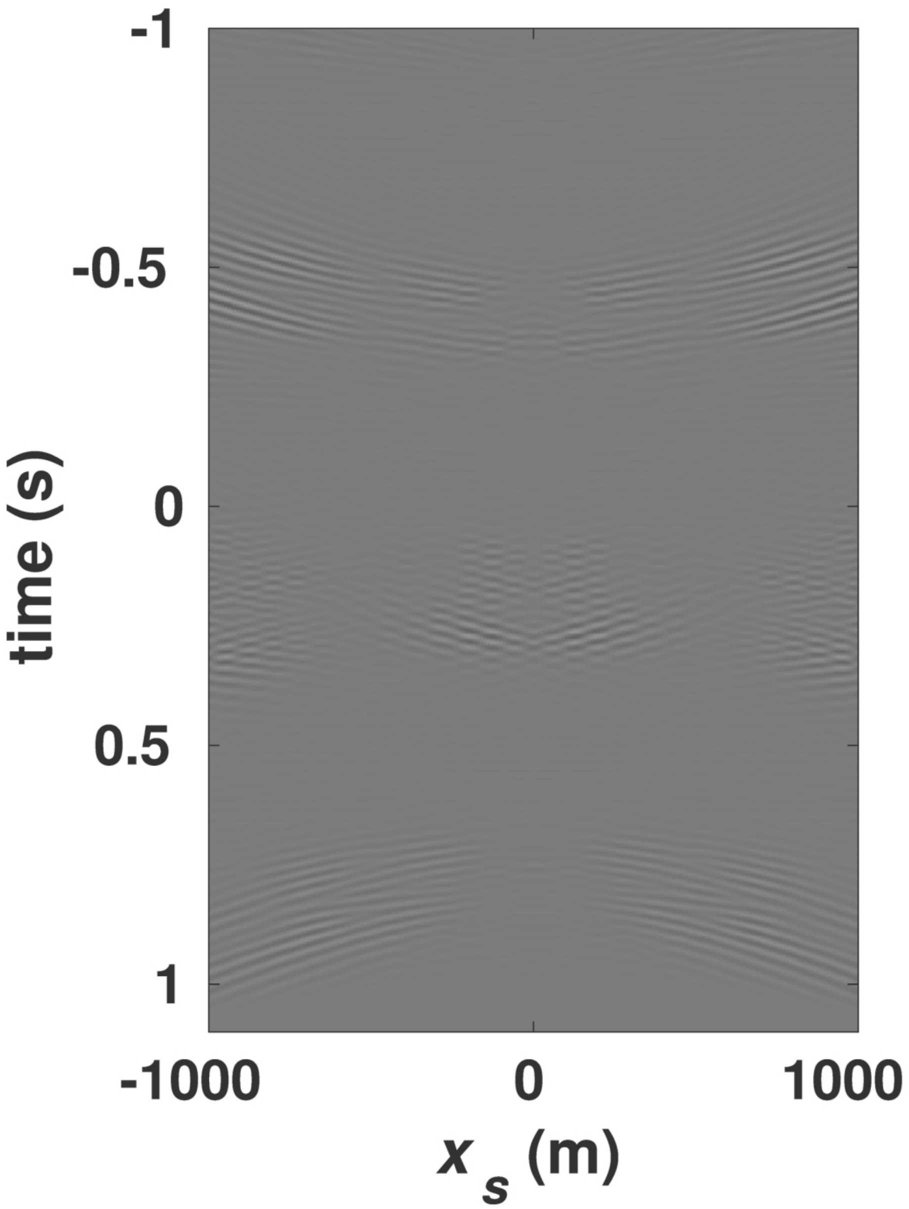

Figure 7(d). For the layered model in Figure 1a with focal point at $(X_F=0\:\text{m}, Z_F=2670\:\text{m})$, the error of focusing function caused by subsampling and integrating on the same dimension (corresponding to Figure 3b) in the fourth iteration.

147x190mm (300 x 300 DPI)

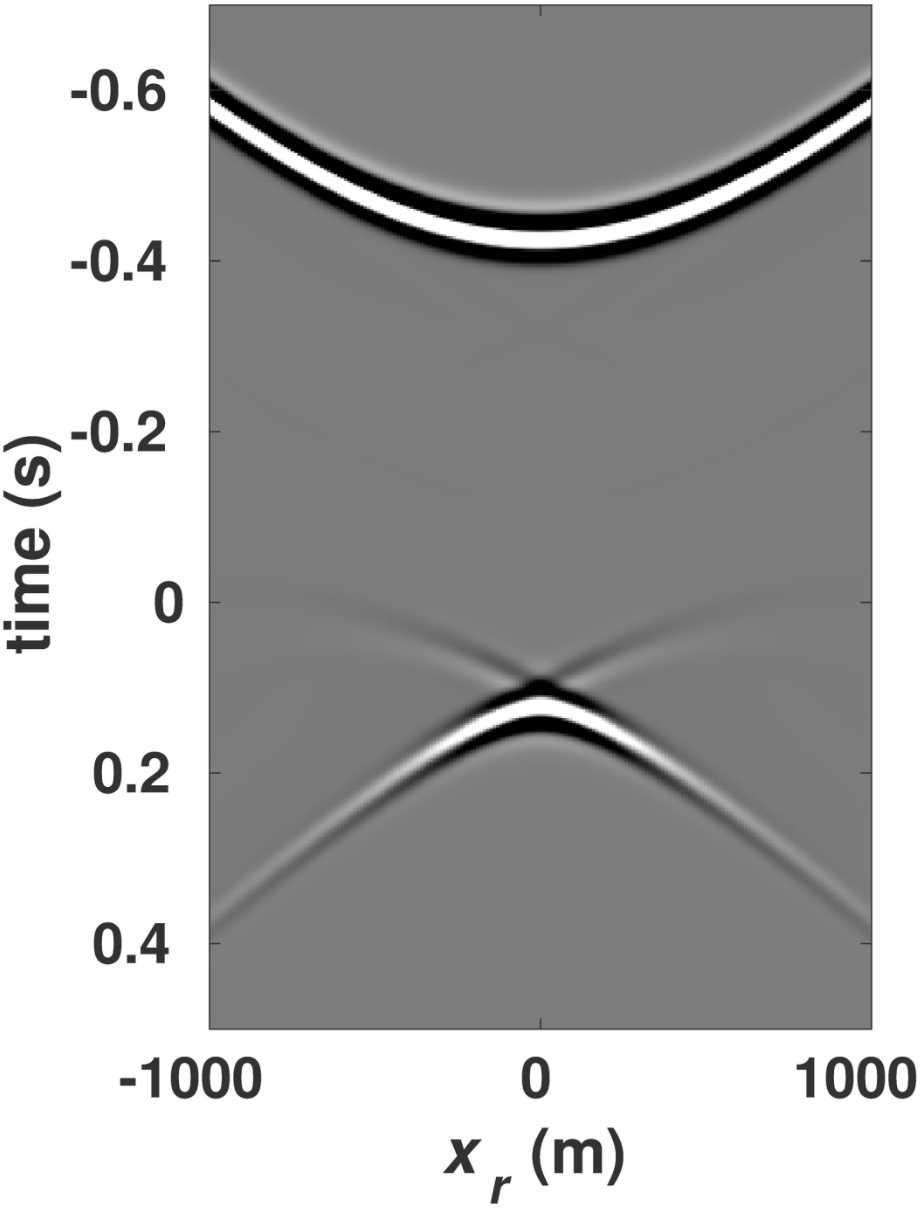

Figure 8(a). For the layered model in Figure 2a with a shallower focal point at $(X_F=0\:\text{m}, Z_F=1125\:\text{m})$, the reference focusing function without subsampling.

147x187mm (300 x 300 DPI)

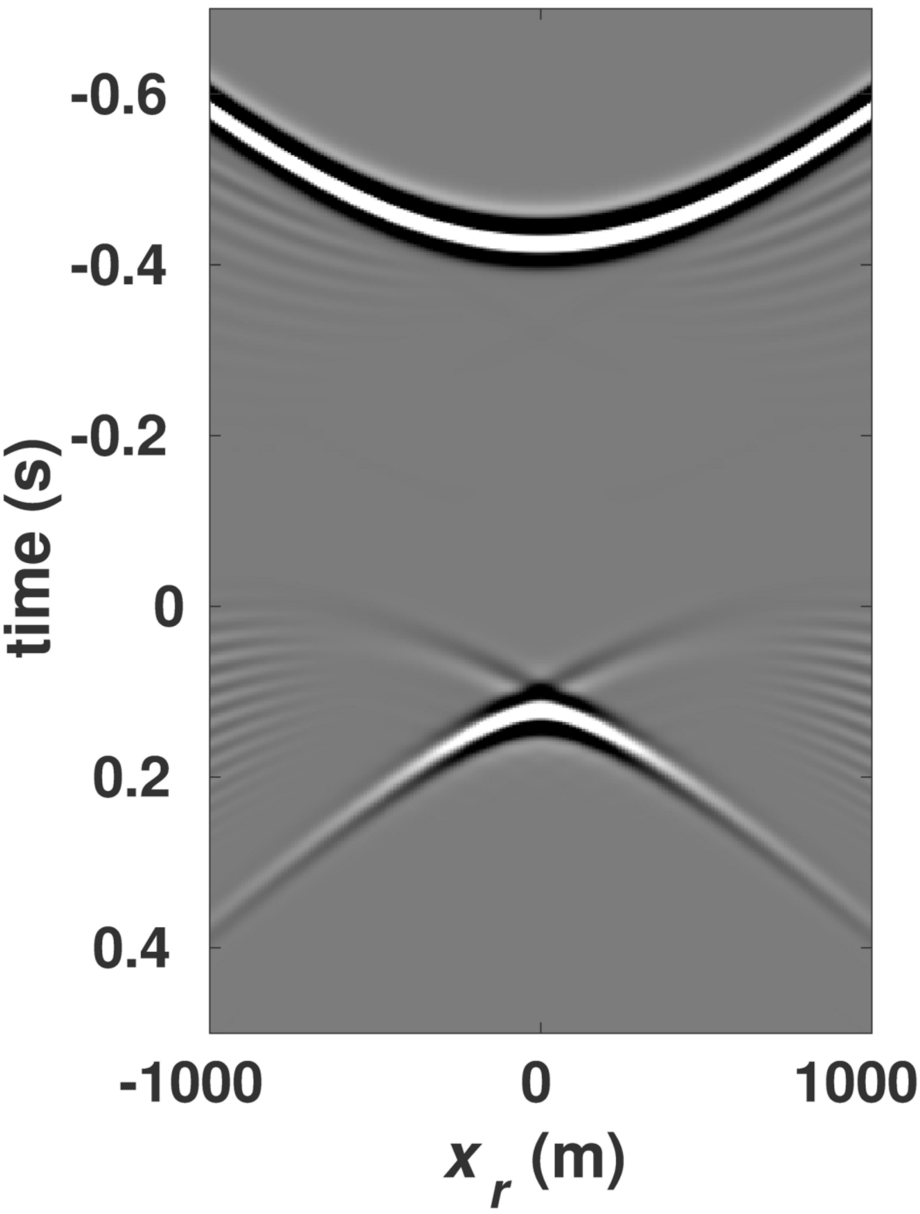

Figure 8(b). The same as Figure 8a, but calculated by subsampling and integrating over sources, using the sampling mask shown in Figure 2b.

147x187mm (300 x 300 DPI)

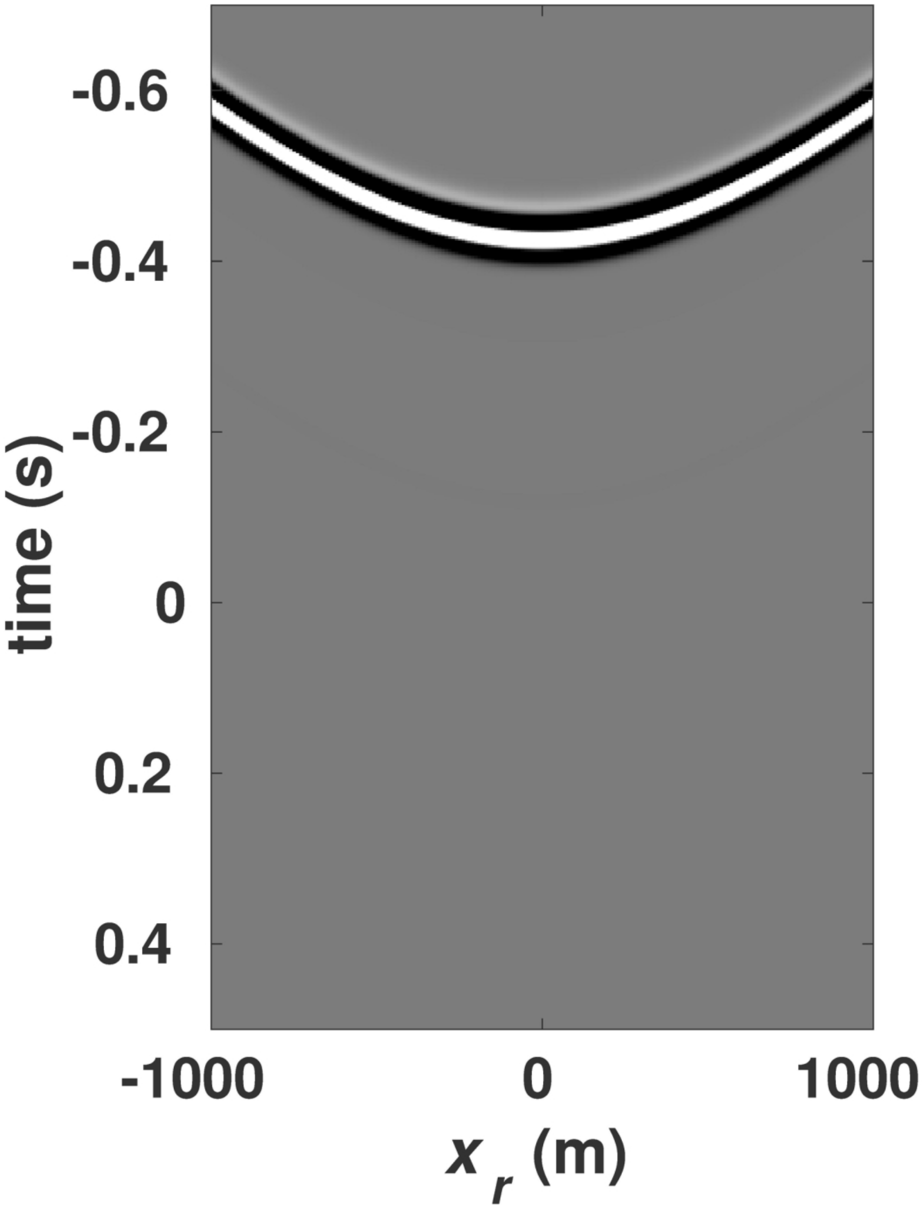

Figure 8(c) the initial focusing functions used for the focusing depths at $Z_F=1125\:\text{m}$,at fixed aperture.

147x187mm (300 x 300 DPI)

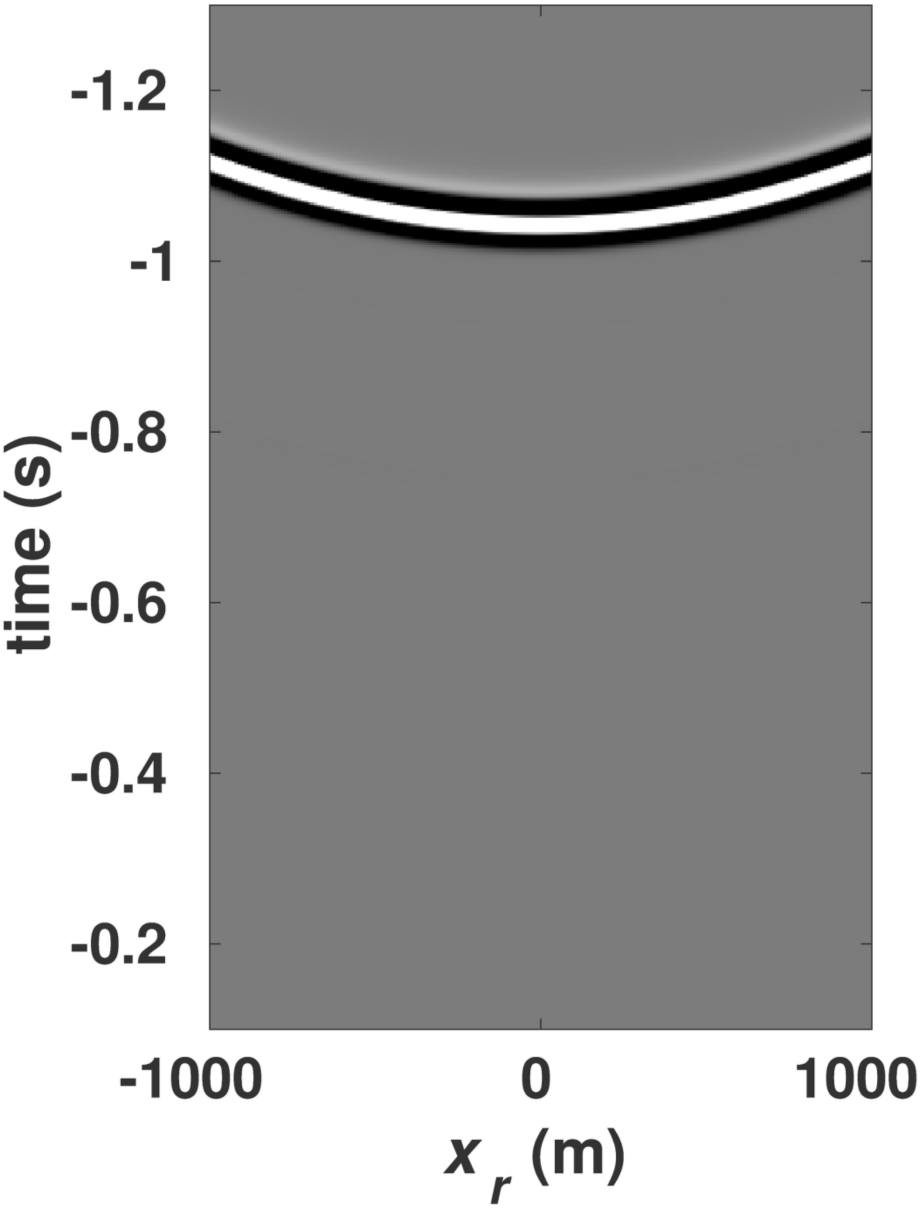

Figure 8(d) the initial focusing functions used for the focusing depths at $Z_F=2670\:\text{m}$,at fixed aperture.

147x187mm (300 x 300 DPI)

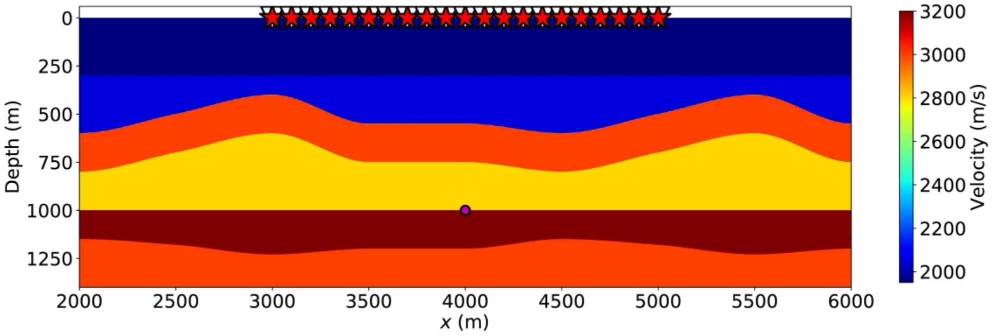

Figure 9(a) The velocity profile of the 2D model used in the source-receiver transpose study for the Marchenko focusing and primary estimation. The magenta dot denotes the location of focal point ($x=4000\: ext{m}$, $z=1000\: ext{m}$). The red stars and white triangles indicate the source and receiver locations.

382x131mm (300 x 300 DPI)

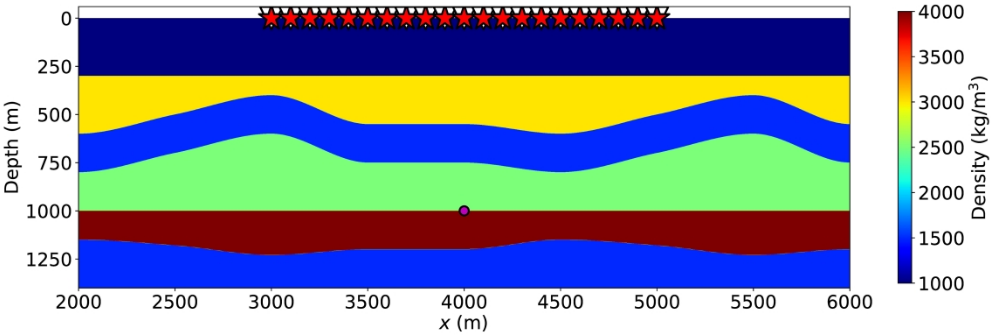

Figure 9(b) The density profile of the 2D model used in the source-receiver transpose study for the Marchenko focusing and primary estimation.

383x131mm (300 x 300 DPI)

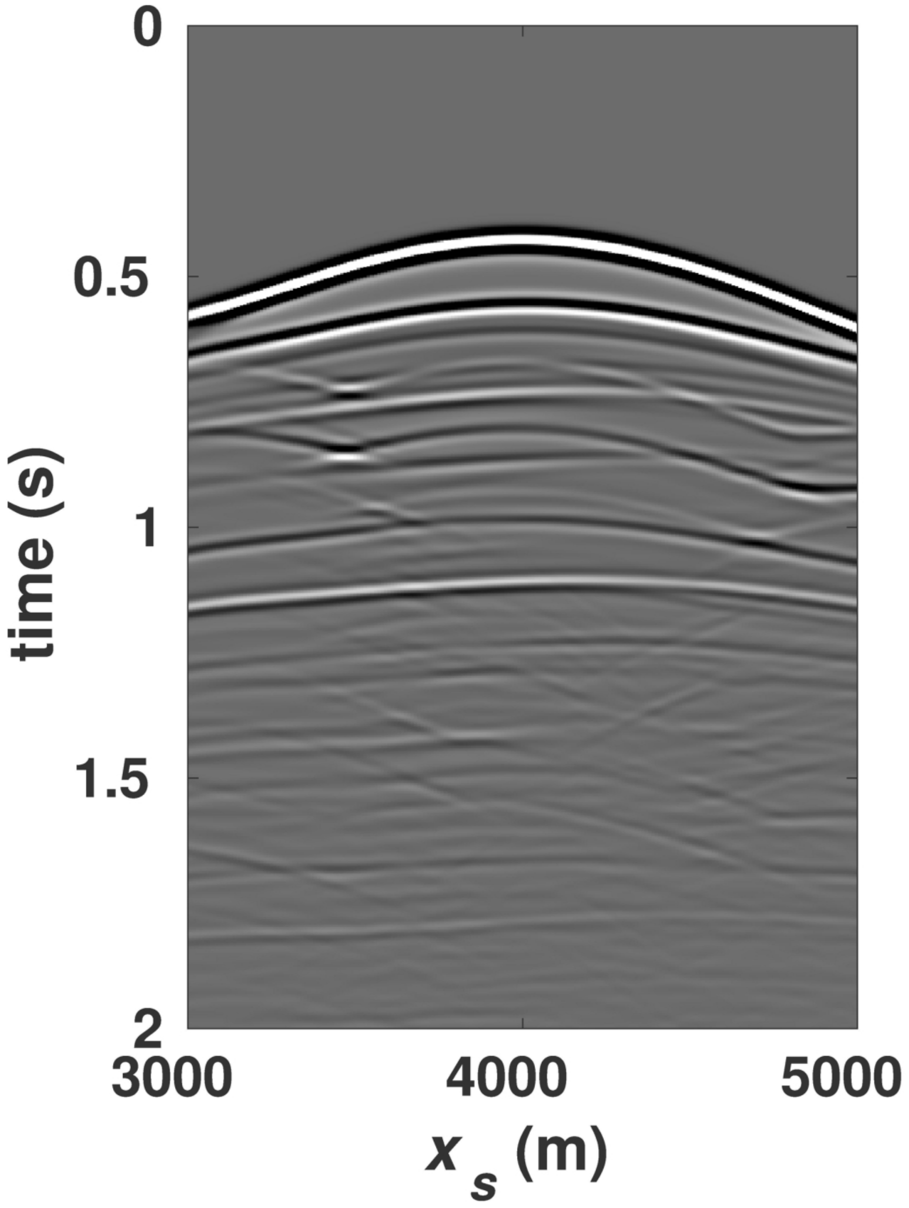

Figure 10(a). For the 2D model shown in Figure 9, the Green's function from forward modeling.

147x191mm (300 x 300 DPI)

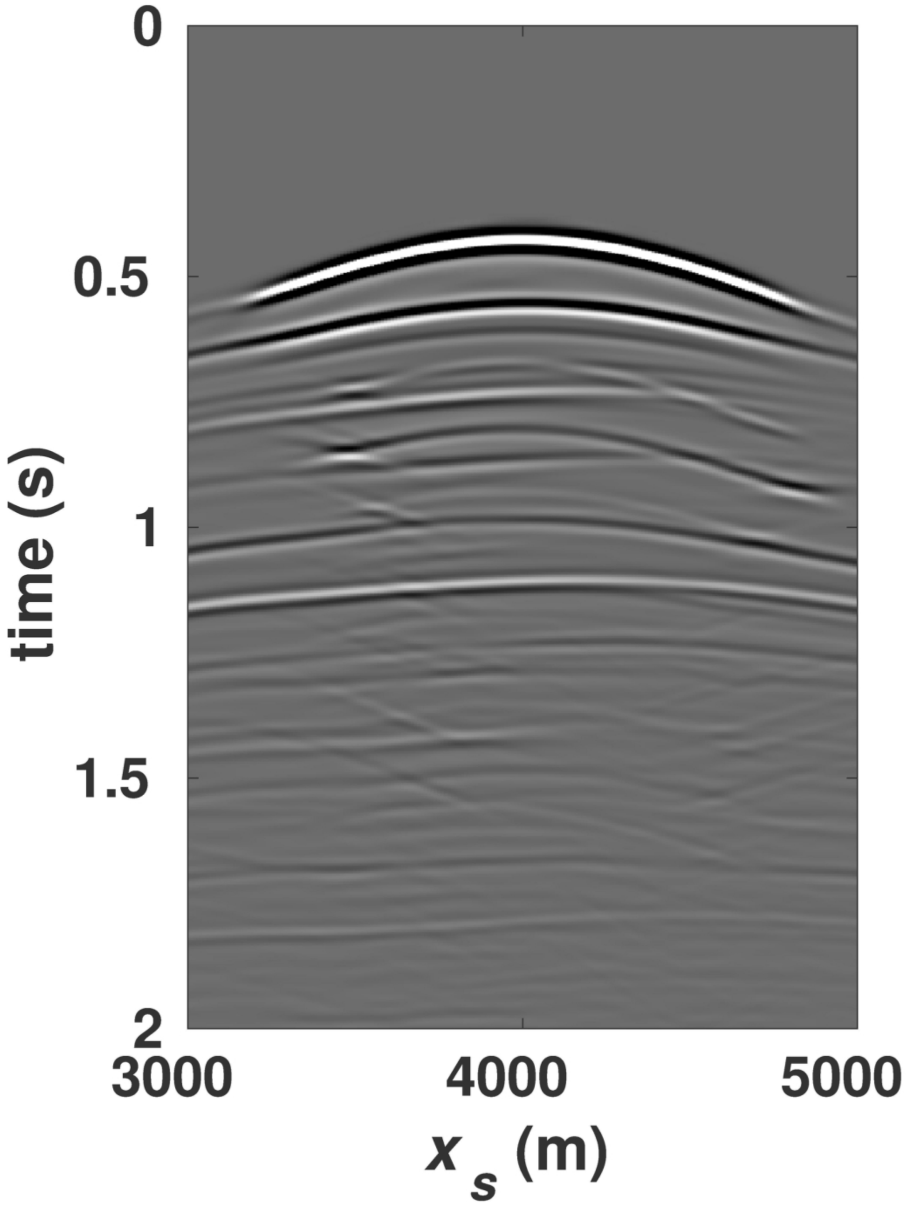

Figure 10(b). The same as Figue 10(a), but obtained from Marchenko redatuming by integrating on the dipole dimension.

147x191mm (300 x 300 DPI)

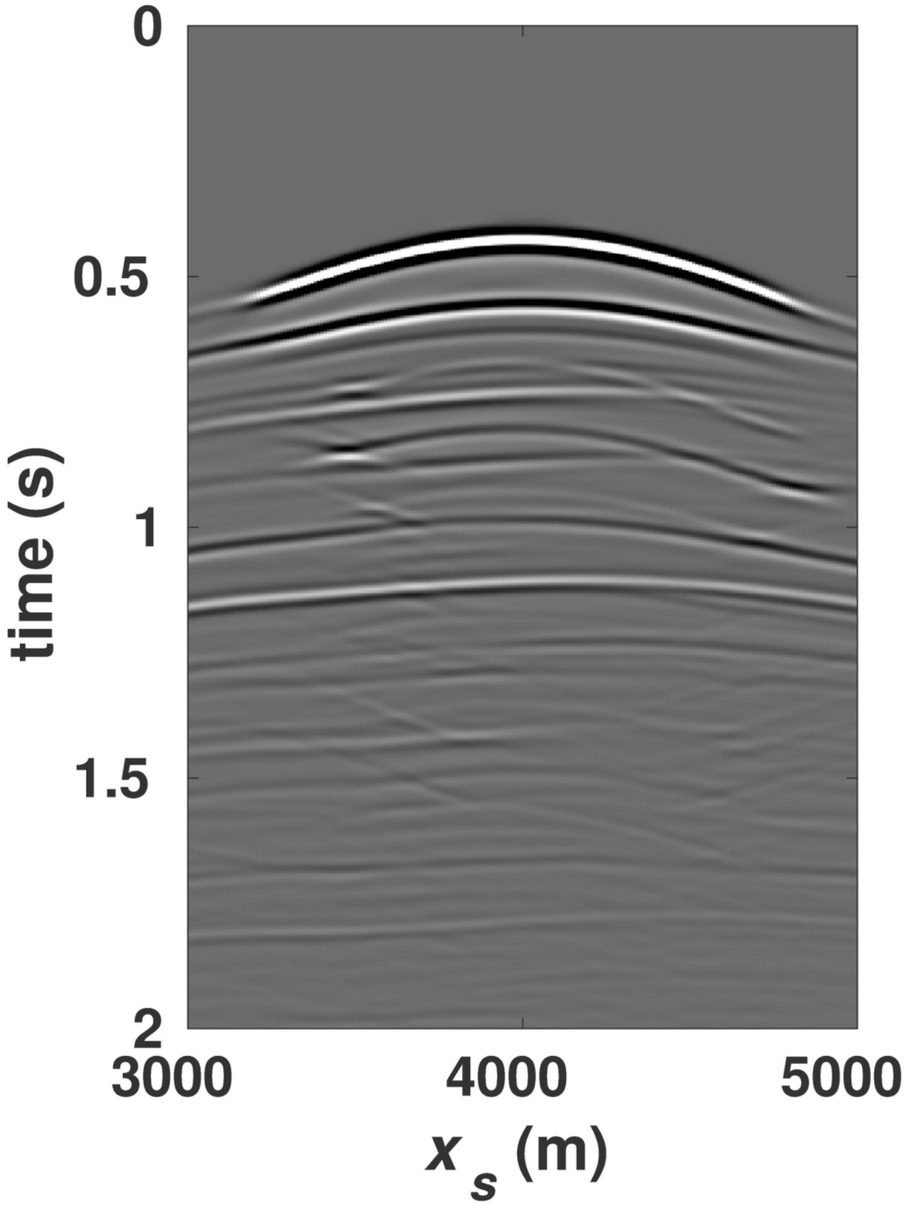

Figure 10(c). The same as Figue 10(a), but obtained from Marchenko redatuming by integrating on the monopole dimension.

147x191mm (300 x 300 DPI)

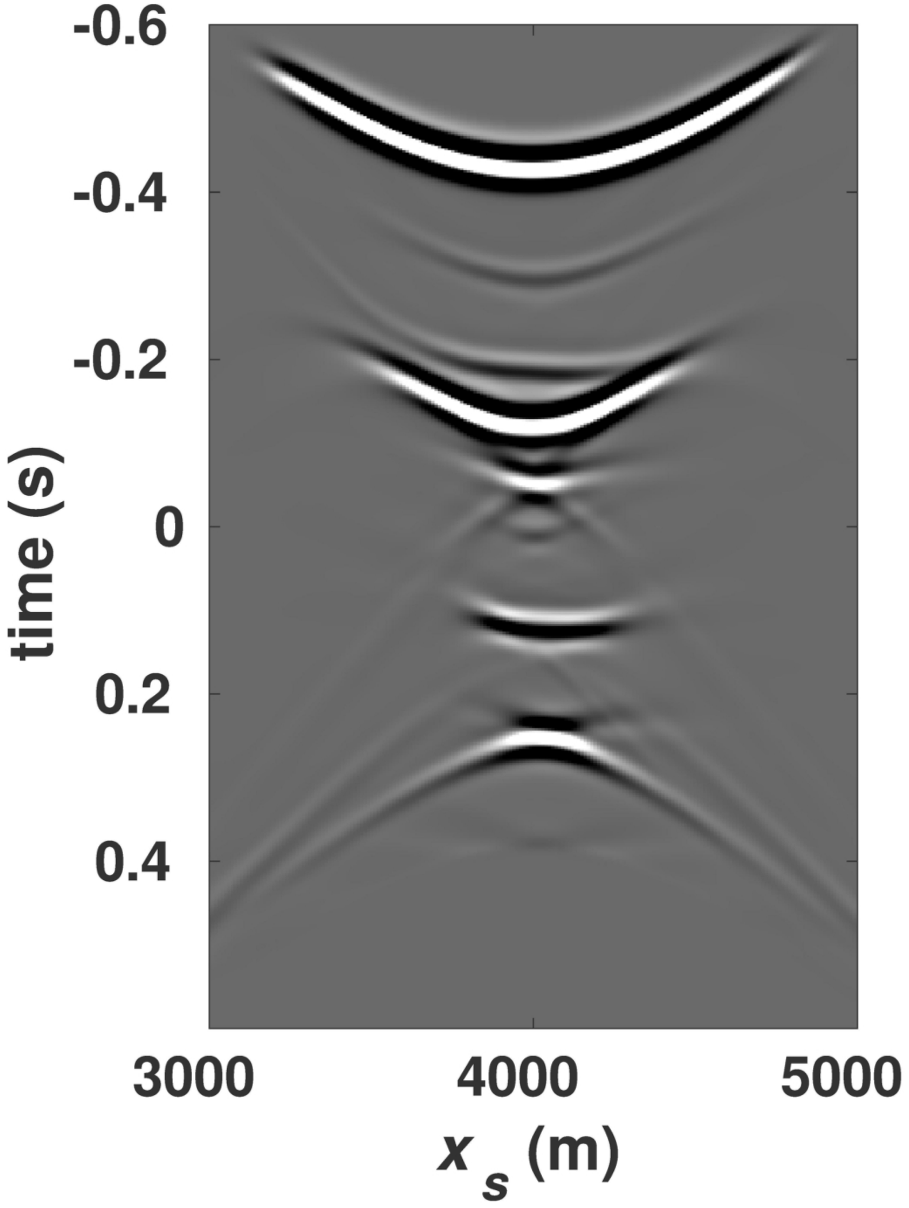

Figure 11(a): Focusing functions calculated by integrating on the dipole dimension.

147x191mm (300 x 300 DPI)

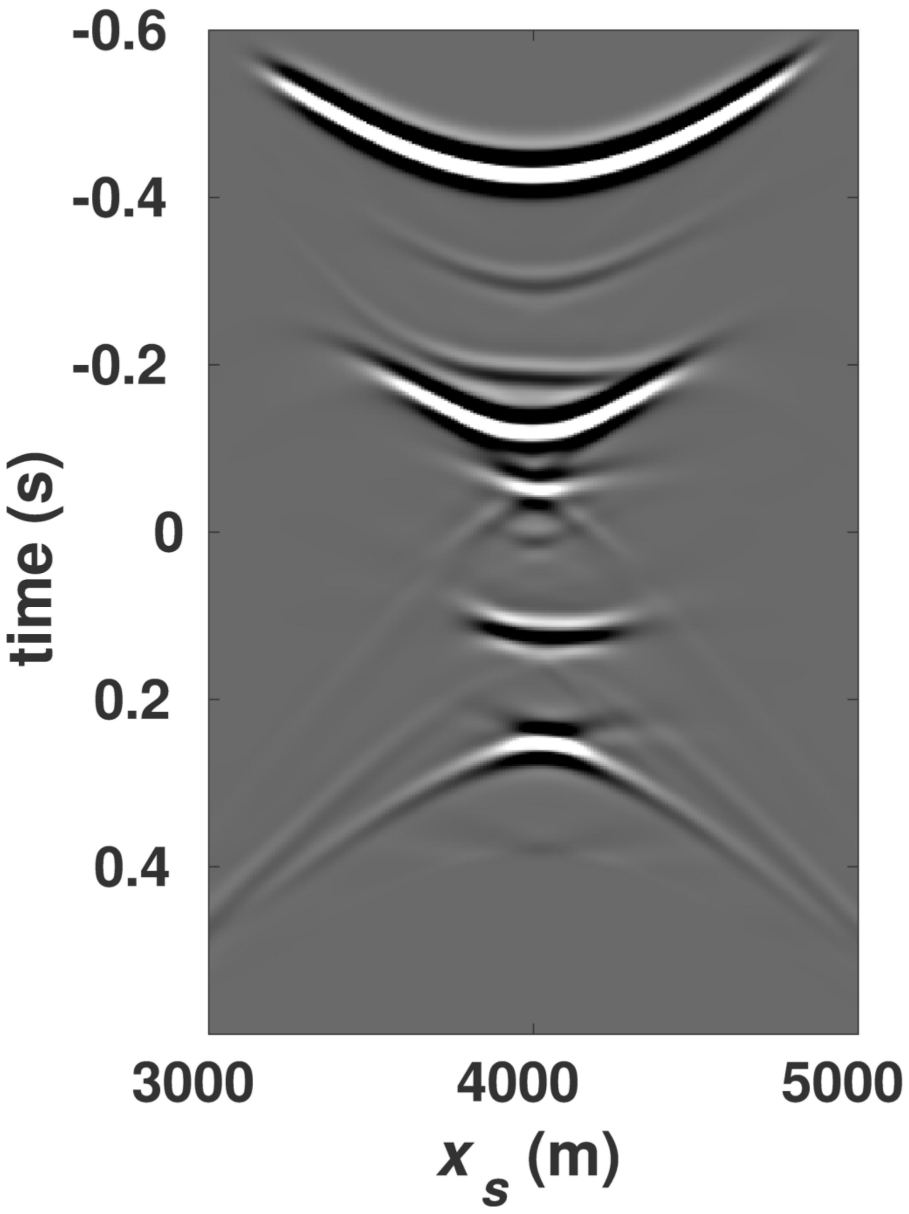

Figure 11(b): Focusing functions calculated by integrating on the monopole dimension.

147x190mm (300 x 300 DPI)

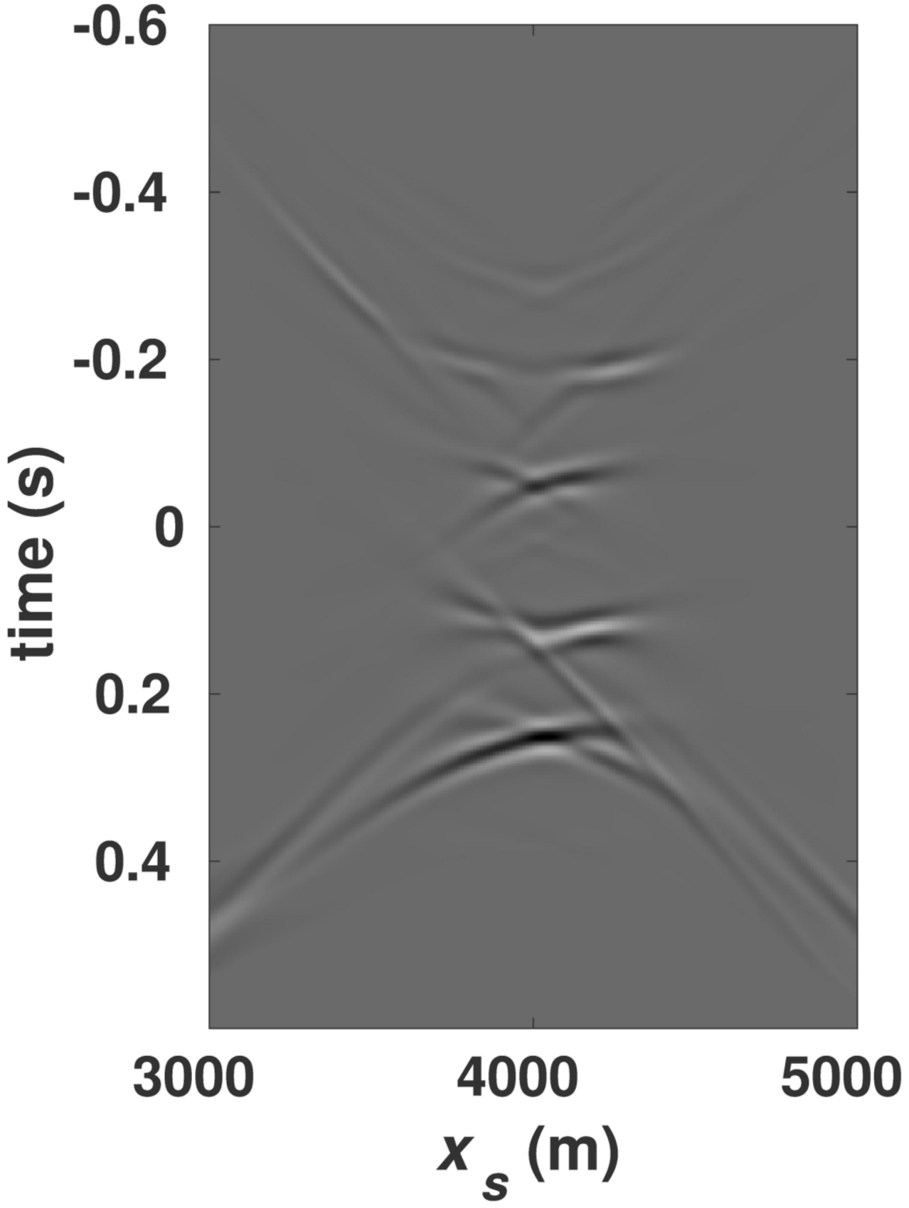

Figure 11(c) the difference between Figure 11(a) and Figure 11(b), of which the amplitude is multiplied by a gain factor of 10.

147x191mm (300 x 300 DPI)

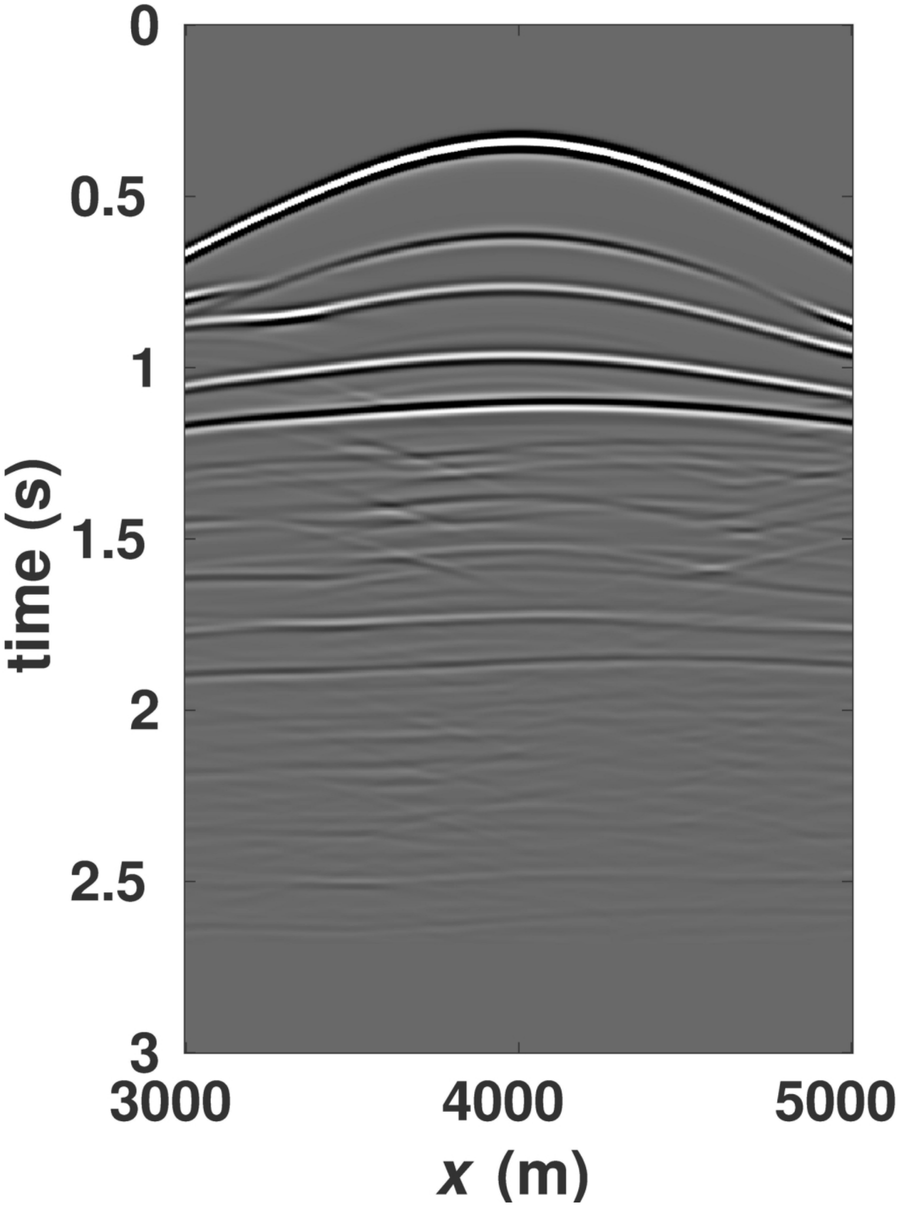

Figure 12(a). Results of primary estimation for the 2D model shown in Figure 9. The reference reflection data with source at $x=4000\: ext{m}$.

147x191mm (300 x 300 DPI)

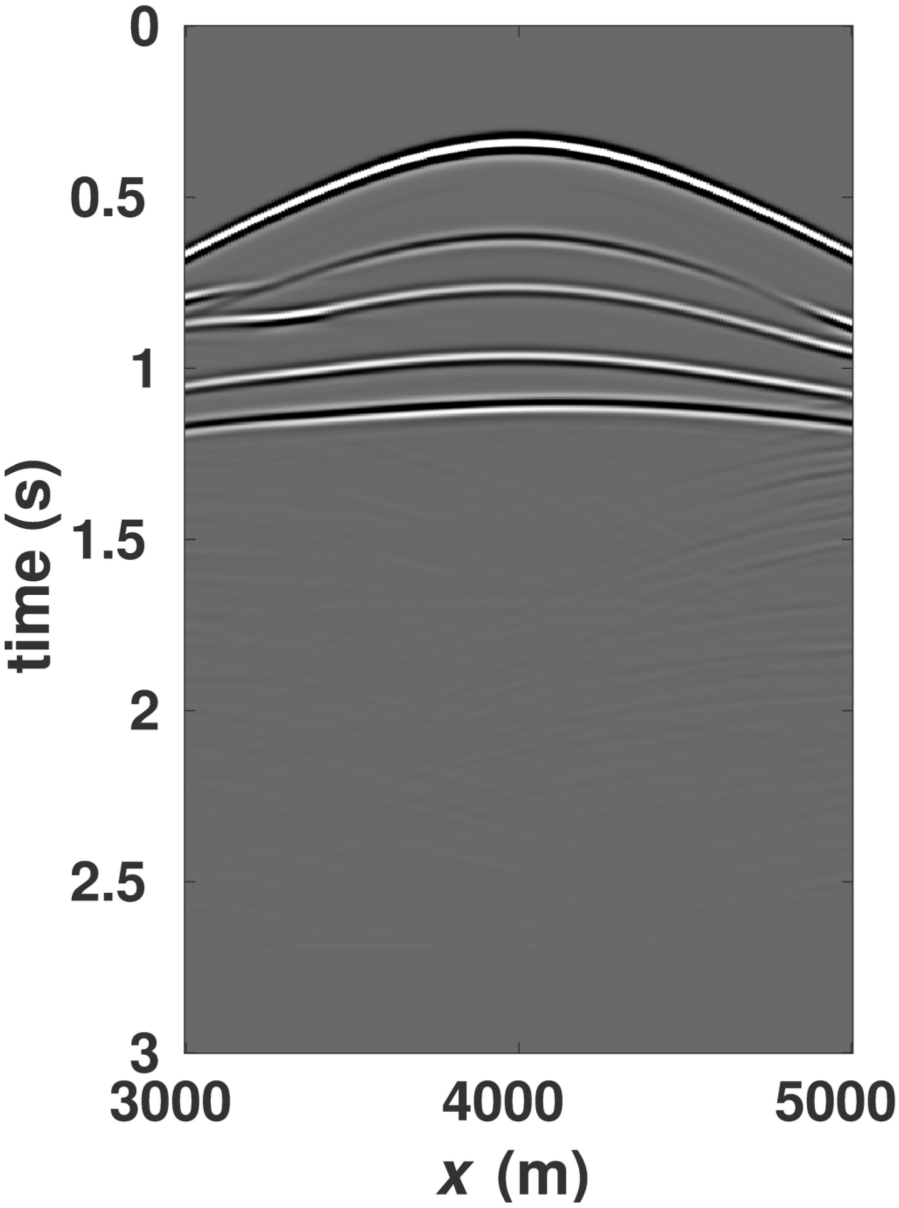

Figure 12(b). Results of primary estimation for the 2D model shown in Figure 9. The primary estimation from integrating on the dipole dimension.

147x191mm (300 x 300 DPI)

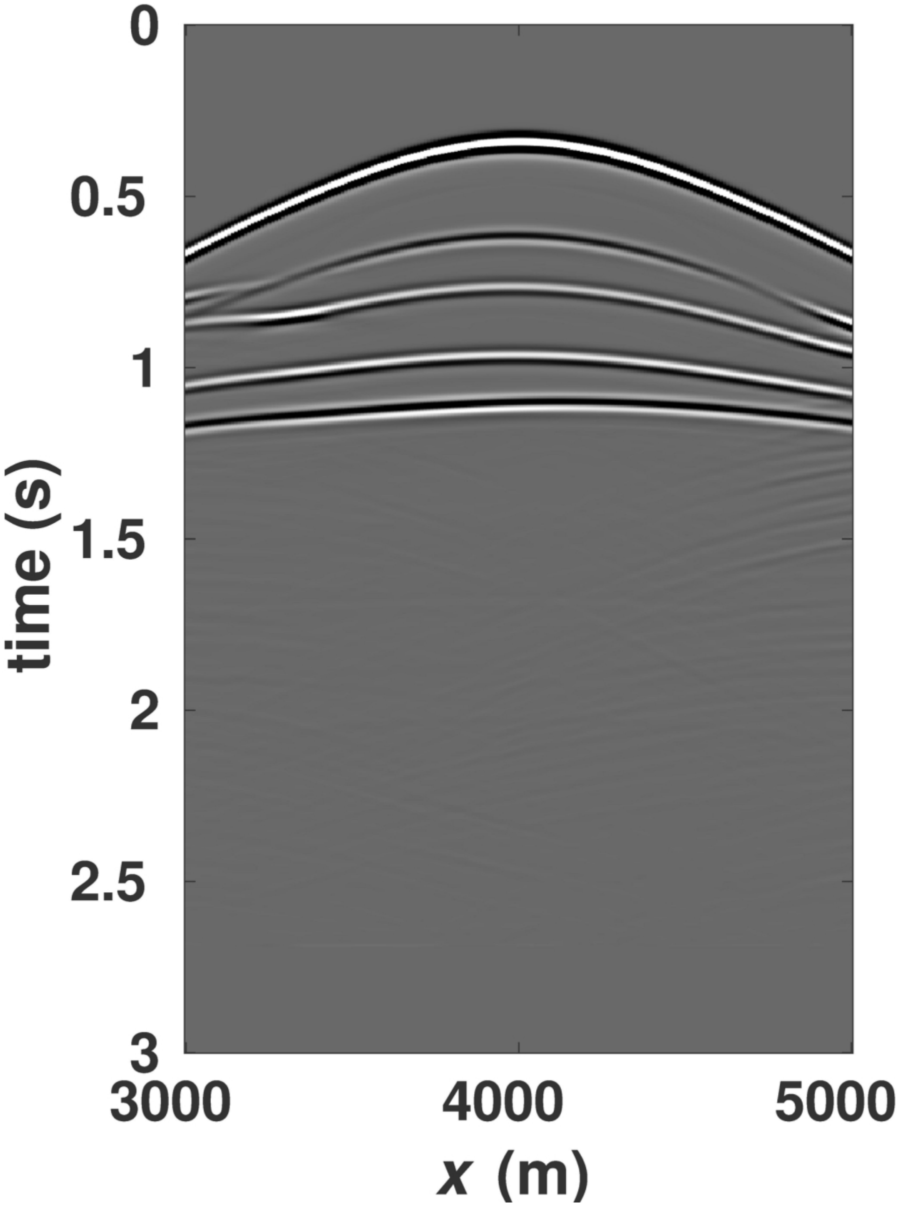

Figure 12(c). Results of primary estimation for the 2D model shown in Figure 9. The primary estimation from integrating on the monopole dimension.

147x191mm (300 x 300 DPI)

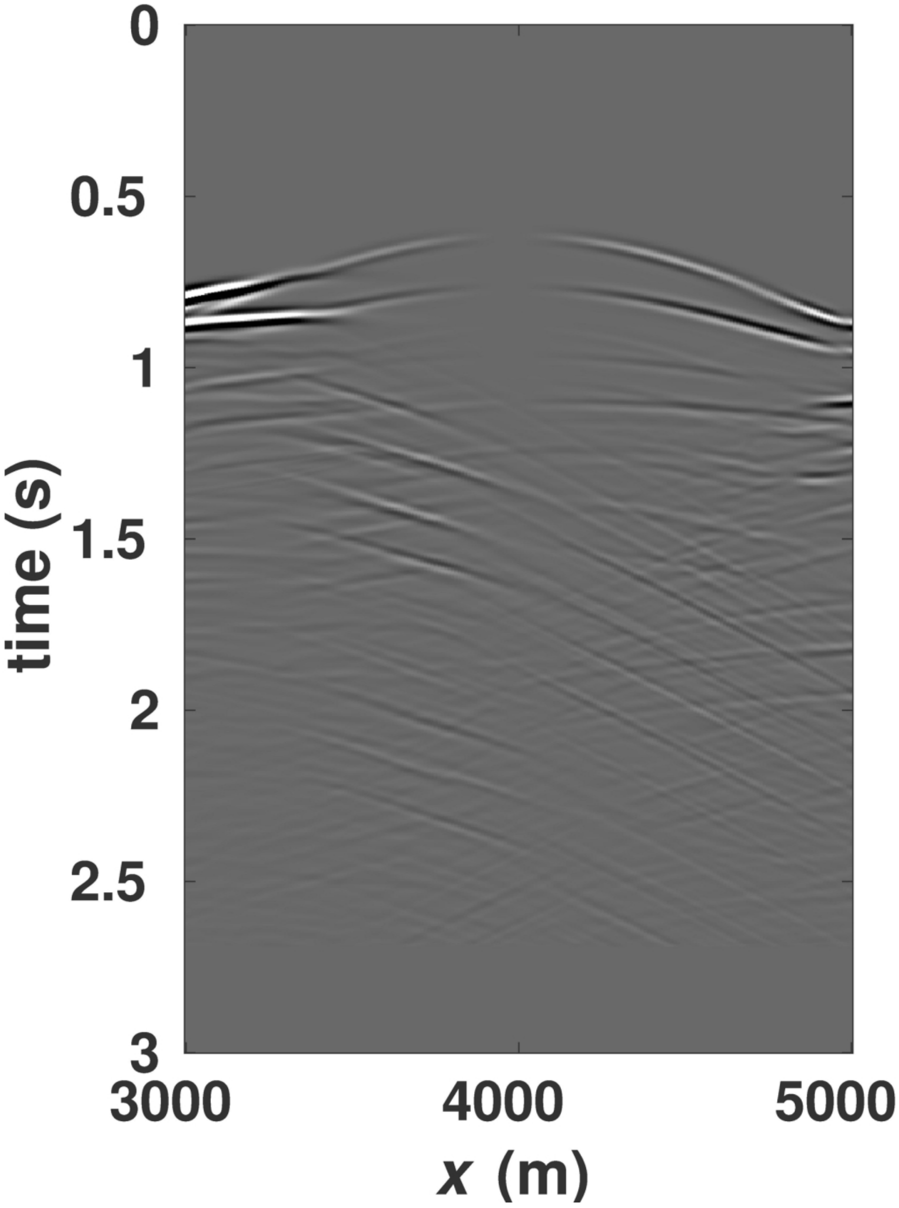

Figure 12(d) the difference between Figure 12(b) and Figure 12(c), of which the amplitude is multiplied by a gain factor of 10.

147x191mm (300 x 300 DPI)

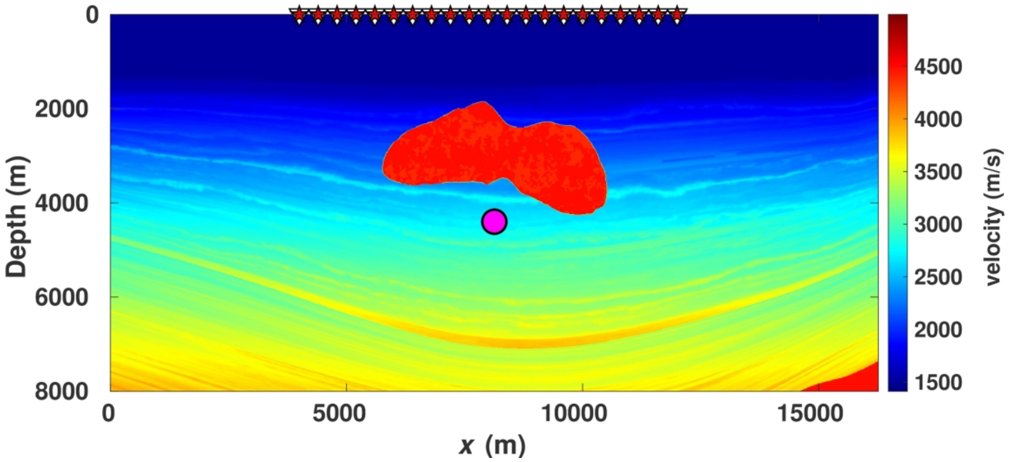

Figure 13. The velocity profile of the salt model with constant density. The magenta circle denotes the focal point ($X_F=8130\:\text{m}, Z_F=4400\:\text{m}$) located beneath the salt body. The red stars and white triangles indicate the source and receiver locations.

291x133mm (300 x 300 DPI)

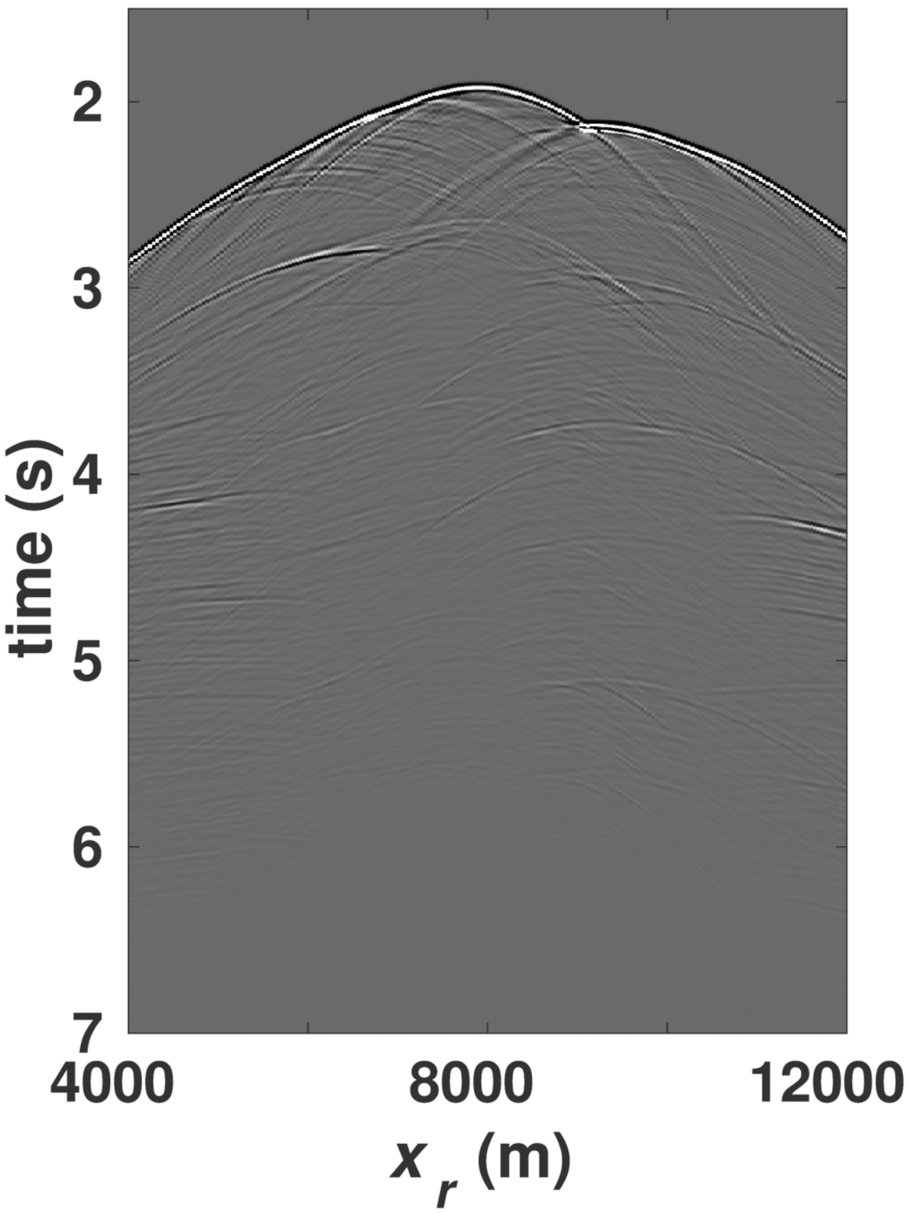

Figure 14(a). For the subsalt model with the focal point at $(X_F=8130\: ext{m}, Z_F=4400\: ext{m})$, the reference Green's function without subsampling.

146x187mm (300 x 300 DPI)

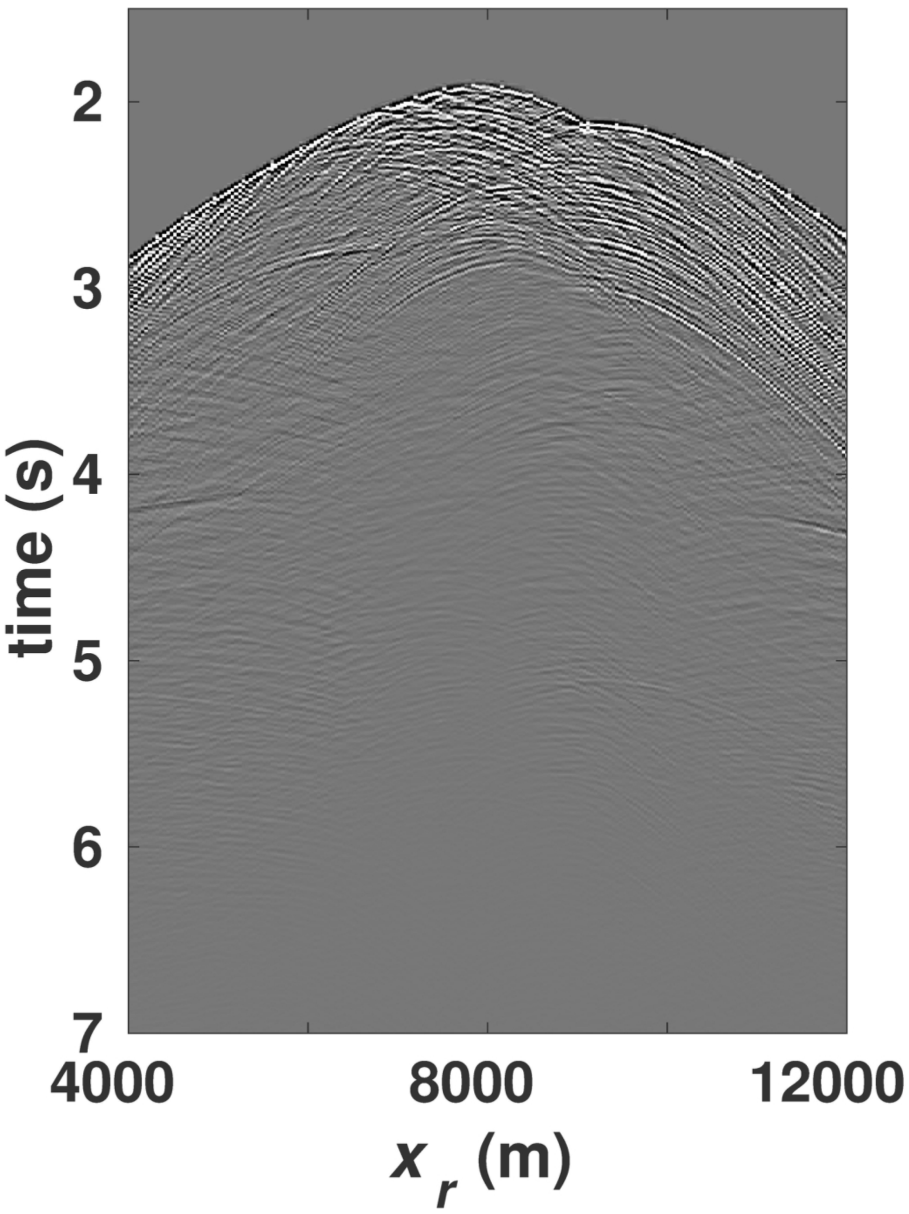

Figure 14(b). The same as Figure 14a, but calculated by subsampling and integrating over source and integrating on source.

146x187mm (300 x 300 DPI)

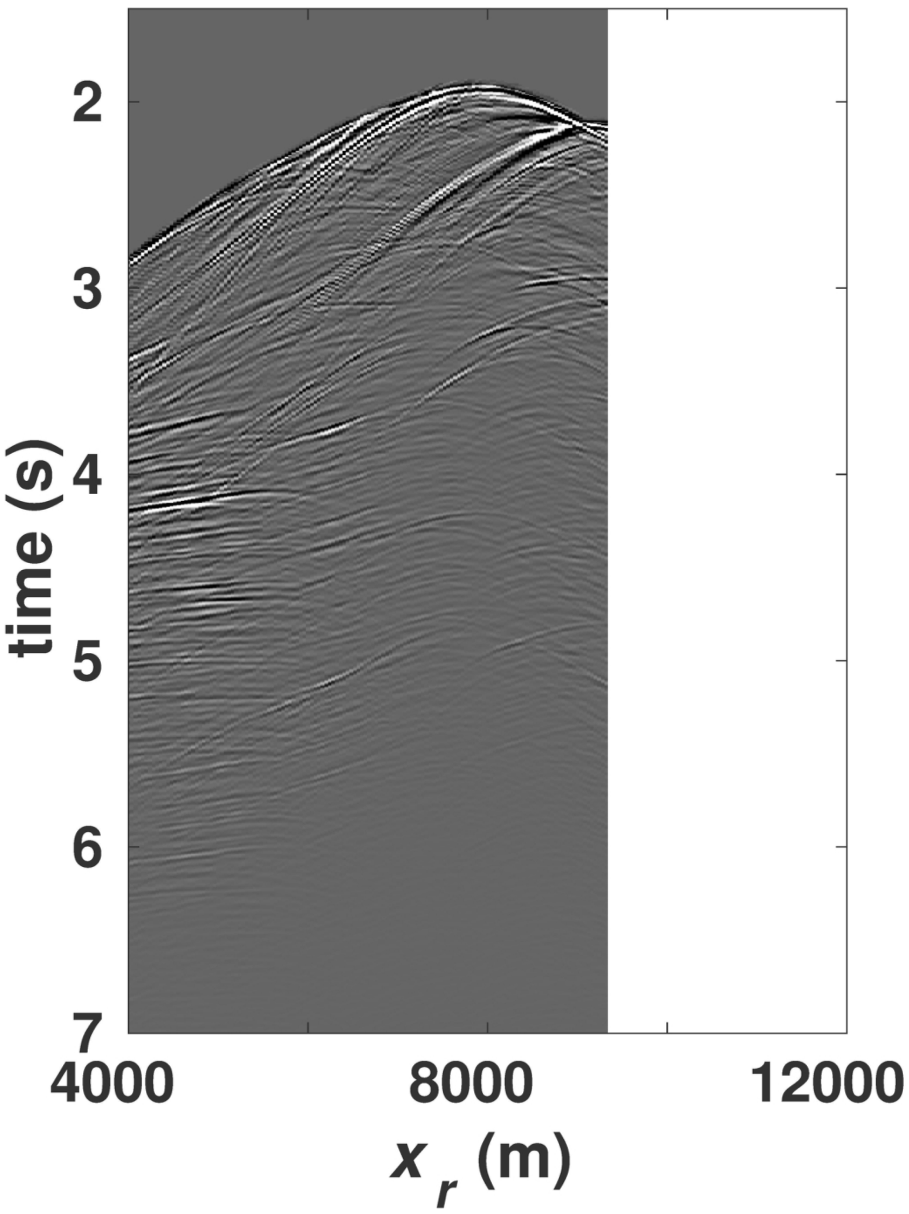

Figure 14(c). The difference plot between Figure 14(a) and estimated Green's function using fully sampled data, with \$2/3\$ of the original aperture.

146x187mm (300 x 300 DPI)

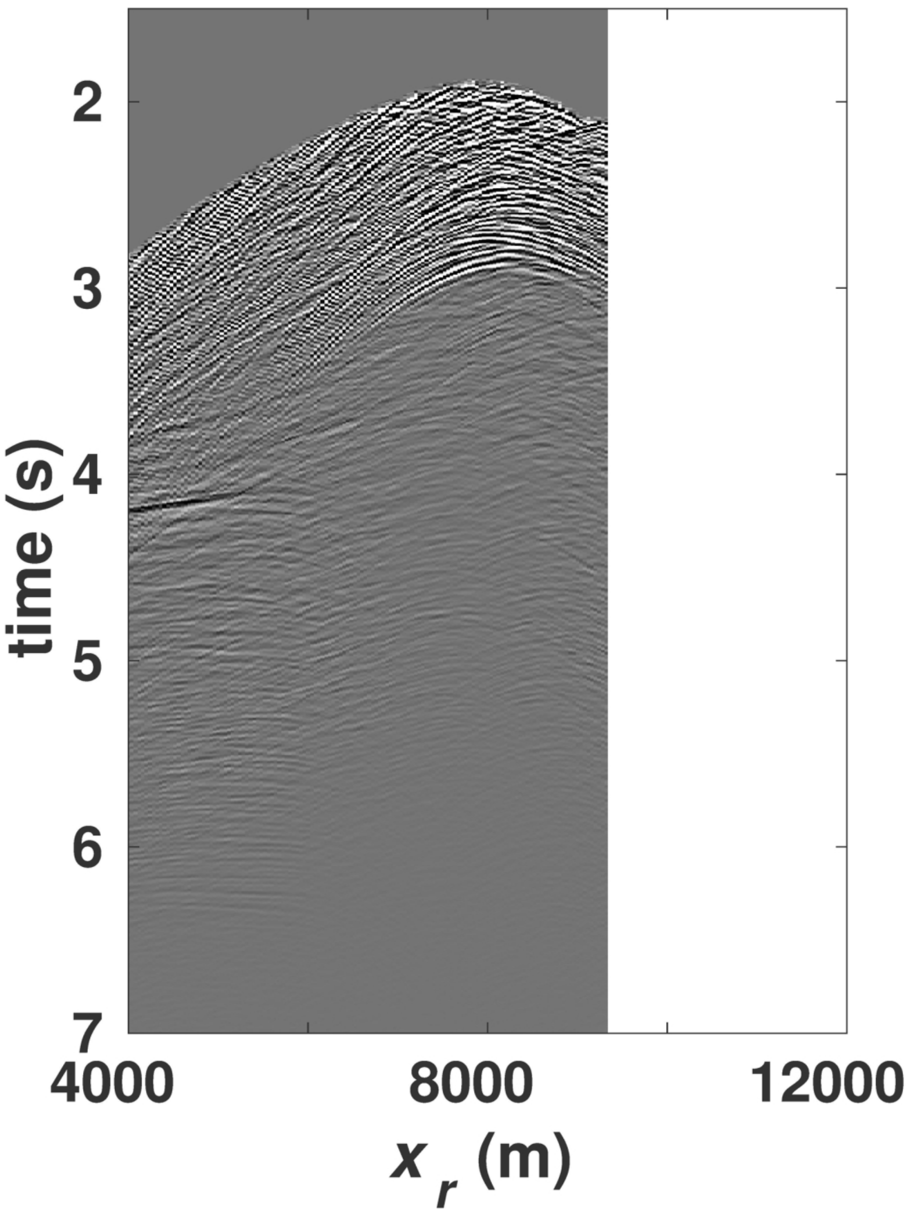

Figure 14(d). The difference plot between Figure 14(a) and estimated Green's function using subsampled data, with $2/3$ of the original aperture.

146x187mm (300 x 300 DPI)

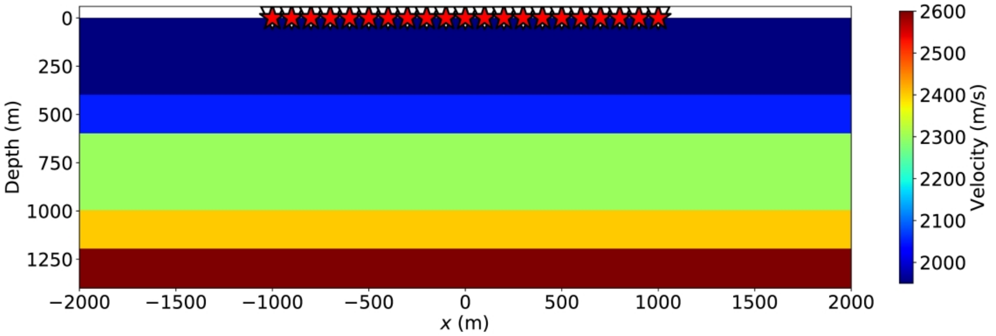

Figure 15. (a) Velocity profile of the four-layer model used for primary estimation, respectively. The red stars and white triangles indicate the source and receiver locations.

382x131mm (300 x 300 DPI)

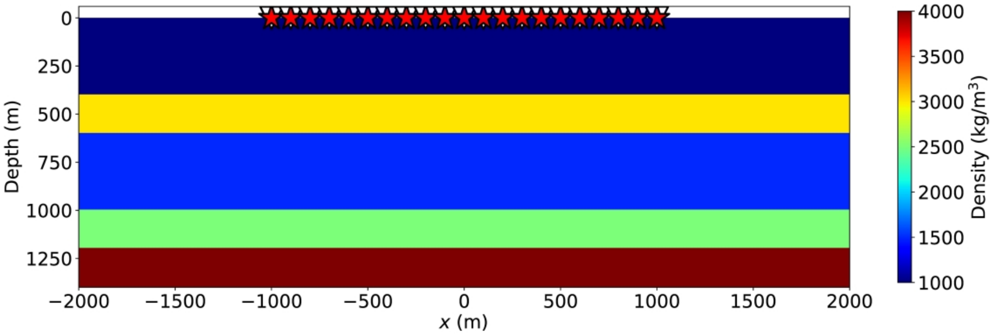

Figure 15(b) Density profile of the four layer model used for primary estimation, respectively. The red stars and white triangles indicate the source and receiver locations.

383x131mm (300 x 300 DPI)

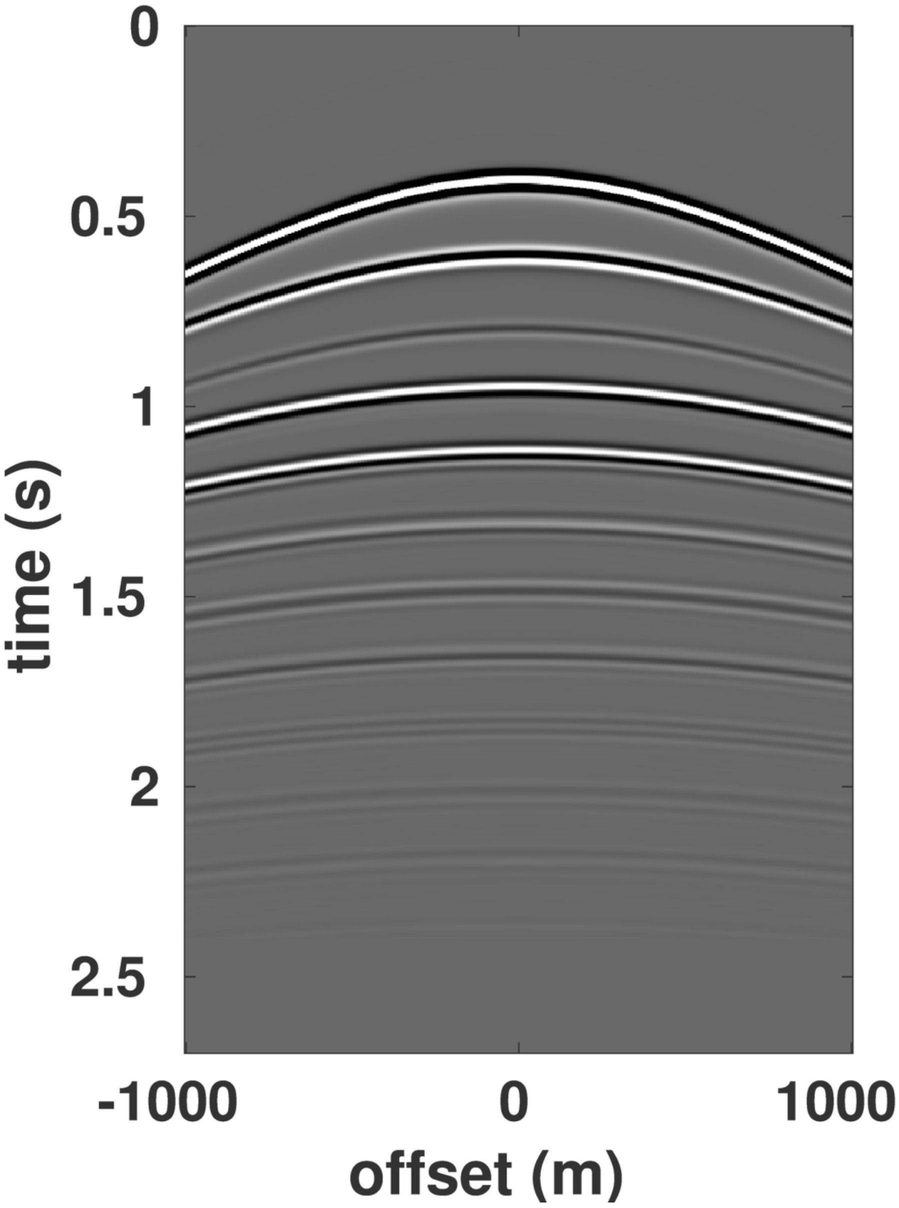

Figure 16(a). Comparison of the results of primary estimation with different subsampling scheme: The reference reflection data for a shot located at $x=0\:\text{m}$.

147x191mm (300 x 300 DPI)

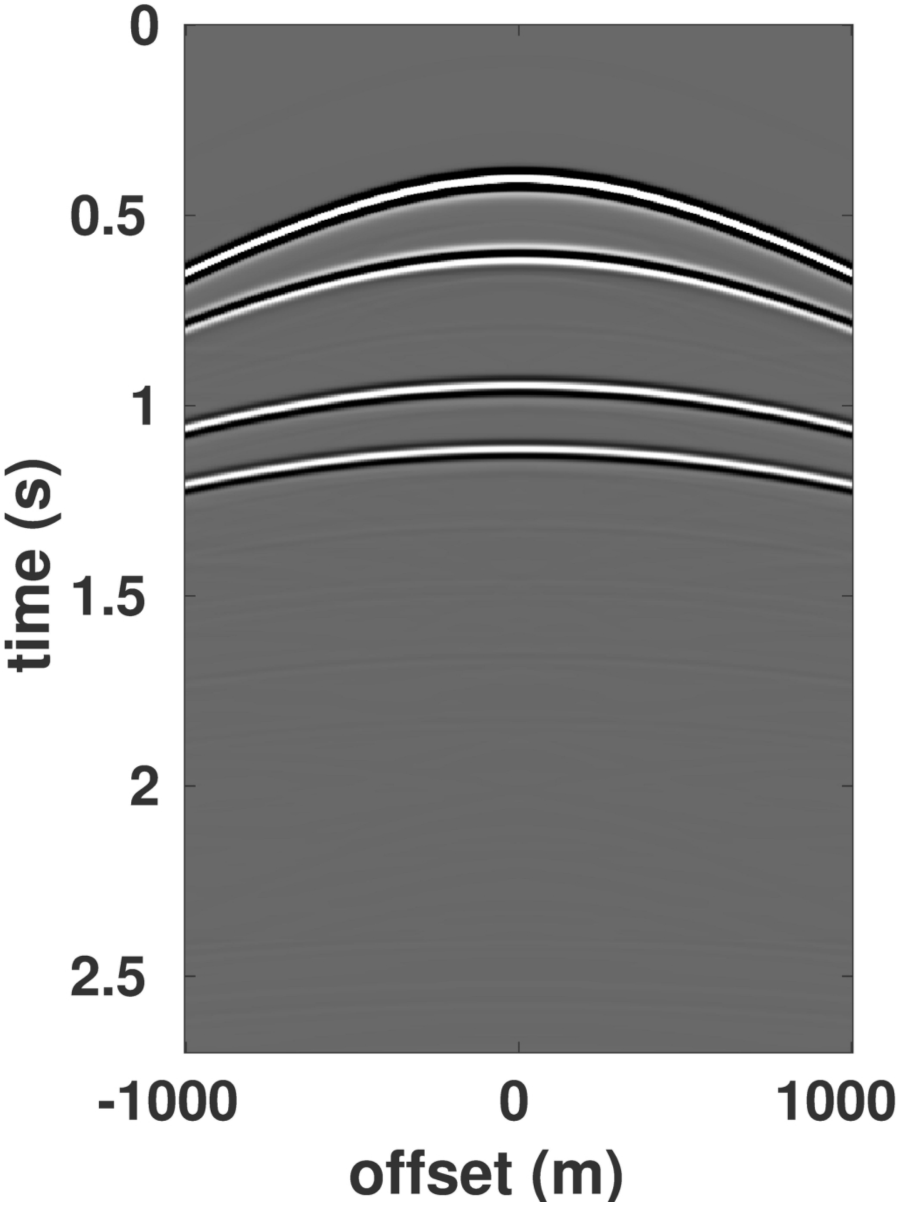

Figure 16(b). Result of primary estimation computed with full data with iterative substitution.

147x191mm (300 x 300 DPI)

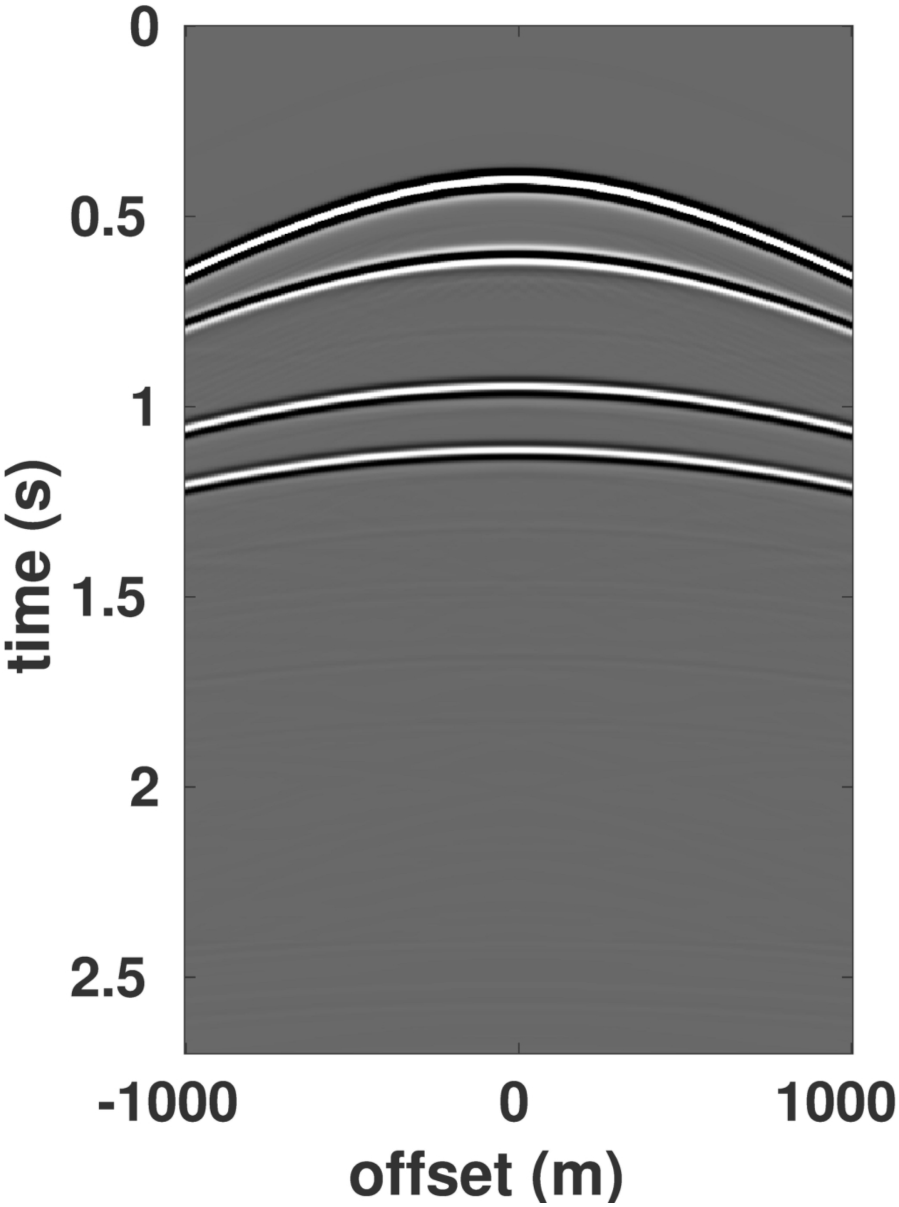

Figure 16c. Result of primary estimation computed with the subsampling scheme of evenly zeroing out 66% with iterative substitution.

147x191mm (300 x 300 DPI)

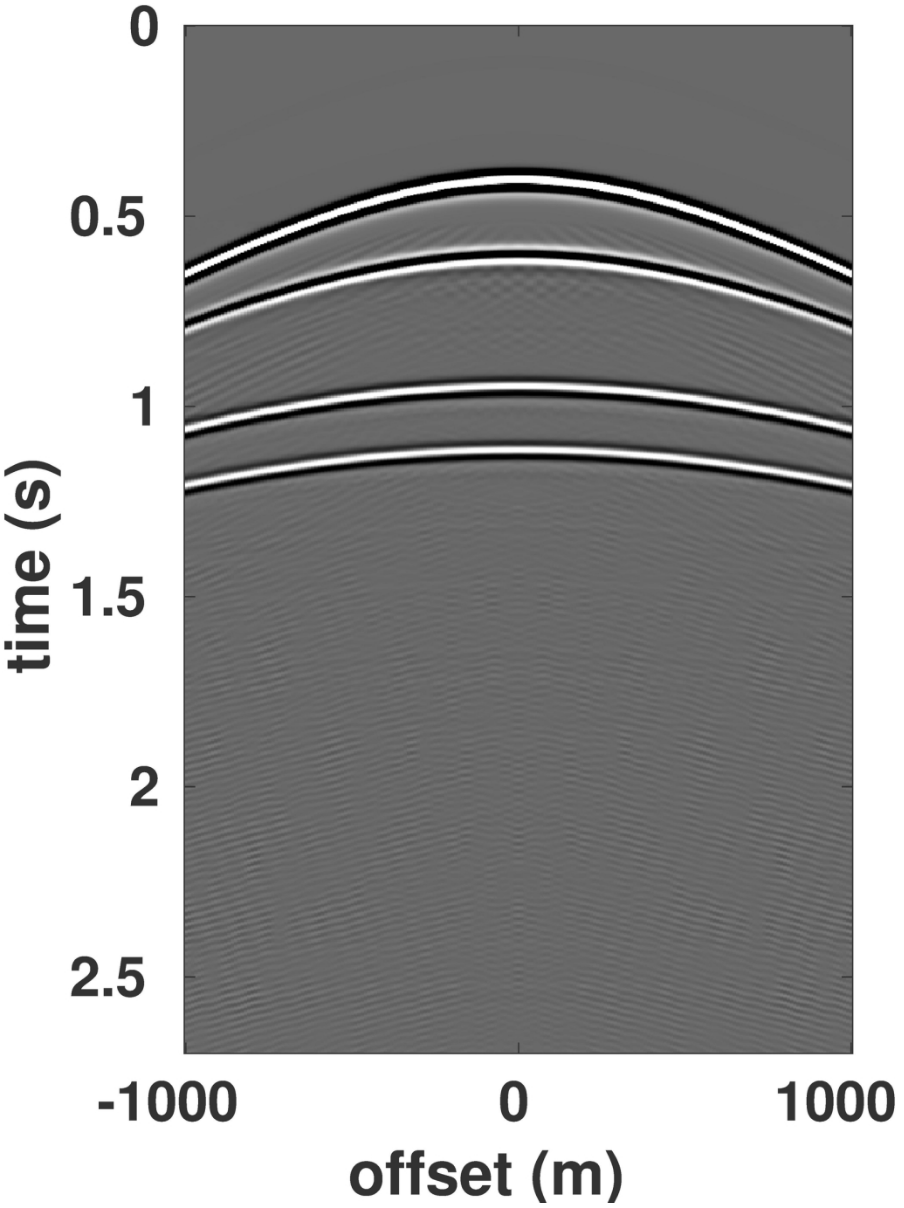

Figure 16d. Result of primary estimation computed with the subsampling scheme of evenly zeroing out 75% with iterative substitution.

147x191mm (300 x 300 DPI)

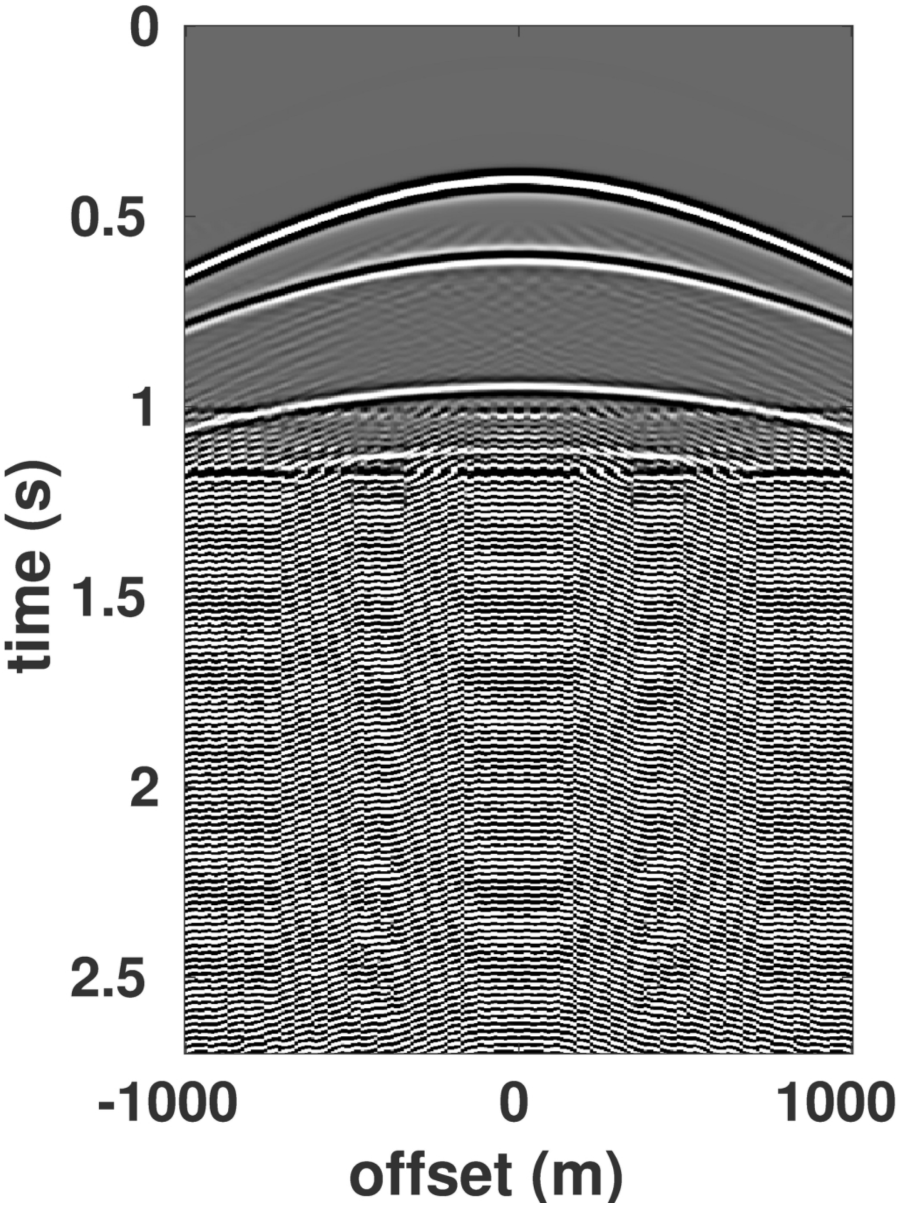

Figure 16e. Result of primary estimation computed with the subsampling scheme of evenly zeroing out \$80\\%\$ with iterative substitution.

147x191mm (300 x 300 DPI)

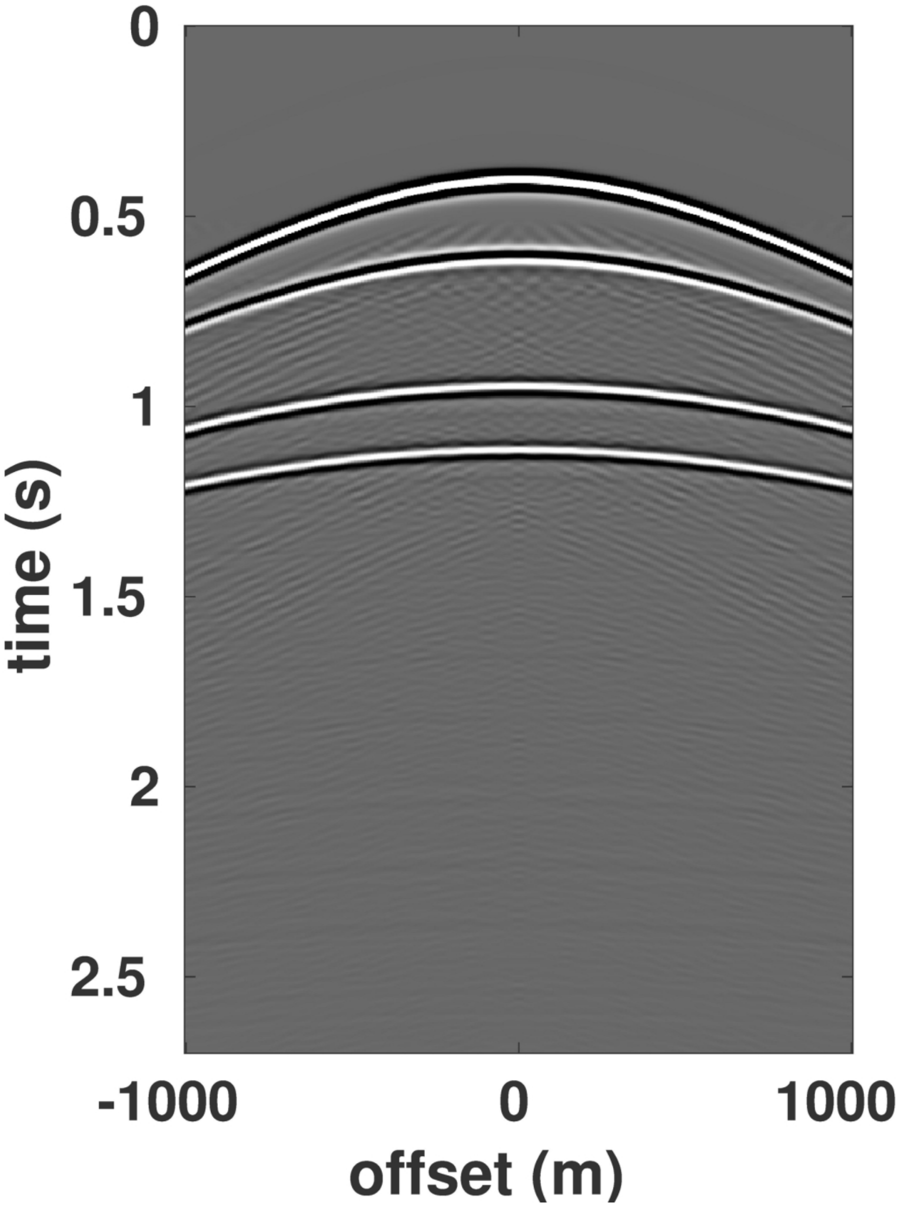

Figure 16f. Result of primary estimation computed with the subsampling scheme of evenly zeroing out 80% with LSQR.

147x191mm (300 x 300 DPI)

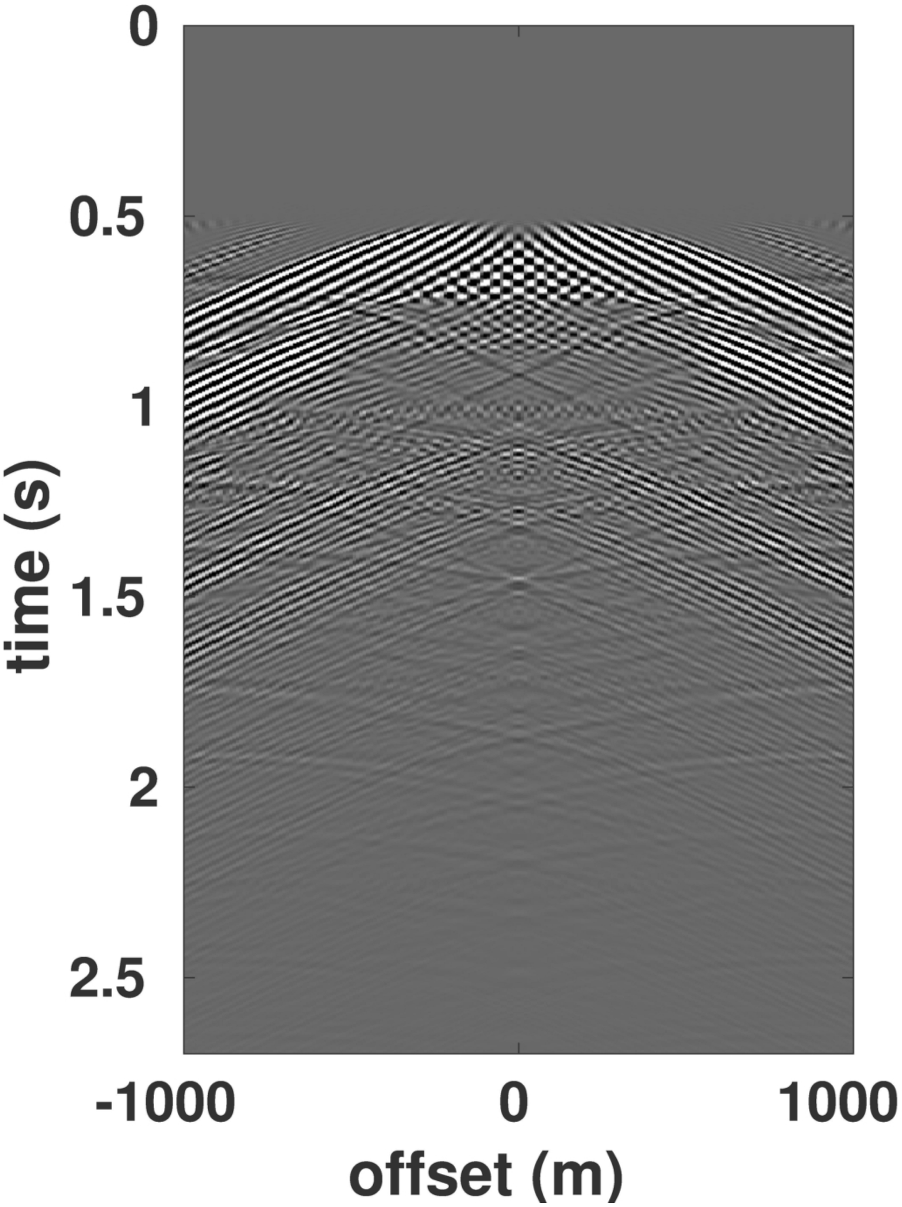

Figure 17(a) Error in the first iterations of primary estimation caused by subsampling (evenly zeroing out 75% of the 201 sources). All the amplitudes are clipped at 2$\%$ of the strongest arrival in Figure 16a.

147x191mm (300 x 300 DPI)

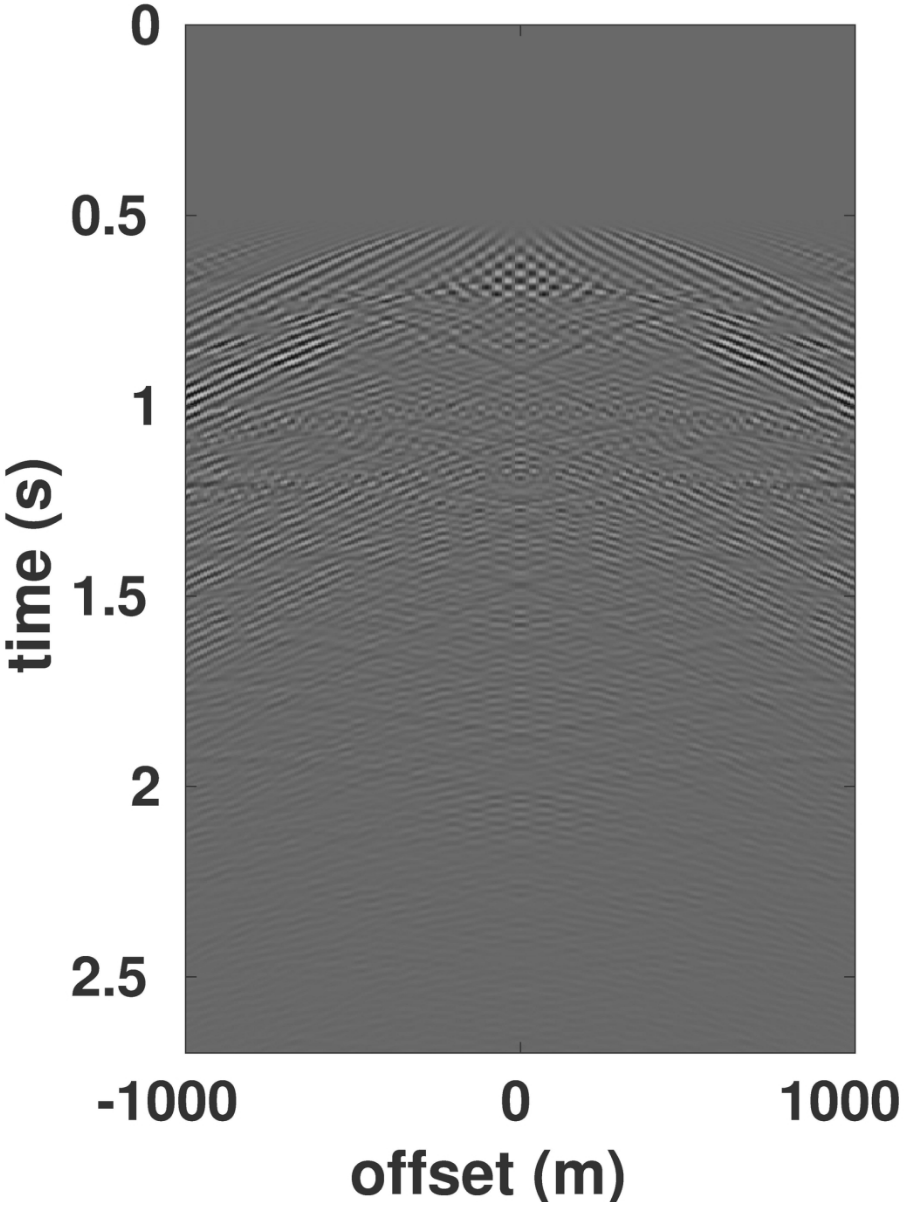

Figure 17(b) Error in the second iterations of primary estimation caused by subsampling (evenly zeroing out 75% of the 201 sources). All the amplitudes are clipped at 2$\%$ of the strongest arrival in Figure 16a.

147x191mm (300 x 300 DPI)

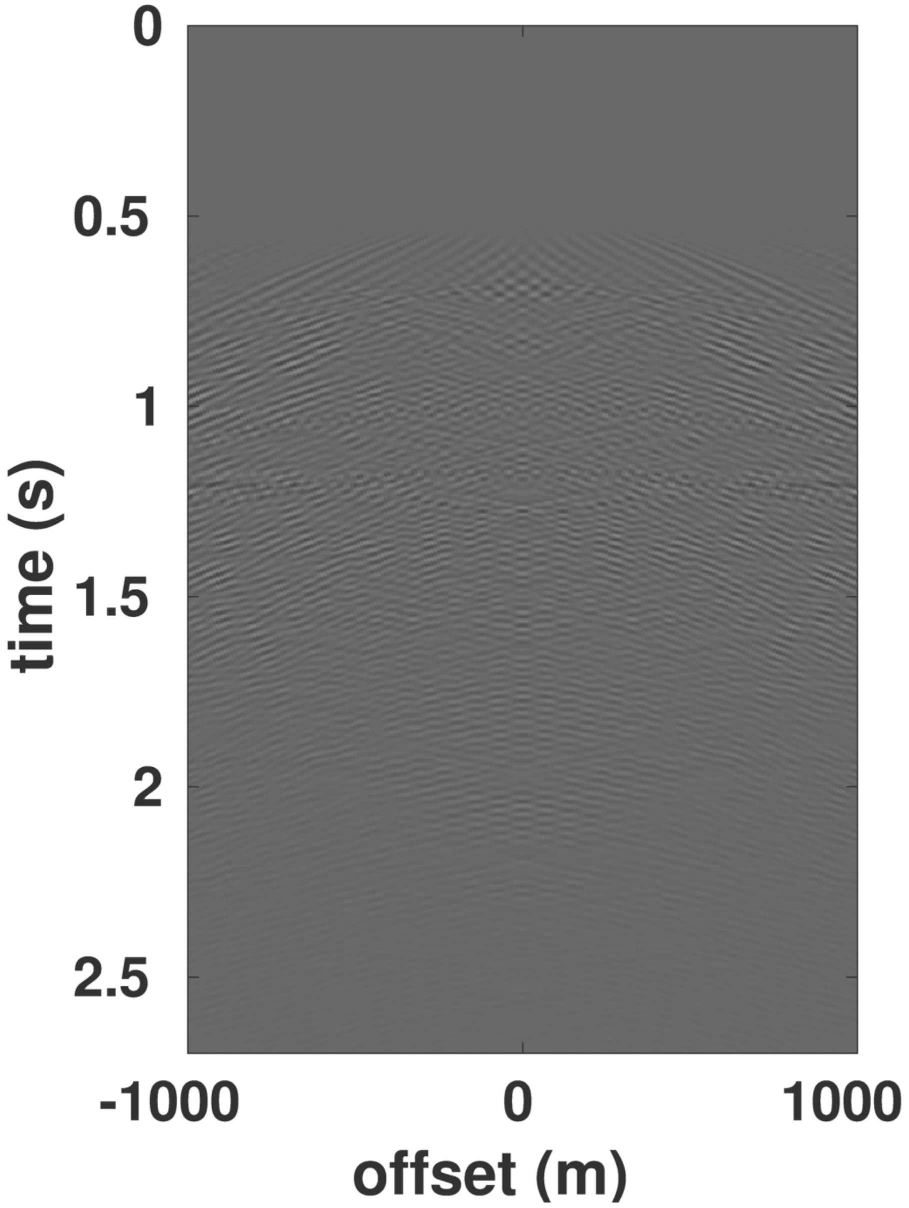

Figure 17(c) Error in the third iterations of primary estimation caused by subsampling (evenly zeroing out 75% of the 201 sources). All the amplitudes are clipped at 2$\%$ of the strongest arrival in Figure 16a.

147x191mm (300 x 300 DPI)

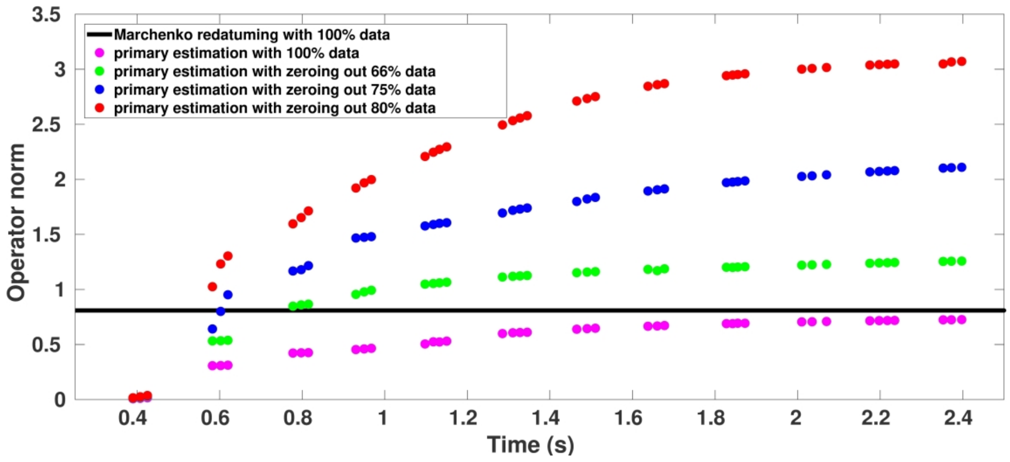

Figure 18 Comparison of operator norm of iterative substitution in primary estimation with different subsampling schemes (100$\%$ data, regularly zeroing out 66$\%$, 75$\%$, 80$\%$, respectively), as well as in the Marchenko redatuming with full data for the same model. Here, we note that the Marchenko redatuming operator norm corresponds to fixed focal point at depth --- thus not being one-to-one comparable with primary estimation on the acqusition surface --- but we choose to show it here merely to indicate that operator norm for redatuming is not time-dependent.

423x191mm (300 x 300 DPI)

DATA AND MATERIALS AVAILABILITY

Data associated with this research are available and can be obtained by contacting the corresponding author.

DOI:10.1190/geo2020-0914.1